Control of Nonlinear Laser Pulse Propagation in Plasma With Strong Magnetic Fields

by

Thomas Cunningham Wilson

A thesis presented for the degree of
Doctor of Philosopy in Physics

Physics Department, University of Strathclyde, Glasgow

Supervisors:
Prof. Zhengming Sheng
Prof. Paul McKenna

January 2020

This thesis is the result of the author's original research. It has been composed by the author and has not been previously submitted for examination which has led to the award of a degree.

Signed:

Date:

Abstract

We examine nonlinear laser pulse dynamics in plasma, encompassing both transverse and longitudinal envelope effects, in isolation and when coupled by the plasma. This is underpinned by an interest in how strong magnetic fields, aligned along the laser axis, modify these processes. In the presence of a strong magnetic field, such that the electron cyclotron frequency is on the order of the laser frequency, there is dramatic modification to the laser-plasma interactions, with the electron motion under left circularly polarised light remaining weakly-relativistic-like at laser intensities typically associated with fully-relativistic behaviour. Conversely right circularly polarised light sees the opposite effect, with the laser-plasma interactions becoming nonlinear at much lower light intensities. This affects all processes underpinned by relativistic motion of the electrons, chiefly self-focusing and self-compression. Such processes are studied in detail for both unmagnetised and magnetised plasma, and the results are compared. We find that not only does an external field alter the relativistic response of the electrons, but it also modifies the laser group and phase velocities, making the pulse shape of interest to the envelope dynamics. We apply this to study spherical compression of a laser pulse, wherein the pulse dimensions reduce symmetrically towards a single cycle. This process results in greatly amplified single-cycle pulses in the lambda-cubic regime, which may peak at over 100 times the initial laser intensity. Finally, the process by which a fully relativistic pulse may amplify an existing magnetic field is examined. We find that while this effect is known of for Laguerre-Gaussian light, it can also occur for linearly polarised light. The ponderomotive effect of the laser, and the external field trapping particles which would otherwise escape, bends their trajectories such that a self-sustaining azimuthal current forms. This current scales with both laser intensity and plasma density, and may produce fields of up to 10 kilotesla. We offer that this work may be of interest for the manipulation of low-power or long-wavelength lasers in underdense plasma, the generation of single-cycle pulses for high-harmonic generation and the generation of localised, quasistatic ultra-intense magnetic fields.

Contents

Acknowledgements

This thesis is the culmination of almost four years of work, and I would like to extend my thanks to everyone who contributed to making it possible. In particular I would like to thank:

- My supervisor Prof. Zhengming Sheng, for accepting me as a student and giving me the opportunity to contribute to this project, as well as his invaluable support over the years.
- Dr. Feiyu Li and Dr. Maria Weikum for their tireless support, patience, and out-of-hours email responses to every stupid question I had.
- My thesis examiners Dr. Bengt Eliasson and Dr. Gianluca Sarri for their constructive criticisms and useful insights.
- Everyone else in my group, and the wider physics dept. at Strathclyde, for useful discussions and advice.
- My friends and family, for putting up with me.

Chapter 0. Acknowledgements

Chapter 1

Introduction, Background and Theory

1.1 Introduction

The short-pulse laser has long been a primary scientific tool in the study of matter since its inception in the 1960s. For early laser technology, available power was limited to around the gigawatt level. The possibility of burning or melting delicate optical components restricted the development of higher-power laser systems due to the requirement that the reflectors and lenses be made larger and larger so as to reduce the incident laser intensity prior to the final focusing stage.

The damage thresholds of laboratory optical equipment was the major factor holding back the development of laser systems until the 1980s, when the technique of chirped pulse amplification (CPA) [1] allowed one to bypass this limitation via a technique of stretching and recompressing laser pulses such that the laser intensity does not rise above the damage threshold while the pulse is amplified. This development was recognised with a Nobel prize, and as a result available laser power has been growing inexorably. As of 2019, it is expected that the first all-optical studies of quantum electrodynamic (QED) processes will soon be possible [2–4] representing a major milestone in extreme-intensity lasers.

As laser power rises, the inherently self-interacting nature of physics becomes impossible to avoid. Intense lasers propagating through any medium affects the materials they are in, altering their properties and resulting in a field of physics termed nonlinear optics. By their nature, intense lasers operate in a pulsed-power mode. In order to amplify a laser pulse via CPA, the

initial seed pulse must already be short. Despite this, a nanosecond-duration pulse can easily carry kilojoules of laser energy. The optical damage threshold of solid-state optics equipment, which already restricted peak laser power available until the advent of CPA, continues to exert an in-practice limit on what can reliably be done with solid optics. The field of nonlinear optics is vast, and ever-present when dealing with intense lasers. At middling light intensity, nonlinear optical effects arise from the polarisation of molecules, and at higher intensities beyond the ionisation limit, this is replaced by plasma effects, and finally relativistic effects. The optical damage threshold itself represents an obvious manifestation of detrimental nonlinear optical effect.

As such, interest in plasma-based optics to focus and compress laser pulses beyond the limits of laboratory optics is growing [5]. The idea of a plasma as an optical medium is attractive for several reasons. Not only does the fluid nature of a plasma mean that the concept of a damage threshold is no longer relevant, but in priciple, the optical properties of a plasma are extremely tunable. Density profiles ranging from tenuous plasmas close to a vacuum to high density gas jets measuring several times the critical density [6] are readily achievable. This makes plasmas useful in cases where high light intensity may preclude the use of traditional optics, and in cases where the light wavelength or pulse dimensions would require very specialised components. The extremely compact nature of plasma optics is also desireable, with optical processes such as focusing possible over extremely short distances on the order of tens or hundreds of laser wavelengths.

The optical properties of plasmas are very well understood at this point, derived from an understanding of how charged particles move under the influence of an electromagnetic (EM) wave, and the resulting currents inform how the wave propagates. The exact shape of these particle orbits are influenced by both the light itself, and any external fields. Of most relevant interest to this work are magnetic fields. In most cases, ambient magnetic fields range from the microtesla level (such as the Earth's magnetic field) to the tens of tesla generated by a solid-state electromagnet. When compared to the fields of the laser, this is vanishingly small, and very often such fields can be neglected when determining the optical properties of the plasma. However, recently magnetic fields at the kilotesla level have been produced by capacitor coil target setups [7,8], and yet stronger fields in the tens of kiloteslas is proposed by using so-called snail targets [9]. This opens up the possibility of background magnetic fields at or above the field strength of the laser light itself, radically changing the particle orbits, and therefore the plasma optical properties, presenting an interesting area of study.

This thesis begins with a general introduction to laser and plasma physics in chapter 1,

and then applies this to study how short-pulse laser propagation in plasma is affected by a strong magnetic field in chapter 2, in particular examining the laser envelope dynamics. This is expanded upon in chapter 3 which derives a general framework to describe short-pulse envelope dynamics in plasma, and considers a special case where the laser envelope collapses down onto a point. The final research chapter 4 examines the case where an external magnetic field in a plasma may be amplified by an intense laser.

1.2 Applications of Short-Pulse Lasers

1.2.1 Plasma-based Accelerators and Radiation Production

Applications of short-pulse lasers in plasma are extremely varied, finding relevance in many different areas. Among the most well known applications is plasma based particle accelerators, whereby electron or ions are accelerated to relativistic velocities using a plasma. Proposed in the late 1970s [10], the concept was experimentally verified not long after [11, 12]. In the time since, the development of laser-plasma accelerators has become a deep field of study in itself, with multiple schemes emerging. Plasma wakefield acceleration (PWFA) involves the use of an existing particle bunch to excite the plasma, and accelerate particles caught in the wake. Alternatively, a laser-driven wake may be used to accelerate the particles, termed laser wakefield acceleration (LWFA). Almost all optical schemes require that the laser is of relativistic intensity, and the pulse dimensions fall close to the plasma wavelength. In real terms, this means intensities on the order of 10^{18} Wcm^{-2} and up, and pulse durations around the tens of femotoseconds. This work considers laser powers slightly below this regime, but with extensions to the models discussed, it may be applied. Further variations exist in the form of laser beat-wave acceleration (LBWA) [13] wherein two lasers of different frequencies are employed, self-modulated laser wakefield acceleration (SMLWFA) relies on self-modulation of the wake by stimulated Raman scattering (SRS) [14] and yet more schemes are proposed on a regular basis [15, 16].

Across all schemes, the persistent feature of laser-based accelerator schemes is the extremely compact nature of the devices. The accelerating electric field gradients of plasma accelerators routinely reach tens of gigaelectronvolts per meter [17,18], compared to MeV/m gradients found in conventional radio frequency (RF) accelerators [19]. The result is particle energies on par with conventional accelerators, achieved in a fraction of the distance. The advent of petawatt laser systems bring with them the expectation that these extreme gradients will continue to rise [20, 21], making particle energies into the multi-gigaelectronvolts possible with lab-scale

equipment, rather than requiring acceleration over multiple kilometers in traditional linac or cyclotron RF accelerators.

While the compact nature of plasma accelerators is a great advantage, when compared to traditional linacs, plasma accelerators lag in some areas. As laser power rises, so does achievable beam energy, but the beam quality must also be considered. Bunch stability, energy spread and emittance must be controlled so that the resulting electron beam is useful for specific application, and the brightness of the beam i.e. the total number of electrons accelerated must also be controlable. These are all areas of active study and improvement [22].

Related to plasma accelerators is the concept of plasma-based radiation production. When an electron bunch is accelerated in a plasma accelerator, the extremely strong longitudinal electric fields cause the bunch to reach relativistic velocities. However, there are also transverse fields, which act to keep the electron bunch centered in the accelerating cavity. Inevitably, as particles enter the cavity they will have some residual transverse momentum. When combined with the focusing fields, this causes the bunch to oscillate while it is accelerated. This results in so-called betatron radiation being emitted by the bunch in the forward direction, typically at X-ray energies [23, 24]. A more complex setup may be employed involving a preformed curved plasma channel may be used to guide a laser pulse round in an arc. If the laser is introduced into the channel slighlty off-axis, the laser centroid, and hence the entire accelerating structure will oscillate, and as such the radiation emitted by the accelerated electrons will reflect this motion [25]. In this way, the plasma may be used in place of a sychrotron for the purposes of generating X-ray photons of tunable frequency. Still higher energy gamma ray photons may be produced by interaction with high density plasma. Via a resonant energy transfer process, electrons are directly accelerated by the laser and reach energies sufficient to emit gamma rays [26].

1.2.2 Inertial Confinement Fusion

Possibly the most appealing potential application of intense lasers is the concept of inertial confinement fusion (ICF). A small amount of hydrogen fuel is compressed by an array of high-energy, but relatively low-power lasers [27], eventually reaching densities and temperatures high enough that spontaneous nuclear fusion occurs. This results in a self-sustaining nuclear fusion reaction, and the resulting energy release may be used to generate electricity. To date, the remains a subject of very active research [28].

The two basic schemes of ICF are direct (DD) and indirect drive (ID). In DD, the fuel capsule is directly illuminated by the laser light, and energy is coupled into it in this way. In

ID, the capsule is surrounded by a hollow metal shell called a hohlraum, which is illuminated by the lasers instead. The hohlraum heats up and reradiates X-rays, which bathe the inside of the hohlraum and compress the fuel. In both cases, the end goal is to couple energy from either the lasers or the thermal X-rays into the fuel. First, to compress the fuel, and then at the point of stagnation, to heat the fuel to the point that a self-sustaining fusion reaction can take hold.

Either scheme requires a lot of laser energy, as the coupling efficiency to the fuel is very low, and extremely symmetric illumination. Typically ICF makes use of many individual laser beamlets of up to nanosecond duration, with each one carrying up to kilojoules of energy [29]. This is orders of magnitude higher than those considered for particle acceleration, however the high energy density nature of the process results in many complex laser-plasma interactions over the entire duration of the compression [30].

In addition to these basic schemes, more sophisticated schemes exist. So-called fast ignition (FI) aims to decouple the compression and the heating aspects of the process, and in doing so relax the energy requirements of the lasers. While the laser is still used to compress the fuel, the heating of the fuel is mediated by a beam of relativistic electrons, such as generated by a plasma accelerator scheme [31]. This scheme has recieved attention recently in the form of a magnetically-assisted (MA) modification. In the MA-FI scheme a strong longitudinal magnetic field is used to collimate the particle beam towards the compressed fuel. The concept has been demonstrated guiding relativistic electrons through a solid target using an imposed magnetic field [32], and specialised simulation codes have been developed to study it specifically for ICF [33, 34].

1.2.3 Plasma Optics

The use of a plasma as an optical medium in and of itself has recieved increasing interest in recent years. In situations where solid-state optics would be impractical, or impossible due to scale or incident laser power, the use of a plasma in place of traditional laboratory optics is an attractive prospect due to their extremely tunable optical properties, and malleable fluid nature.

The widespread adoption of CPA for the generation of high-intensity lasers is undoubtedly a necessity when dealing with ultraintense lasers, but as laser power continues to rise, eventually equipment damage thresholds become significant again. One possible reponse is to simply increase the size of the optics, thus lowering the incident intensity, but this obviously has limits of its own. Quite apart from the practicality of using extremely large optics, the equipment

becomes increasingly expensive to buy and maintain. Instead, we may look to a plasma to solve the problem. An already ultraintense 'seed' laser may be further amplified in a plasma by Raman backscattering (RBS) amplification over multiple order of magnitude by interaction with a 'pump' laser [35–38] over centimeter scales, again taking advantage of the extremely compact nature of optical processes in plasma, and the lack of a damage threshold.

Similarly, focusing optics are subject to the same material damage thresholds, and these processes too may be accomplished with a plasma. Intense light will spontaneously self-focus in plasma via a variety of means [39], and the first simulations clearly demonstrating such processes were performed in the 1990s [40]. Self-focusing is a fundamental process, and as such interest remains high, with schemes proposed to use plasmas as efficient lenses, hoping to see order-of-magnitude increases of on-axis intensity and simultaneously improve other aspects of the pulse profile, such as the temporal contrast [5]. Such schemes are typically in-plasma, i.e. the pulse enters the plasma, and then undergoes focusing and its ultimate purpose without returning to vacuum. However, a so-called 'thin' plasma lens may be employed in the manner of a traditional optic, where the pulse enters a plasma, undergoes some focusing, and then returns to vacuum [41].

Plasmas may also be employed as mirrors. By directing an intense laser onto a surface, a plasma inevitably forms at that surface. Lasers may not propagate through plasmas above a critical density, and instead will be reflected from that surface with extremely high efficiency, regardless of the specular properties of the original solid material. In this way, the expanding plasma can be used as a specular mirror, or optical switch. In the relativistic regime, high density gradient interactions may produce high harmonic generation (HHG) at the laser-plasma interface [42, 43]. In a related application, the interference pattern of two lasers may be used to selectively ionise a surface, producing a modulated plasma mirror, or a plasma hologram. This may then be used to generate complex phase structures at relativistic intensities by reflecting lasers off this specialised mirror [44].

The analogies continue, with plasmas also capable of being made to resemble optical waveguides for short-pulse guiding, by having a two-pulse train. The first pulse evacuates a filament of the plasma, and the second pulse follows in the newly created cavity [45–47]. The interaction of two colliding lasers in a plasma may cause the formation of periodic density structures, which function as a diffraction grating [48]. These structures are long-lived and may be employed to chirped-pulse compression [49], again with no appreciable damage threshold. Periodic density structures in plasma may also be employed as optical modulators [50, 51], in order to manipulate pulse envelopes. Plasmas may be employed as light polarisers. The use of a magnetic

field imposed on a plasma causes linearly polarised light to faraday-rotate as it propagates. Or, in the case of ultrashort pulses and strong magnetic fields, it causes complete separation of the circularly polarised components of the pulse [52]. This effect may also be used to generate circularly polarised (CP) THz radiation at a tunable frequency [53].

Indeed there is little that can be accomplished with a traditional optics that cannot also be accomplished with a plasma. As the fundamental physical mechanisms for many of the above mentioned optical processes in a plasma overlap, it is possible and expected that they will occur spontaneously, and simultaneously. The desireable properties of plasmas as an optical media coupled with the inherant instability associated with intense light in a fluid material make this a highly motivated, challenging field of study. This work contributes to plasma optics in that the focus is the manipulation of short-pulse lasers with a plasma as the optical medium. The specific focus is the inclusion of a magnetic field.

1.3 The Laser Pulse

In simple terms, the laser electric field $\boldsymbol{E}$ can be given by

$$\boldsymbol{E} = \hat{\boldsymbol{e}}_{\boldsymbol{p}} \psi \exp(i\phi), \tag{1.1}$$

where $\hat{\boldsymbol{e}}_{\boldsymbol{p}}$ is the polarisation vector, ϕ is the phase angle and ψ is the envelope.

The vector $\hat{\boldsymbol{e}}_{\boldsymbol{p}}$ describes the polarisation state of the light. This may be written in generalised form as

$$\hat{\boldsymbol{e}}_{\boldsymbol{p}} = \hat{\boldsymbol{e}}_{\boldsymbol{x}} + i\delta \hat{\boldsymbol{e}}_{\boldsymbol{y}}, \tag{1.2}$$

where depending on the value of δ, we may use this to describe left-circular polarisation (LCP) where $\delta = -1$, linear polarisation (LP) where $\delta = 0$ and right-circular polarisation (RCP) where $\delta = +1$. In this work we make no distinction between O-mode and X-mode linear polarisation in this definition. An even more generalised form for $\hat{\boldsymbol{e}}_{\boldsymbol{p}}$ which would allow for an initial polarisation angle θ_0 and a varying degree of ellipticity φ is given by

$$\hat{\boldsymbol{e}}_{\boldsymbol{p}} = \cos(\theta_0)\hat{\boldsymbol{e}}_{\boldsymbol{x}} + \sin(\theta_0)\hat{\boldsymbol{e}}_{\boldsymbol{y}} + i\delta e^{i\varphi}\cos(\theta_0)\hat{\boldsymbol{e}}_{\boldsymbol{y}} + i\delta e^{i\varphi}\sin(\theta_0)\hat{\boldsymbol{e}}_{\boldsymbol{x}}. \tag{1.3}$$

The phase angle of the beam may be approximated by a plane wave

$$\phi = \boldsymbol{k} \cdot \boldsymbol{r} - \omega t, \tag{1.4}$$

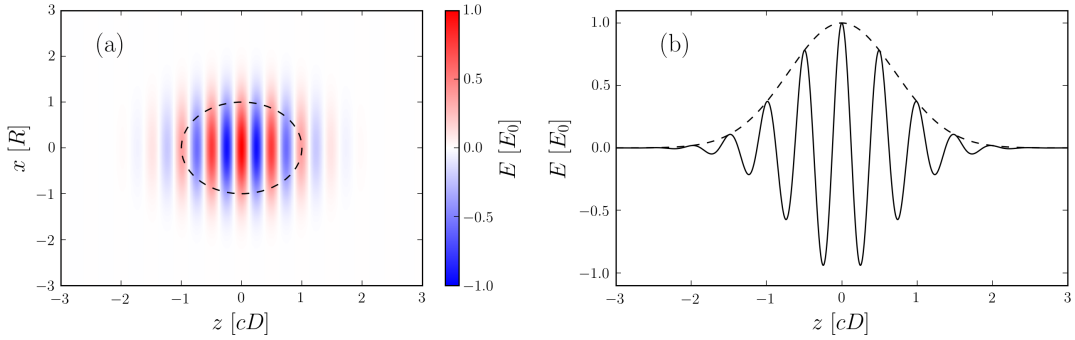

Figure 1.1: Schematic showing an enveloped laser pulse in (a) 2D, where the black dashed line traces the points at which the envelope drops to 1/e of the peak amplitude, and (b) a 1D slice along $r = 0$ showing the envelope (dashed) over the phase (solid).

and we take ψ to be a gaussian envelope

$$\psi = a \exp\left[-\frac{(z-ct)^2}{c^2 D^2} - \frac{r^2}{R^2}\right], \tag{1.5}$$

where a is the field amplitude, and R describes the laser spot radius, and D describes the pulse time duration. Both R and D are defined as the half-width of the envelope where the amplitude falls to $1/e$ of its maximum value.

In fact, we should consider all the lasers as initially gaussian beams. This introduces several extra terms to the phase angle in order to describe wavefront curvature, and extra terms to the envelope in order to describe vacuum diffraction. While these terms are not included in our analytical evaluations, their omission does not affect the relevant physics, as nonlinear processes arising from laser-plasma interactions dominate the propagation characteristics once the beam enters a plasma. Nevertheless, these terms are taken into account in the numerical simulations. A schematic of an enveloped laser is given in figure 1.1.

Higher-order modes exist in various forms, the most well known being the Hermite-Gaussian (HG) and Laguerre-Gaussian (LG) modes. LG mode lasers are characterised by a helical phase structure and intensity minimum on the axis due to the phase singularity at that point. LG modes can be described by the addition of two indices l and p describing the azimuthal and radial mode numbers. Specifically l describes the azimuthal phase dependence, where the wave phase varies by l complete rotations around the laser axis, and p describes the number of amplitude peaks in the radial direction. The simplified laser elecrtic field of a LG laser is given

in cylindrical coordinates (r, θ, z) by

$$\boldsymbol{E} = \hat{\boldsymbol{e}}_{\boldsymbol{p}} \mathcal{L}_p^{|l|}(r^2) \left(\frac{r}{R}\right)^{|l|} \exp\left[-\frac{(z-ct)^2}{c^2 D^2} - \frac{r^2}{R^2}\right] \exp\left[i(kz - \omega t - l\theta)\right], \tag{1.6}$$

where $\mathcal{L}_p^{|l|}(r^2)$ is a generalised Laguerre polynomial of textbook form. When $l = p = 0$ the standard Gaussian mode is recovered. In this work we will only consider $p = 0$ mode LG beams, and as $\mathcal{L}_0^{|l|}(r^2) = 1$, this simplifies the analysis required. From (1.6) we see that the sign of the azimuthal index l is relevant only in the phase, and determines the handedness of the beam, specifically it gives the sign of the orbital angular momentum (OAM) carried by the beam, in the same way the sign of δ determines the sign of the spin angular momentum (SAM).

The transverse components of the field are well defined via the above methods, but longitudinal fields are not taken into account. In vaccum these must be determined by solving $\nabla \cdot \boldsymbol{E} = 0$ in order to fully satisfy the wave equation. Once the electric field is defined, the magnetic field is given by

$$\boldsymbol{B} = \frac{1}{c}\hat{\boldsymbol{k}} \times \boldsymbol{E}. \tag{1.7}$$

Light intensity I is given by the magnitude of the Poynting vector $\boldsymbol{S}$

$$I = |\boldsymbol{S}| = \frac{1}{\mu_0}|\boldsymbol{E} \times \boldsymbol{B}|, \tag{1.8}$$

In vacuum $B = E/c$, and $c = (\epsilon_0 \mu_0)^{-1/2}$ and hence

$$I = c\epsilon_0 E^2 \tag{1.9}$$

for CP light. Beam power P is given by I (or more generally $\boldsymbol{S} \cdot \hat{\boldsymbol{e}}_{\boldsymbol{z}}$ for a laser directed along z) integrated over the transverse dimensions, and pulse energy $\mathcal{E}$ is given by the power integrated over time;

$$P = \int_0^{2\pi} \int_0^{\infty} Ir \, \mathrm{d}r\mathrm{d}\theta, \tag{1.10}$$

$$\mathcal{E} = \int_{-\infty}^{\infty} P \, \mathrm{d}t. \tag{1.11}$$

Assuming E is Gaussian in fundamental mode, the intensity envelope is hence

$$I = c\epsilon_0 E^2 \exp\left[-2\frac{r^2}{R^2} - 2\frac{t^2}{D^2}\right]. \tag{1.12}$$

We can now evaluate (1.10) and (1.11):

$$P = c\epsilon_0 \frac{\pi}{2} E^2 R^2 \exp\left[-2\frac{t^2}{D^2}\right], \tag{1.13}$$

$$\mathcal{E} = c\epsilon_0 \left(\frac{\pi}{2}\right)^{3/2} E^2 R^2 D. \tag{1.14}$$

Introducing the ubiquitous normalisation

$$\boldsymbol{a} = \frac{e\boldsymbol{E}}{m_e \omega c} \tag{1.15}$$

for the field amplitude, we can rearrange to a more convenient form. Intensity (irradiance) is given by

$$I = 4\pi^2 P_0 \frac{a^2}{\lambda_0^2} = 2.763 \times 10^{10} \left(\frac{a^2}{\lambda_0^2}\right) \text{Wm}^{-2}, \tag{1.16}$$

beam power by

$$P = 2\pi^3 P_0 \frac{a^2 R^2}{\lambda_0^2} = 4.298 \times 10^{10} \left(\frac{a^2 R^2}{\lambda_0^2}\right) \text{W}, \tag{1.17}$$

and the total energy for a Gaussian pulse with duration D seconds

$$\mathcal{E} = \sqrt{2\pi^7} P_0 \frac{a^2 R^2 D}{\lambda_0^2} = 5.387 \times 10^{10} \left(\frac{a^2 R^2 D}{\lambda_0^2}\right) \text{J}. \tag{1.18}$$

Here $P_0 = \epsilon_0 m_e^2 c^5 / e^2 = 6.931 \times 10^8$ W is a convenient unit of power. These values are calculated for CP light, and should be halved for LP.

1.4 Linear Plasma Response

The above analysis gives the basic mathematical description of light in a vacuum, in a plasma medium this is complicated by currents induced by the laserfields. The equation of motion for an electron is

$$m_e \frac{\mathrm{d}\boldsymbol{v}}{\mathrm{d}t} = -e\left(\boldsymbol{E} + \boldsymbol{v} \times \boldsymbol{B}\right), \tag{1.19}$$

where m_e and e are the electron rest mass and charge respectively, $\boldsymbol{E}$ and $\boldsymbol{B}$ correspond to the rapidly varying fields of the laser and $\boldsymbol{v}$ is the electron velocity. The electric field of an arbitrarily polarised laser is given by (1.1), and from this we may determine the electron velocity. Analytically, we take the plane-wave approximation. This is valid for large spot-size lasers in the long-pulse approximation such that pulse duration $D \gg 2\pi/\omega_p$ [54] and the pulse amplitude does not vary much over a laser period. Hence, plasma electron wave excitation and

all ponderomotive force may be considered to be negligible. We hence take $\boldsymbol{v} \simeq \boldsymbol{v}_\perp$. Linearising (1.19) with $\mathrm{d}/\mathrm{d}t = -i\omega$, and taking the nonrelativistic limit such that $\boldsymbol{v} \times \boldsymbol{B} \ll \boldsymbol{E}$, the velocity is found as

$$\boldsymbol{v}_\perp = \Re\left\{-\frac{ie}{m_e\omega}\hat{\boldsymbol{e}}_{\boldsymbol{p}} E_0 \exp\left(i\phi\right)\right\}. \tag{1.20}$$

The inhomogeneous electromagnetic wave equation is

$$\nabla^2 \boldsymbol{E} - \frac{1}{c^2}\frac{\partial^2 \boldsymbol{E}}{\partial t^2} = -\mu_0 \frac{\partial \boldsymbol{J}}{\partial t}, \tag{1.21}$$

where we take the current density $\boldsymbol{J}$ to be dominated by the transverse motion of the electrons only $\boldsymbol{J} \simeq \boldsymbol{J}_\perp = -en_e\boldsymbol{v}_\perp$. Here n_e is the electron number density. Using $\boldsymbol{a} = e\boldsymbol{E}/m_e\omega c$, and defining the quantities

$$\tilde{n}_e = \frac{n_e}{n_0}, \tag{1.22a}$$

$$\omega_p^2 = \frac{e^2 n_0}{m_e \epsilon_0}, \tag{1.22b}$$

$$k_p = \frac{\omega_p}{c}, \tag{1.22c}$$

where n_0 is the background electron density and ω_p and k_p are the plasma frequency and wavenumber respectively. The corresponding wave equation in plasma is therefore

$$\nabla^2 \boldsymbol{a} - \frac{1}{c^2}\frac{\partial^2 \boldsymbol{a}}{\partial t^2} = k_p^2 \tilde{n}_e \boldsymbol{a}. \tag{1.23}$$

Under the assumption that the plasma is homogeneous, the density profile n_0 is constant. Consider a simple plane wave $\boldsymbol{a} = \hat{\boldsymbol{e}}_{\boldsymbol{x}} \exp[i(kz - \omega t)]$. By substituting this and $\tilde{n}_e = 1.$ into (1.23), we can recover the normal plasma dispersion relation as

$$\omega^2 = k^2c^2 + \omega_p^2, \tag{1.24}$$

which provides the basic information about how light propagates in a plasma, graphed as the solid line in figure 1.2(a). There is a cutoff frequency at $\omega = \omega_p$ below which k becomes imaginary, and therefore light of that frequency cannot propagate. This corresponds to a particular electron density known as the critical density

$$n_c = \frac{\omega^2 m_e \epsilon_0}{e^2}\ (\mathrm{m}^{-3}), \tag{1.25}$$

and we may further summarise the dispersion relation by taking the refractive index N from the phase velocity $v_p = \omega/k$

$$N = \frac{c}{v_p} = \sqrt{1 - \frac{\omega_p^2}{\omega^2}}. \tag{1.26}$$

1.5 Relativistic Nonlinear Plasma Response

Under relativistic conditions we must make modifications to the above equations as the electron motion becomes relativistic. The Lorentz force is now given as

$$m_e \frac{\mathrm{d}}{\mathrm{d}t}(\boldsymbol{v}\gamma) = -e\left(\boldsymbol{E} + \boldsymbol{v} \times \boldsymbol{B}\right), \tag{1.27}$$

where the lorentz factor of the electron is given by $\gamma = [1 + (p/mc)^2]^{1/2}$. This means we must average the squared momentum over a laser cycle. For LP light this results in a factor half reduction and for CP light this results in a factor unity. We will consider CP light here. The average electron lorentz factor is therefore given by conservation of momentum [55, 56] as

$$\gamma = \sqrt{1 + a^2}. \tag{1.28}$$

This expression is calculated for the average rest-frame of the electron, and ignores and drift motion, or forward momentum the particle acquires. It remains accurate enough for most purposes in the weakly relativistic regime ($a^2 \ll 1$), and numerical modeling calculates the particle motion self-consistently as a matter of course, so it is acceptable. Due to the relativistic mass increase of the electrons, the effective plasma frequency is reduced, varying as $\omega_{p_{\mathrm{eff.}}} = \omega_p/\sqrt{\gamma}$, leading us to the relativistic plasma dispersion relation

$$\omega^2 = k^2c^2 + \frac{\omega_p^2}{\gamma}, \tag{1.29}$$

where now the effective cutoff frequency is reduced, and hence the effective critical density given in (1.25) is raised due to the increase in m. This allows intense light to propagate in traditionally over-dense plasma, a phenomenon known as relativistically-induced transparency. The disperson relation and the electron Lorentz factor are plotted in figure 1.2.

All optical properties have some threshold beyond which they become nonlinear. That is, the intensity of the light itself affects the property in question. The refractive index of a medium is a fundamental optical property, arising from the dispersion relation. It determines the medium response to incoming light, and as seen in (1.29) it can become nonlinear under intense light.

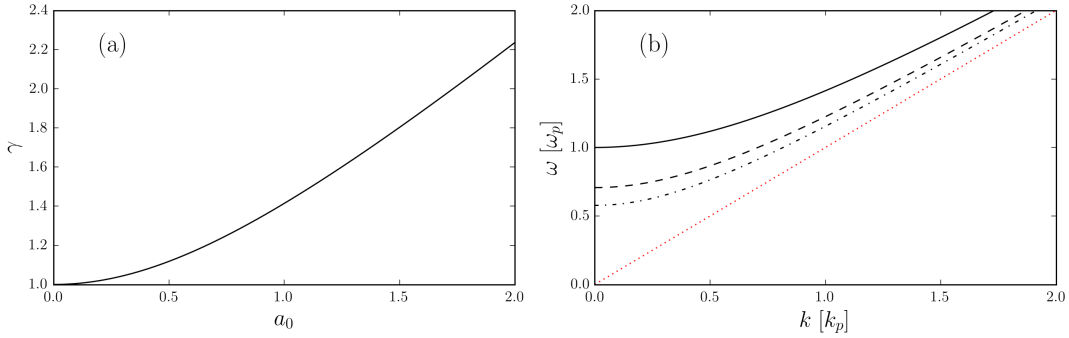

Figure 1.2: (a) A plot of (1.28) up to $a_0 = 2$. (b) A plot of (1.29). The solid, dashed and dot-dashed curves show the dispersion relation for $\gamma = 1$, 2 and 3 respectively, illustrating the reduced cutoff frequency. The dotted red curve shows the vacuum relation $\omega = kc$.

While in plasma the nonlinearity is due to the relativistic mass increase of the electrons, in neutral media it is due to induced polarisation. This is the well-known Kerr optical effect, and may be represented as a linear refractive index N_0 modified by some nonlinear refractive index N_1 proportional to the laser intensity

$$N = N_0 + N_1 a^2. \tag{1.30}$$

This means while there is no hard lower threshold for nonlinear processes to occur, due to the dependence on the square of the light amplitude, their impact is vanishingly small at low light intensity, and proprtionally much more significant at high intensities. This allows us to safely separate linear and nonlinear optical models depending on incident intensity. Modifications to the plasma refractive index may be described in the form of (1.30) by taking a Taylor series of the Lorentz factor, a technique which is very widely employed in the weakly-relativistic regime.

Self-focusing is a fundamental nonlinear process which may occur in any optical medium. It is the process governed by variations in refractive index due to intense light. Real laser beams are not uniform in intensity, and spatial gradients in the intensity result in spatial gradients in the refractive index. This in turn causes a differential change to the speed of light in the medium in areas of high intensity, and distorts the phasefront structure of the light, this turns the rays of the pulse inwards and the beam focuses spontaneously.

In plasma, self-focusing may be categorised to three main sources; thermal, ponderomotive and relativistic. Thermal focusing occurs when the plasma is locally heated, raising its refractive index and therefore acting as a lens in hot areas. Ponderomotive focusing arises due to the fact a plasma is a fluid medium, and density fluctuations naturally alter the refractive index. Finally,

relativistic self-focusing arises from the relativistic mass increase of the electrons as a response to intense laser light. This causes a reduction in the effective plasma frequency, raising the refractive index and causing the plasma to act as a lens. All three of these effects can, and do, occur simultaneously, and determining to what extent each process affects a laser is quite difficult.

Density fluctuations in plasmas are unavoidable, given its fluid nature. An extremely significant source of such fluctuations is found in the laser itself. While for plane waves, particles oscillate in place, and there is no change in the overall plasma density, real lasers are unfortunately not plane waves, with finite durations and spot sizes, the gradients in intensity lead to particle drift. The ponderomotive force may be qualatatively explained as the force which pushes particles out of areas of high field intensity. As a particle oscillates in a laser field with some spatial intensity gradient it will naturally drift down the gradient due to the asymmetry of the forces it experiences. Mathematically, this force $\boldsymbol{F}_p$ can be derived in a few different ways [57, 58], with the result taking the form

$$\boldsymbol{F}_p = -m_e c^2 \nabla \bar{\gamma}, \tag{1.31}$$

where $\bar{\gamma}$ is the time-averaged lorentz factor as given by the laser amplitude (1.28). The ponderomotive force affects both electrons and ions in the same way, there is no polarity effects. However, this is not so to say they are both affected equally. Naturally ions are much heavier, and therefore do not respond as quickly. Very often their ponderomotive motion is disregarded entirely from analytical treatments. This large difference in response leads to space charges forming in the wake of an intense pulse, due to the now mismatched electron and ion densities. This in turn gives rise to the plasma wake and bubble phenomena of fundamental importance to plasma-based particle acceleration.

Due to the dependence on $\nabla\bar{\gamma}$ both the peak intensity of the laser and the pulse dimensions affect how strong the ponderomotive force is. In the weakly relativistic regime, very often ponderomotive effects are disregarded for both ions and electrons. If we assume circularly polarised light, $\gamma = \bar{\gamma}$, and a Gaussian amplitude profile $a = a_0 \exp(-r^2/R^2)$, we may evaluate (1.31) as

$$\boldsymbol{F}_p = m_e c^2 \frac{2ra^2}{R^2\bar{\gamma}} \hat{\boldsymbol{e}}_{\boldsymbol{r}}. \tag{1.32}$$

From this, we can see that the ponderomotive force does indeed push particles in the positive r direction as expected, but in the weakly relativistic regime, we expect $a^2 \ll 1$, so the ponderomotive force will be vanishingly small. This is further compounded by the dependence on

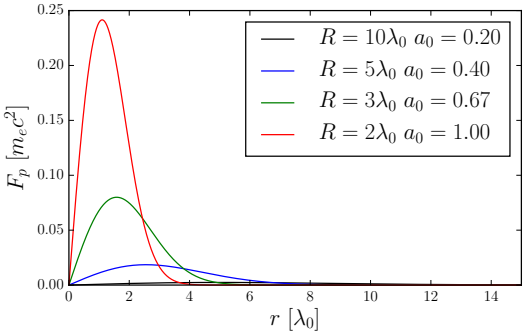

Figure 1.3: Illustrative plot showing the normalised ponderomotive force produced by a laser pulses of varying amplitude and spot size. All four curves represent pulses with an equal amount of total energy, and may be interpreted as a single laser pulse undergoing self focusing. The black curve represents the largest spot size, and exerts a ponderomotive force which peaks at 0.002, wheras the tightly focused red curve peaks at 0.24, over 100 times stronger.

$1/R^2$, which will act to further reduce the ponderomotive force when the spot size is large. In the event that either a^2 becomes large, or R^2 becomes small, the assumption that the ponderomotive force can be neglected is course no longer valid. Figure 1.3 shows how this may occur, illustrating how pulse amplitude and spot size affect the exerted ponderomotive force. It shoiuld be noted that the example curves shown in figure 1.3 contain the same amount of energy ($aR = \text{const.}$), and may therefore be thought of as snapshots of the same pulse, which begins at a modest amplitude and large spot size, safely in the regime where ponderomotive effects should be small, but then subsequently self-focuses, and dramatically increases the amount of ponderomotive force exerted.

1.6 Generation of Quasistatic Magnetic Fields and Related Effects

Magnetic fields in plasmas introduce another class on nonlinearity, as plasmas consist of charged particles, any magnetic field imposed upon a plasma will influence the motion of the plasma particles. There are many different mechanisms for the generation of magnetic fields in plasmas. These range from large-scale, relatively low strength fields such as may emerge spontaneously from a turbulent plasma, so-called dynamo action [59–61], to small-scale, short-lived, much stronger phenomena as may be produced by an intense laser. In this work we are more concerned with the latter.

Of laser-generated magnetic fields, most commonly seen are the thermoelectric magnetic field

[62, 63] arising from electron transport due to mismatched temperature and density gradients. Such fields may also occur in the absence of a laser, where the mechanism is known as the 'Biermann battery. [64]. In either case the growth rate of such fields is proportional to the temperature and density gradients

$$\frac{\partial \boldsymbol{B}}{\partial t} \propto \nabla T_e \times \nabla n_e. \tag{1.33}$$

Magnetic fields also arise from a ponderomotively driven current through a steep density gradient [65–68],

$$\nabla^2 \boldsymbol{B} \propto \nabla n_e \times \nabla I. \tag{1.34}$$

Both of these fields are azimuthal in nature, albeit of opposite sign, and appear along the path of the laser as is propagates into a plasma.

Longitudinal magnetic fields may be generated by the inverse faraday effect [69], in which a static magnetisation $\boldsymbol{M}$ is induced in the plasma following

$$\boldsymbol{M} \propto \boldsymbol{E} \times \boldsymbol{E}^*, \tag{1.35}$$

where $\boldsymbol{E}^*$ is the complex conjugate of $\boldsymbol{E}$. This results in a magnetic field aligned parallel to the path of the laser, rather than perpendicular to it in the case of (1.33) and (1.34). This effect is traditionally restricted to CP light only, as $\boldsymbol{E} \times \boldsymbol{E}^* = 0$ for LP light. However it has been proposed that a LP laser can drive a similar process if it carries OAM [70]. A more exotic method of generating longitudinal magnetic fields is a so-called 'light spring' setup [71–73], in which a superposition of LG mode beams of different azimuthal indices and central frequency produce a helical beam envelope, and hence a helical plasma wake, which drives an azimuthal current behind the pulse. Both of these effects rely on the angular momentum of light, either spin or orbital, to couple into the plasma and provide the neccessary circulating electron currents.

Both spontaneously appearing magnetic fields and those generated and imposed from external sources have the common effect of changing how a plasma responds to incoming light. In this work we will consider a constant field along the laser propagation direction $\boldsymbol{B} \parallel \boldsymbol{k}$, and CP light. From this starting point, we can examine how the electron motion will be modified. If we consider (1.27), now with a nonzero $\boldsymbol{B}$, we immediately see that wheras before the $\boldsymbol{v} \times \boldsymbol{B}$ term vanished due to neglible contributions to the electron motion from the laser magnetic fields, now the external field will cause continually bend the particle motion in the xy-plane. If left to its own devices, a moving charge particle in a static magnetic field will travel in a circle,

performing so-called cyclotron motion, and the radius of this circle termed the Larmor radius r_L gyrating at the cyclotron frequency ω_c;

$$r_L = \frac{\gamma m v}{|q|B}, \tag{1.36a}$$

$$\omega_c = \frac{|q|B}{\gamma m}. \tag{1.36b}$$

From here, the modified dispersion relation

$$\omega^2 = k^2 c^2 + \omega_p^2 \frac{\eta}{\gamma}, \tag{1.37}$$

can be found. Here, η is a relativistically modified factor relating to the external field $\eta = (1 - \delta\omega_c/\gamma\omega)^{-1}$, where δ again describes the polarisation state of the laser light as per (1.2). This result is consistent with that given in previous work [69, 74], and illustrated in Figure 1.4. It shows that when $\omega_c \neq 0$, cutoff frequencies for RCP and LCP light take different values. These may be obtained by setting $k = 0$ in (1.37) and have the general form $\omega_{R,L} = [(\omega_c/2\gamma)^2 + \omega_p^2/\gamma]^{1/2} \pm \omega_c/2\gamma$. The cutoff frequency is reduced down to ω_L for LCP light, and increased up to ω_R for RCP light. While transparency is increased for LCP light, there is still a cutoff frequency below which no propagation is possible. Conversely, RCP waves may also propagate in whistler mode, creating an opaque frequency range $\omega_c/\gamma < \omega < \omega_R$.

The dispersion relation above shows that the extra complexity added to laser propagation characteristics from the magnetic field alone is considerable. The combination of relativistic and magnetic nonlinearity means that study of intense lasers in magnetised plasma is a challenging field. Magnetised plasma effects stem from the particle motion being modified due to imposed magnetic fields. When this motion is relativistic, these processes change in ways that are not always obvious. For example, the relativistic Larmor radius does not grow linearly with velocity, as relativistic kinematics must be employed. Similarly, the Lorentz factor in a magnetised plasma does not scale the same as in an unmagnetised plasma. This gives rise to combined relativistic-magnetic nonlinearity resulting in modifications to familiar phenomena such as self-focusing, and entirely unique phenomena such as relativistically induced opacity (discussed in chapter 2).

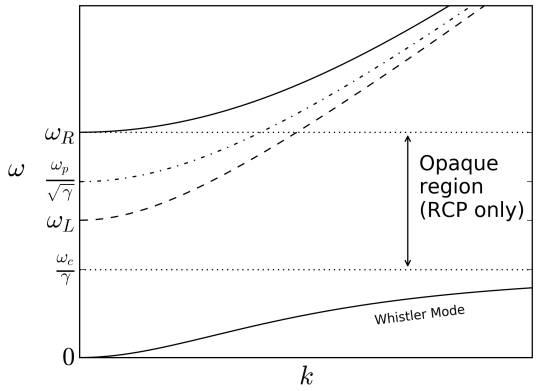

Figure 1.4: The magnetised plasma dispersion relation. The solid curve represents RCP light, the dashed curve represents LCP light and the dot-dashed curve indicates the unmagnetised dispersion for comparison. Here ω_c is arbitrarily less than ω_p, as the relationship between the two is not important here.

1.7 Particle-in-Cell Simulation

In kinetic plasma modeling, we aim to simulate individual charged particles interacting in order to study their collective behaviour. Typically kinetic models are used to understand very fast, and very small-scale processes, such as interactions between plasmas and lasers. This in constrast to fluid models, for example, which are much more suited to larger scale processes that occur over longer timescales. Kinetic modeling would ideally simulate each particle interacting directly. However, attempting this is impossible, due to the vast number of particles in a real system, and the vast number of interactions each particle experiences. Instead, to simplify the problem we use particle-in-cell (PIC) codes. A PIC code is a tool to model a plasma as a kinetic system, while staying within the limits of computation. The PIC method can be applied in one to three spatial dimensions, and may be integrated into multiscale simulations via hybrid algorithms or bridging codes, making it a versatile tool in the plasma physics arsenal.

The two key aspects of modelling plasma processes are the fields and the particles. Fields are discretised onto points in a grid, and particles are allowed to move freely around within the grid. Generally particles are initialised at regular intervals on the grid, giving rise to the name particle-in-cell.

Simulating the vast number of particles present in a real system is not practical, so particles are amalgamised into so-called 'macroparticles'. Each macroparticle represents a number of real particles of the same species, with macroparticles from different species distinguished by their charge-to-mass ratio (q/m). Therefore, we can describe a macroparticle representing an electron via an internal q/m of -1, normalised to the elementary charge and the electron mass.

Correspondingly, a Hydrogen ion would have a q/m of 1/1836, with now positive charge and a mass corresponding to m_p/m_e. Heavier ions, and ions with different ionisation states can be initialised in a similar manner. Since the particle trajectory is determined by the charge-to-mass ratio, this means macroparticles follow the same paths real particles would. Each macroparticle is weighted according to its representative size, and this is taken into account such that the calculated charge and current densities are correspondant to those of a real system. This adds a new parameter we must consider when designing simulations. In addition to the familiar spatial step size, and time interval of numerical modeling, we must also choose the macroparticle count. As with the grid spacing and timestep, the choice of macroparticle granularity depends on the problem being investigated. In general, if features of the particle distribution function are (or are important to) the object of study, a high macroparticle count is required. The aliasing arising from a coarse grid spacing and timestep are further compounded upon by the possibility of errors due to particle phase-space aliasing arising from a low particle count. Such errors are hard to identify, as they do not typically affect the numerial stability of the simulation itself. This means that without proper dilligence, macroparticle aliasing can easily be missed, or worse, misinterpreted as genuine results.

At its core, the PIC method aims to solve the Vlasov equation

$$\frac{\partial f}{\partial t} + \boldsymbol{v} \cdot \nabla f + q(\boldsymbol{E} + \boldsymbol{v} \times \boldsymbol{B}) \cdot \frac{\partial f}{\partial \boldsymbol{p}} = 0, \tag{1.38}$$

in a Lagrangian specification in order to determine the distribution function $f(\boldsymbol{r}, \boldsymbol{p}, t)$ of each simulated particle species. In order to do this, Maxwell's equations are used to determine the fields

$$\nabla \times \boldsymbol{E} = -\frac{\partial \boldsymbol{B}}{\partial t}, \tag{1.39a}$$

$$\nabla \times \boldsymbol{B} = \frac{1}{c^2}\frac{\partial \boldsymbol{E}}{\partial t} + \mu_0 \boldsymbol{J}, \tag{1.39b}$$

$$\nabla \cdot \boldsymbol{E} = \frac{\rho}{\epsilon_0}, \tag{1.39c}$$

$$\nabla \cdot \boldsymbol{B} = 0, \tag{1.39d}$$

and the particle equations of motion are used to determine the trajectories of individual

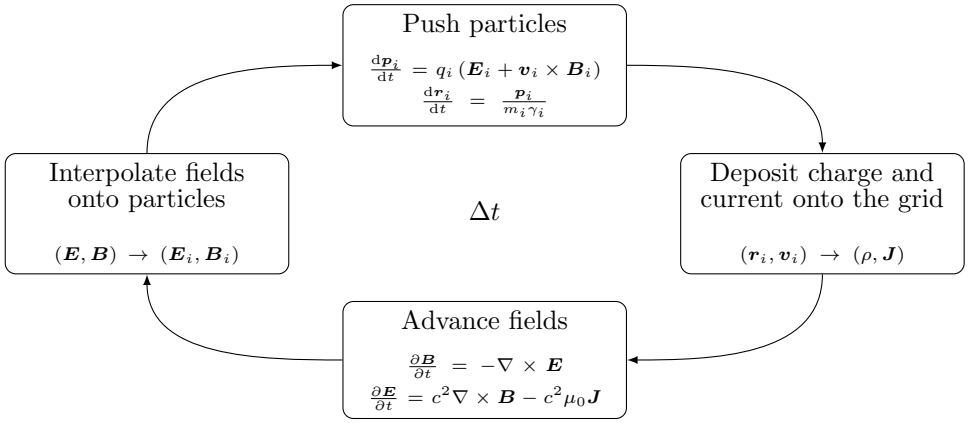

Figure 1.5: The basic PIC cycle

macroparticles

$$\frac{\mathrm{d}\boldsymbol{p}}{\mathrm{d}t} = q\left(\boldsymbol{E} + \boldsymbol{v} \times \boldsymbol{B}\right), \tag{1.40a}$$

$$\frac{\mathrm{d}\boldsymbol{r}}{\mathrm{d}t} = \frac{\boldsymbol{p}}{m\gamma}. \tag{1.40b}$$

For an electrostatic (ES) PIC code, we solve only (1.39c) and (1.40), with the assumption that $\boldsymbol{E} = -\nabla\phi$ where ϕ is the electrostatic potential. For an EM PIC code we solve (1.39a), (1.39b) and (1.40), while (1.39c) and (1.39d) are automatically resolved as part of the simulation setup and boundary conditions. If (1.39d) is satisfied at $t = 0$, it will remain satisfied throughout the simulation, and if the charge continuity equation

$$\nabla \cdot \boldsymbol{J} + \frac{\partial \rho}{\partial t} = 0 \tag{1.41}$$

is satisfied via a charge-conserving current deposition scheme, then (1.39c) need only be satisfied at $t = 0$, usually achieved via corrections to the field as the simulation is initialised. This allows realistic simulations to be performed with only one particle species if desired. If a non-charge conserving deposition scheme is used, then $\boldsymbol{E}$ must be adjusted at every timestep in order to keep (1.39c) satisfied.

The classic PIC algorithm is shown in figure 1.5, consisting of four main steps. First, the electric and magnetic fields on each particle are determined by linearly interpolating from the nearest grid points. Then, particles are moved according to these fields. This is most commonly achieved using a scheme known as the Boris pusher [75], which has good energy-conserving properties and a reasonable computational overhead. From the new positions, currents (and charge

densities, if required) are deposited onto the grid. This is usually done using a charge-conserving scheme in accordance with the particle shape factor, which determines the neighbouring grid points to which charge and current are deposited, and the weighting on each point. This is often the most time-consuming step, especially if there are a large number of particles using a high-order shape factor. As such, it is also the step for which good load-balancing is most important. The calculated current density is then used to advance the electric and magnetic fields in time, typically this is achieved using a leapfrog method, making use of quantities staggered in both space and time to achieve a numerically stable integrator, whilst minimising computational cost. Alternate methods of advancing fields, depositing particle quantities and implementations of collisions, ionisation and QED effects vary from code-to-code, and most PIC codes are designed with a particular feature or area of study in mind, therefore it is worth considering the problem at hand when selecting a code.

In addition to the code itself, the simulation parameters must be chosen so that the relevant physics can be resolved, and simulation is stable. Generally speaking, a good starting point is to identify the smallest spatial features and the fastest events a simulation must be able to resolve. In plasma simulation, the Debye length λ_D crops up very often as a constraint on simulation grid spacing. It is given by

$$\lambda_D = \left(\frac{\epsilon_0 k_B T_e}{n_e e^2} \right)^{1/2} \tag{1.42}$$

where ϵ_0 is the permitivity of free space, k_B is the Boltzmann constant, T_e is the electron temperature, n_e is the electron density and e is the elementary charge. This length is a measure of how far an individual particles electrostatic charge has influence, beyond which, the collective properties of the plasma dominate and the charge may be considered 'screened'. This parameter is important to the properties and behaviour of the plasma and so it is an important parameter to consider when designing simulations. Typical values of the Debye length can range from macroscopic values in space-plasmas, to picometer scales inside stars. In laser-produced plasmas at or below the critical density, and heated to keV levels, the Debye length typically falls around the micrometer scale. This provides a first basis for choosing the grid spacing for the simulation.

The second factor to look at for determining appropriate grid spacing is the laser itself. In PIC simulation, the laser fields are initialised piecewise across the cells, and therefore must also be resolved over the course of the simulation. This necessitates a grid resolution (in the laser direction) of at least six times [40] smaller than the central wavelength in order to reasonably resolve the field structures of the laser (naturally higher resolution is more desireable). Typically in laser-plasma experiments, Ti:Sapphire lasers operate at around 800 nm, which would mean

a minumum spatial resolution of 0.1 μm. Frequency doubled lasers, or simulations in which high-harmonic generation (HHG) is expected would require accordingly higher resolution.

Once the spatial resolution is decided, the timestep must be chosen. Resolving particle orbits is usually the main physical consideration when choosing a maximum timestep. Intense lasers cause electrons to follow a characteristic figure-eight motion [76], and ambient magnetic fields introduce cyclotron motion, and once again the expectation of high-harmonics necessitate yet higher resolution to properly resolve the motion. Aside from the physics-based contraints on the timestep, there is also the question of numerical stability.

When attempting to solve differential equations numericallly, the Courant condition gives the limits on both spatial resolution and timestep in order to ensure stability i.e. the solutions to the equations the simulation is trying to solve will converge, and not 'blow up', producing unphysical results. In the case of a PIC simulation modeling n spatial dimensions we may write

$$C = c\Delta t \sum_{i=1}^{n} \frac{1}{\Delta x_i} \leq C_{\max}, \tag{1.43}$$

where Δx_i is the grid spacing along each spatial coordinate, C is the calculated Courant number, $C_{\max}$ is the maximum allowable Courant number, Δt is the timestep and c is the maximum speed information can travel across the grid, the speed of light. If $C \leq C_{\max}$ then the results of the simulation will converge. The exact value of $C_{\max}$ varies depending on how the equation is solved. Explicit methods usually require smaller timesteps in order to maintain stability ($C_{\max} = 1$, for instance), wheras implicit solvers are often more forgiving in this respect and $C_{\max}$ may rise considerably. The technical constraints on simulations, and the physical considerations together inform how a simulation should be designed in order to maximise the efficiency of available computing resources.

In this work, we make use of two PIC codes, namely Osiris [77, 78] and FBPIC [79, 80]. Osiris is a fully explicit 3D code employing finite-difference time domain (FDTD) methods to advance fields and particle trajectories. This 'no-shortcuts' approach produces reliable results, and Osiris has a long track record of use within the plasma physics community. It is designed for large-scale distributed computing, and this method of execution is often unavoidable given the intense nature of simulating laser-plasma interactions. A long 3D simulation involving potentially billions of cells and macroparticles demands a significant investment in terms of computer power.

FBPIC, on the other hand is a relatively new code. It takes advantage of a Fourier-Bessel decomposition algorithm to describe the field geometry around the azimuth. This allows the

particles themselves to move around in 3D, but the field are described by multiple 2D grids describing the various azimuthal modes. This combination of 3D motion and 2D grids is sometimes described as 'quasi-3D' or '2.5D'. All of the time integration in FBPIC is performed in spectral space, this allows for analytical integration of Maxwell's equations,making it a 'dispersion-free' field solver, sidestepping numerical dispersion effects which FDTD methods are prone to [81]. The net result is an accurate code, which executes quickly and at significantly less computational overhead than a fully-3D code, so long as the problem being studied has intrinsic azimuthal symmetry. For the purposes of the laser-plasma interactions of interest to this work, this assumption is valid. A more in-depth comparison of the two codes is given in appendix C, where some specific simulations detailed in chapter 3 are examined.

Chapter 2

Influence of Strong Magnetic Fields on Laser Pulse Propagation

First, we examine the interaction between intense laser pulses and strongly magnetised plasmas in the weakly relativistic regime. An expression for the electron Lorentz factor coupling both relativistic and cyclotron motion nonlinearities is derived for static magnetic fields along the laser propagation axis. This is applied to predict modifications to the refractive index, critical density, group velocity dispersion and power threshold for relativistic self-focusing. It is found that electron quiver response is enhanced under right circularly-polarised light, decreasing the power threshold for various instabilities, while a dampening effect occurs under left circularly-polarised light, increasing the power thresholds. Derived theoretical predictions are tested by one and three-dimensional particle-in-cell simulations.

2.1 Introduction

Static magnetic fields induce cyclotron motion in the charged particles of a plasma. The particles gyrate at a frequency proportional to the applied field, and this motion modifies the optical properties of the plasma. Classical plasma theory is also altered by the relativistic mass increase of electrons when the driving laser amplitude is high enough, and this couples to the magnetic nonlinearity through mass dependence of the cyclotron frequency. In this way, magnetic and relativistic effects are linked, and must be considered together.

This work focuses exclusively on the propagation of circularly polarised light along the direction of an externally applied DC magnetic field. In this case, there is distinct difference between right circular polarisation (RCP) and left circular polarisation (LCP) of the light, which are respectively with clockwise and anticlockwise rotation along the laser propagation direction. A dramatic effect of magnetisation on RCP light in the whistler mode is greatly increased plasma transparency, which allows for novel schemes of efficient, magnetically guided plasma acceleration [74]. This is of particular relevance to the fast-ignition scheme of inertial confinement fusion, which relies heavily on precise deposition of energy by accelerated particles [82]. This motivates an understanding of the physics of intense laser interactions with highly magnetised plasma. For lasers on the order of μm wavelength, it would require a magnetic field on the order of 10^4 Tesla, in order to bring the plasma in order to operate in the whistler regime. Such extremely high fields are challenginging to reach experimentally, however the generation of ultra-strong magnetic fields has received considerable interest in the last decade.

Long-lasting fields of around 100 Tesla can now be readily produced with conventional techniques [83, 84]. Higher strength fields operating at shorter timescales are can also be produced [85]. High power laser interaction with dense plasma can even produce quasi-static magnetic fields at the 10^5 T level [86–89]. By irradiating a capacitor-coil target with kilo-Joule high power lasers, it has been demonstrated experimentally that high magnetic fields at kT level can be produced [7, 8]. The latter is particularly interesting for a number of applications such as inertial confinement fusion [34].

Even in the linear wave regime, the magnetic fields result in unique effects of wave propagation. Observations of anomalous radio waves were documented as early as 1894, termed whistlers due to the descending tone heard as the waves were picked up on receivers. Explanations of the physical processes underlying them developed in the 1950s as general understanding of plasma physics advanced [**?**]. The comparatively high frequency of laser light compared to radio waves has, until relatively recently, precluded the investigation of whistler mode lasers. However, advances in laser technology and the creation of high strength magnetic fields now allow access to this parameter regime, and have spurred interest in the combination of magnetic and relativistic plasma effects.

Nonlinear propagation of lasers in unmagnetised plasma has been widely studied. The key physics involving the propagation of a laser pulse in a plasma concern the transverse evolution [54, 90, 91], typically characterised by self-focusing (SF) processes, and the longitudinal evolution, governed by processes such as self-phase modulation (SPM), [92, 93] which may act to compress an already short pulse in plasma further. Recently, work has been done determin-

ing the effect magnetisation plays on the propagation of lasers. The transverse evolution of lasers in weakly-relativistic magnetised plasmas is investigated by [94, 95], who conclude that magnetic field enhances self-focusing of RCP pulses. Longitudinal effects are investigated by some researchers [96–98], who conclude that SPM may be enhanced for RCP light, or inhibited for LCP light, by an applied magnetic field.

In this chapter we consider the strongly magnetised regime, in which the electron cyclotron frequency is on the order of the incident laser frequency. In this case, magnetic fields dramatically influence the magnitude and rate of the SF and SPM processes with a much lower power threshold for RCP light. In chapter 3.2, a theory model is presented for a regime where the laser pulse duration is relatively long so that ponderomotive force and subsequent density perturbations can be neglected. Therefore we focus on the effect of strong magnetic fields on relativistic SF and relativistic SPM. Also the self-generated magnetic fields [40, 99–102] are neglected as compared with the externally applied magnetic field. Results from self-consistent three-dimensional particle-in-cell simulations are presented in chapter 2.3, which confirm the theory predictions given in section 3.2. Simulations also illustrate complicated longitudinal and transverse couplings at later stage of the laser propagation.

2.2 Theory Model

2.2.1 Dispersion Relation

We aim to describe the characteristics of propagation of a laser beam in a magnetised underdense plasma, with the static magnetic field aligned along the propagation axis of the laser and with the cyclotron frequency comparable to the laser frequency. We may do this by generalisation of the treatment used to study Faraday rotation [103].

We have following expression for the particle motion,

$$\boldsymbol{v}_\perp = \Re\Big\{ -\frac{i\eta eE}{m_e\omega\gamma}\hat{\boldsymbol{e}}_{\boldsymbol{p}} \exp\left[i(kz-\omega t)\right] \Big\}. \tag{2.1}$$

Reminding ourselves of the notation $\eta = (1-\delta\omega_c/\gamma\omega)^{-1}$, we also define $B = \omega_c/\omega$ for further convenience. We may construct an implicit expression for the time-averaged electron Lorentz factor

$$\gamma = \sqrt{1+\left(\frac{eE\eta}{m_e\omega c}\right)^2}. \tag{2.2}$$

This, in combination with (1.37) we may immediately obtain the normalised phase velocity as $\beta_p = \left(1-(\eta/\gamma)(\omega_p/\omega)^2\right)^{-1/2}$. The plasma refractive index N and dielectric function ϵ are

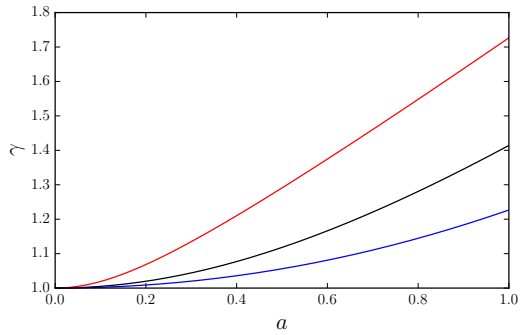

Figure 2.1: The relationship between γ and a for CP light. The black line shows the unmagnetised curve conforming to $\gamma = \sqrt{1+a^2}$. The red curve shows RCP light with a magnetic field strength $B = 0.5$, and the blue curve shows the relationship for LCP light, also for $B = 0.5$.

related by $\epsilon = N^2 = 1-(\eta/\gamma)(\omega_p/\omega)^2$. We may also obtain the normalised group velocity from (1.37) as

$$\beta_g = N\left\{1+\frac{n\eta^2\delta B}{2\gamma^2}\left[1+\frac{a^2\eta^3}{2\gamma^2}\left(1-\frac{a^2\eta^3\delta B}{2\gamma^3}\right)^{-1}\right]\right\}^{-1}, \tag{2.3}$$

where we have used $\gamma = \sqrt{1+a^2\eta^2}$ and $n = (\omega_p/\omega)^2$. RCP light may propagate in the whistler mode, where $B/\gamma > 1$ and hence $N > 1$. Under these conditions, propagation is possible in overdense plasmas [104].

Extra care must be taken for intense light in the whistler mode. Due to relativistic electron mass increase, it is possible for the effective cyclotron frequency to be lowered enough that it approaches the laser frequency and the plasma is returned to a resonant state.

As (2.2) is implicit, it is not immediately plottable. However, solving (2.2) for a results in

$$a = \left(\frac{\gamma^2-1}{\eta^2}\right)^{1/2}, \tag{2.4}$$

which is plottable with γ as the domain. The result may then be used to numerically interpolate for $\gamma(a)$. In weakly magnetised plasmas, this results in a slighly modified curve, shown in figure 2.1, LCP light shows a flattening of the curve, wheras RCP light sees the curve steepen. As the magnetic field is raised further, LCP light continues to be damped but RCP light undergoes more complicated changes due to the presence of the cyclotron resonance point at $B = 1$. Figure 2.2 shows how the curve changes for RCP light as B is raised above 1. We see that the curves become multi-valued when $B > 1$. Physically, electrons will adhere to the curve up to the inflection point, denoted by dots in Figure 2.2 and mathematically described by solving $\mathrm{d}a/\mathrm{d}\gamma = 0$ in (2.4). The physical explanation for this is found by considering what the lorentz

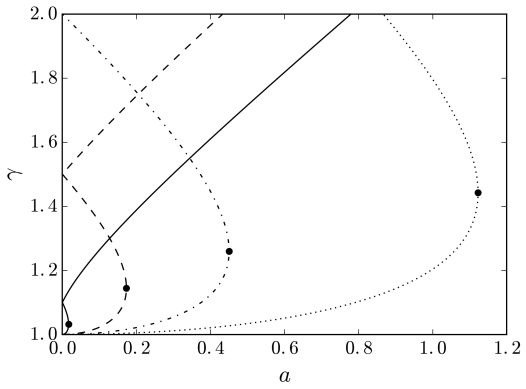

Figure 2.2: The calculated relationship between γ and a for RCP light in the whistler mode. The solid, dashed, dot-dashed and dotted curves show $B = 1.1$, 1.5, 2 and 3, respectively. The black points on each curve correspond to critical values (a_c, γ_c) described in the text. Physically, γ must always take the lowest value available when $a < a_c$. For $a > a_c$ the plasma is highly absorbing and the actual electron Lorentz factor can vary over many orders of magnitude.

factor represents. The cyclotron frequency of a particle is determined by the ambient magnetic field strength, and the mass of the particle, as per (1.36b). In this case the magnetic field is fixed, but the particle mass is not. As the electrons gain energy, their mass increases, and the effective cyclotron frequency is reduced. Taking an extremely strong magnetic field $B > 1$, the effective cyclotron frequency is initially above the reonance frequency, however when the cyclotron frequency is reduced back to cyclotron resonance, any further attempts to increase the kinetic energy of the electrons is instead subject to resonant absorption. The amplitude at which this begins to occur may be expressed in terms of B as a critical light amplitude a_c or critical Lorentz factor γ_c

$$a_c = (B^{2/3} - 1)^{3/2}, \tag{2.5a}$$

$$\gamma_c = B^{1/3}. \tag{2.5b}$$

These quantities do not correspond directly to the resonant point of $B/\gamma = 1$, rather they represent the point at which strong heating begins and large amounts of energy are transfered from the laser to the bulk plasma. As B is increased, the critical point is increased in turn.

The frequency gap associated with RCP light results in an opaque region close to the resonant point occupying the range $(\gamma - n) < B < \gamma$. In reality, this is a poor definition of the actual range at which a laser may still propagate in the plasma, as strong absorption occurs even outside this region. As a result, the insight gained from this is of little practical use. However, at the very least we can estimate the upper bound as γ_c. This improves our estimate

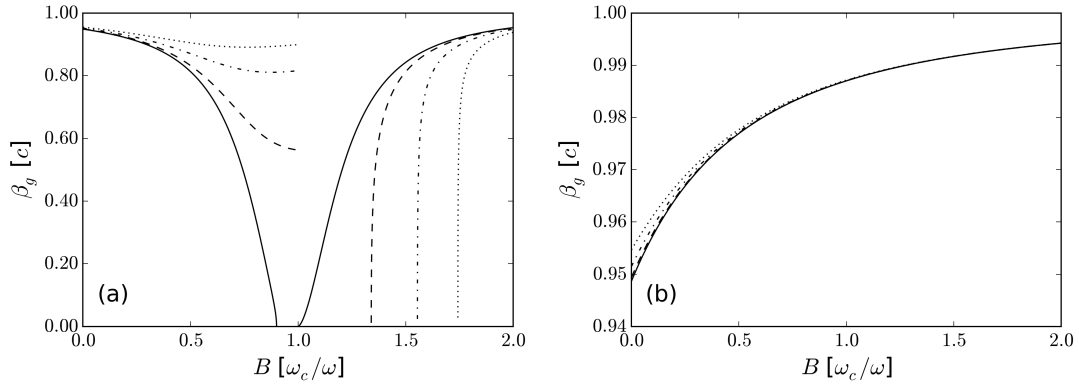

Figure 2.3: Calculated group velocity for light of varying intensity in a plasma of constant density $n = 0.1$. the solid, dashed, dot-dashed and dotted lines correspond to $a = 0$, 0.1, 0.2 and 0.3, respectively. (a) RCP light. The values of β_g when $B \simeq 1$ are in reality quite different from those calculated due to the finite nature of real pulses. Plasma absorption and heating begins before the peak of the pulse can act to reduce to effective cyclotron frequency. (b) LCP light. Tends asymptotically towards $\beta_g = 1$ with increasing B.

to $(\gamma - n) < B < \gamma^3$. We show the effect of increasing a on β_g in Figure 2.3.

2.2.2 Transverse Properties

Analytically we consider a regime where the laser pulse is relatively long so that the longitudinal motion of electrons due the longitudinal ponderomotive force can be neglected. Also we consider a regime where the laser intensity is weakly relativistic so that the density modification due to the transverse ponderomotive force can be neglected during the laser interaction. The numerical simulations detailed in section 2.3 show that this approximation is justified during the early stages of propagation, although nonlinear evolution at later stages leads to the development of very complicated structures that cannot be described by this analytical model.

Consider a laser pulse similar to (1.1):

$$\boldsymbol{a} = \Re\left\{\hat{\boldsymbol{e}}_{\boldsymbol{p}} a \exp\left[i(kz - \omega t)\right]\right\}, \tag{2.6}$$

where the amplitude term is a slowly-varying envelope function $a(r, z, t)$. The evolution equation of the laser envelope is obtained by substituting (2.6) into (1.23), and evaluating it under the slowly varying envelope approximation (SVEA) [54]. Using a generic dispersion relation $\omega^2 = k^2c^2 + \sigma\omega_p^2$ where σ is a constant typically associated with the laser power of a finite-width beam [90]. Physically this constant relates to ponderomotive cavitation along the beam axis, which acts to reduce the effective plasma frequency in the presence of a powerful laser.

Generally speaking the higher the power, the smaller σ becomes, ranging between $0 \leq \sigma \leq 1$.

Now, let $a(r, z, t) = a(r, \xi, \tau)$, where $\tau = t$ and $\xi = z - v_g t$ with the assumption that $v_p v_g \sim c^2$, and therefore $v_g \sim kc^2/\omega$. Then we can obtain

$$\left(2i\frac{\partial}{\partial\tau} + \nabla_\perp^2 + \sigma\frac{\omega_p^2}{\omega^2}\frac{\partial^2}{\partial\xi^2}\right)a = \left(\frac{n_e\eta}{\gamma} - \sigma\right)a, \tag{2.7}$$

where $\nabla_\perp^2 a = r^{-1}\partial/\partial r(r\partial a/\partial r)$ is the radial component of the Laplacian and the normalisations $\tilde{\tau} = (\omega_p^2/\omega)\tau$, $\tilde{\xi} = k_p\xi$, and $\tilde{r} = k_p r$ have been used, with the tildes henceforth dropped for convenience. In accordance with the SVEA, we discard some terms containing second-order derivatives $\partial^2/\partial\tau^2$ and $\partial^2/\partial\tau\partial\xi$ from (2.7). The second order terms $\nabla_\perp^2$ and $\partial^2/\partial\xi^2$ are allowed to remain as these terms govern processes that are of interest. Specifically, $\nabla_\perp^2$ governs the transverse diffraction and hence also self-focusing, and $\partial^2/\partial\xi^2$ governs longitudinal spreading due to linear plasma dispersion, and hence also self-compression. The right hand side of this equation is a nonlinear source term, governing the magnitude of both self-focusing and self-compression.

To obtain the laser power threshold for self-focusing, one may consider a stationary solution and a laser pulse with long longitudinal profile. To further simplify calculations, an analytical form for the electron Lorentz factor is required. The weakly relativistic approximation assumes that γ remains close to 1. This is usually satisfied when $a^2 \ll 1$. However, magnetisation introduces the additional factor η. If we consider $\gamma \sim 1$, then $\eta \sim \eta_0 = (1 - \delta B)^{-1}$. When $B \simeq 1$, $\eta_0^2 \gg 1$ and so we must modify the conditions to $a^2\eta_0^2 \ll 1$, under which we may consider the weakly-relativistic approximation to be still satisfied. This effectively limits the scope of application of this theory to only the low-B or very high-B regime for RCP light, but increases the amplitude range we may consider for strongly magnetised LCP light.

Performing a Taylor expansion of (2.2) yields

$$\gamma \approx 1 + \frac{a^2\eta_0^2}{2}. \tag{2.8}$$

If we make the assumption that the beam has a constant transverse profile, which does not vary along ξ or τ we can examine the stationary solutions to the envelope equation. Taking $\partial a/\partial\tau = 0$ and $\partial^2 a/\partial\xi^2 = 0$, then substituting (2.8) into (2.7) with the approximation $\eta/\gamma \approx \eta_0 - a^2\eta_0^4/2$, one can obtain the stationary envelope equation for a laser beam in a magnetised plasma

$$\nabla_\perp^2 a - (\eta_0 - \sigma)a + n_e\frac{\eta_0^4}{2}|a|^2 a = 0. \tag{2.9}$$

Solving this equation yields the radial profile for a beam of a given power, indicated by assigning a value $\sigma \leq 1$. Such beam profiles represent trapped beams, undergoing self-focusing. Many solutions to this problem exist, found by solving (2.9) via the shooting method, detailed extensively in [54, 90]. We are interested in the minimum power required to trap a beam and induce self-focusing. In this threshold case, we take $\sigma = 1$, signifying a low power, and hence eliminate the ponderomotive force, setting $n_e = 1$. We may recast (2.9) via a change of variables, according to the general form $\nabla_\perp^2 a - \epsilon_1 a + \epsilon_2 a^3 = 0$, where ϵ_1 and ϵ_2 are arbitrary coefficients. We may use the relations $a = \alpha(\epsilon_1/\epsilon_2)^{1/2}$ and $r = \rho\epsilon_1^{1/2}$ to transform between $a(r)$ and $\alpha(\rho)$, where $\alpha(\rho)$ is the solution of $a(r)$ with $\epsilon_1 = \epsilon_2 = 1$. This may be evaluated numerically with the boundary conditions $\mathrm{d}\alpha(0)/\mathrm{d}\rho = 0$ and $\alpha(\infty) = 0$. Recasting and evaluating (2.9) for the beam power via the relation between amplitude and intensity in vacuum $I = \epsilon_0 c|E|^2$, numerically evaluating and reverting to dimensional quantities yields the critical power for self-focusing

$$P_c = 1.62\times10^{10}\eta_0^{-4}\left(\frac{\omega}{\omega_p}\right)^2 [W]. \tag{2.10}$$

This result is consistent with previous work [54, 69] i.e. focusing effects are stronger at higher densities, and the additional term η_0^{-4} relates to the magnetic field. This term reduces to unity for $B = 0$, making the result generally applicable. The corrective term suggests that the magnetic field strongly alters the threshold for self-focusing by a factor of $\eta_0^{-4} = (1-\delta B)^4$. The form of the adjustment is reversed for RCP and LCP light and is shown in Figure 2.4. It shows that the SF power threshold is significantly reduced for RCP light near $B \sim 1$. This analysis implies that at $B = 1$ the threshold power drops to zero. In reality however, this is the point at which cyclotron resonance occurs, and the plasma becomes opaque in the low-power regime and strongly absorbing at high light power. Resonant effects preclude the exploitation of this parameter regime for anything other than plasma heating. Conversely for LCP light, the SF power threshold increases monotonically with B.

Alternatively, starting with Eq. (2.7), assuming a Gaussian transverse amplitude profile such as by $a(\tau) = A(\tau)\exp(-r^2/R^2(\tau))$, it can be shown, by either source-dependant expansion [105] or variational methods [106], that the beam waist evolution of a CP laser pulse can be described by

$$\frac{\mathrm{d}^2R}{\mathrm{d}\tau^2} = \frac{4}{k^2R^3}\left(1 - \frac{P}{P_c}\right), \tag{2.11}$$

where critical power is given by $P_c = 1.74\times10^{10}\eta_0^{-4}(\omega/\omega_p)^2$ [W], which is only slightly different from that given in (2.10).

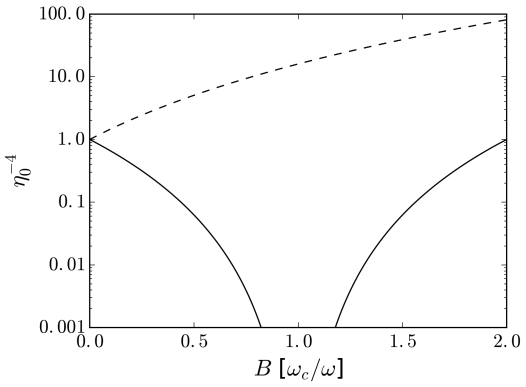

Figure 2.4: The adjustment to the critical power for self-focusing as induced by an applied magnetic field. The solid curve represents the adjustment for RCP light, the dashed curve for LCP light.

2.2.3 Longitudinal Properties

For short pulses, one can consider the evolution of the longitudinal profile of a laser pulse in magnetised plasmas due to SPM by use of (2.7). The phase change due to nonlinearity on the right-hand side of this equation is given by

$$\Delta\phi = \frac{1}{2}\int^{\tau} \eta_0(1-n_e) + \frac{n_e\eta_0^4}{2}|a|^2 \mathrm{d}\tau'. \tag{2.12}$$

where we have replaced σ from the generic dispersion relation with η_0 from the linear magnetised dispersion relation, and the result taylor-expanded. The corresponding frequency change is given by $\Delta\omega = -\partial(\Delta\phi)/\partial t$. Alternatively, the effect can be demonstrated directly for a specific set of parameters. For a temporal pulse profile $a(t)$, the instantaneous phase of the wave after propagating a distance L into a homogeneous plasma is given by $\phi = \omega t - NkL$. In this case the frequency change may be estimated from $\omega = \partial\phi/\partial t$ as

$$\Delta\omega = -\frac{\pi L}{N}\frac{n_e}{n_c}\left(\frac{a\eta^4}{\gamma^3 + \delta B a^2\eta^3}\right)\frac{\partial a}{\partial t}, \tag{2.13}$$

where L is normalised to $2\pi/k$. This is illustrated for RCP and LCP light in Figure 2.5. The SPM of the laser pulse leads to the compression of the longitudinal profile of the laser pulse. In the weakly relativistic case, the compression level is found by letting $(\omega_p^2/\omega^2)(\partial^2/\partial\xi^2) \sim \eta_0^4 a^2/2$ in (2.7). Therefore, the laser pulse duration can be compressed to the level

$$L_p \approx \frac{\sqrt{2}}{k_p}\frac{\omega_p}{\omega}(\eta_0^2 a)^{-1}. \tag{2.14}$$

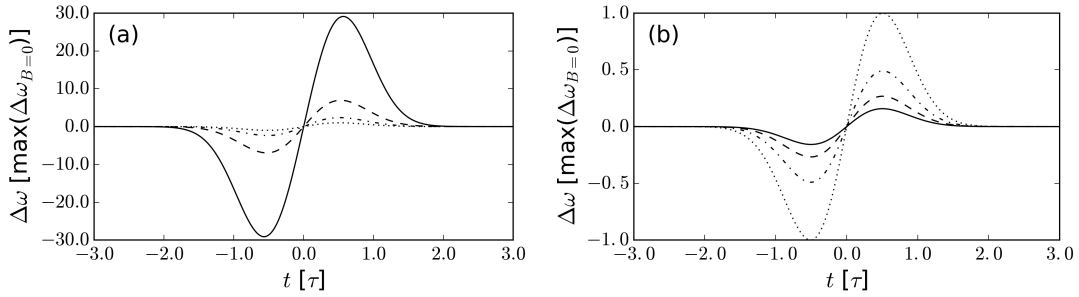

Figure 2.5: Frequency shift introduced by SPM for a Gaussian envelope $a = a_0 \exp(-t^2/\tau^2)$. We show a pulse of amplitude of $a_0 = 0.1$, at an arbitrary distance L into a plasma of density $n = 0.1$. The dotted line plot shows the unmagnetised case. The influence of an external magnetic field causes an increase in frequency spread for the same amplitude and density. The dot-dashed, dashed and solid lines correspond to $B = 0.2$, 0.4 and 0.6, respectively. The y-axis is scaled to the unmagnetised case. (a) RCP. (b) LCP.

This suggests that the longitudinal compression can be significantly enhanced for RCP light with $B < 1$. The magnitude of SPM is tied heavily to the plasma density, with higher density producing stronger modulation.

Pulse compression by SPM alone is not possible for whistler-mode lasers. If we recall that $B = \omega_c/\omega$, and take ω_c to be constant, B will vary inversely with ω. By analysis of (2.3) (or inspection of Figure 2.3a), we can find that $\partial\beta_g/\partial\omega$ takes opposite signs for $B < 1$ and $B > 1$. When this is considered alongside the frequency shift given by (2.13), it can hence be shown that the effect of SPM is reversed when $B > 1$, acting to lengthen the pulse, rather than compress it.

2.3 Numerical simulation results

To illustrate the key features of laser pulse propagation in strongly magnetised plasma predicted by theory discussed above, we have carried out 1D and 3D particle-in-cell (PIC) simulations. All of the following numerical simulations are performed using the PIC code Osiris. In general length scales are characterised by the laser wavelength λ_0 in vacuum and timescales by the laser period $\tau_0 = \lambda_0/c$.

For 3D simulations, we use a Cartesian coordinate system, with a grid resolution set to 20 cells per wavelength in the longitudinal direction, and 5 cells per wavelength in the transverse directions. In order to simulate long propagation distances it is convenient to make use of the moving window feature of Osiris. The laser pulse propagates in the forward z direction. It has a pure sine-squared longitudinal profile with the initial pulse duration of $50\tau_0$ in full-width. The

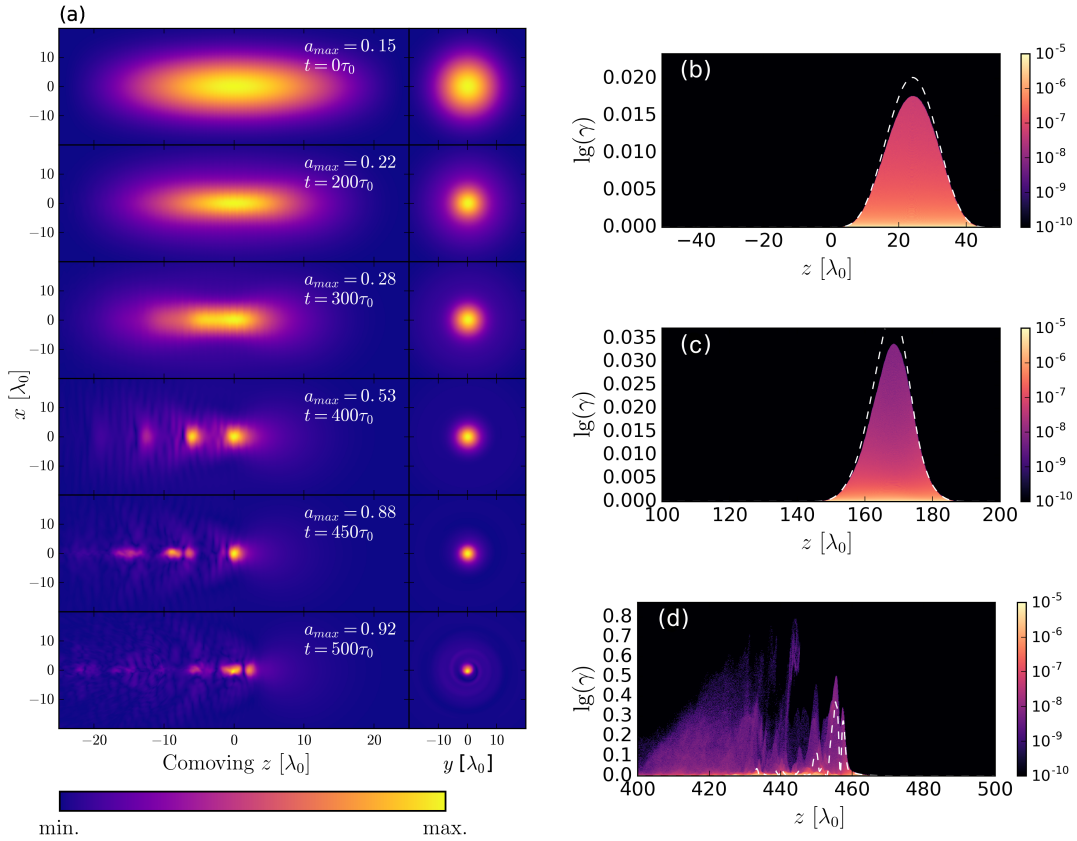

Figure 2.6: Simulation results for a RCP pulse with $B = 0.5$, $P/P_c \approx 2$. (a) Pulse evolution over time. The left column shows the longitudinal amplitude profile, the right column shows the transverse amplitude profile at the longitudinal peak amplitude. Each row is independently normalised, with the colour scale ranging from 0 to the peak amplitude indicated by the value a_{max} on each row. (b - d) The normalised electron distribution at t= $50\tau_0$, $200\tau_0$ and $500\tau_0$, respectively. The dashed line plots denote the prediction by (2.8) using the on-axis pulse amplitude. Focusing and compression are observed over the first few hundred laser periods, until density modulations cause pulse breakup into a train of very short, highly amplified pulses of the plasma wavelength in length. The pulse train undergoes catastrophic collapse and loses cohesion, diffusing rapidly after this. The beginning of this process can be seen at t=$500\tau_0$. This also marks the point at which the electron response ceases to be adiabatic.

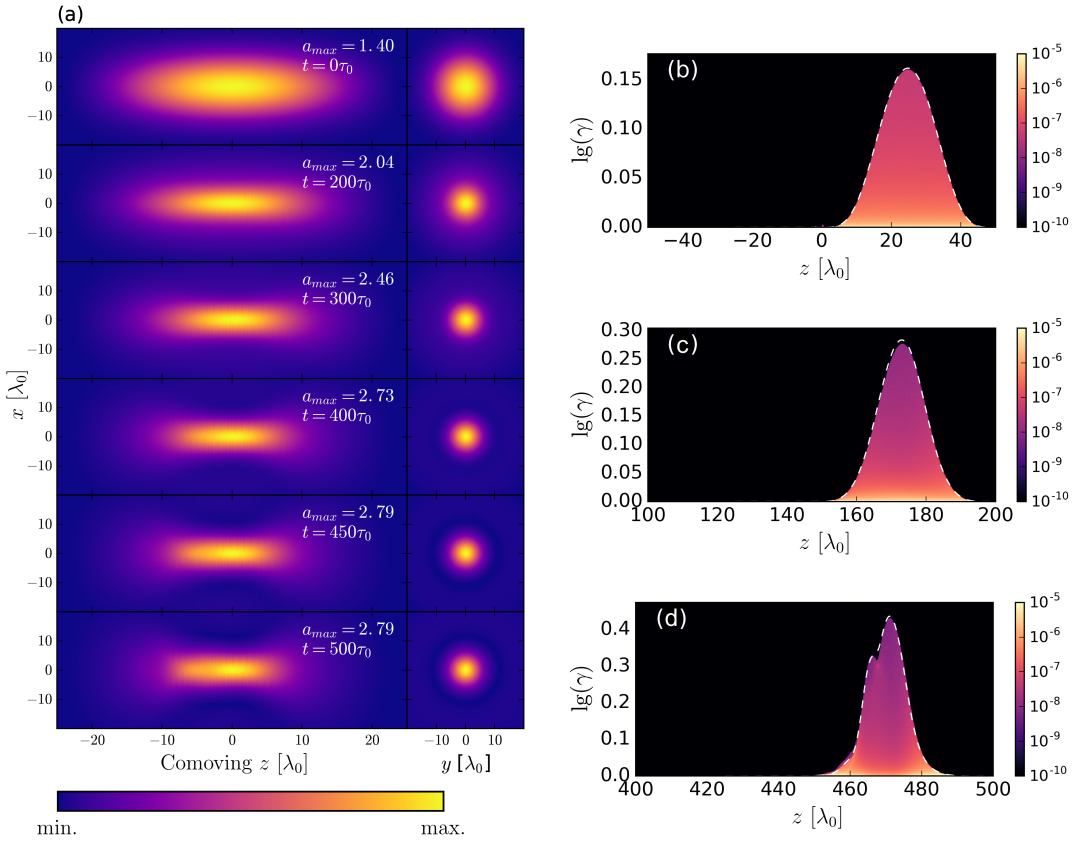

Figure 2.7: Simulation results for a LCP pulse with $B = 0.5$, $P/P_c \approx 2$. (a) Pulse evolution over time. The left column shows the longitudinal amplitude profile, the right column shows the transverse amplitude profile at the longitudinal peak amplitude. Each row is independently normalised, with the colour scale ranging from 0 to the peak amplitude indicated by the value a_{max} on each row. (b - d) The normalised electron distribution at t= $50\tau_0$, $200\tau_0$ and $500\tau_0$ respectively. The dashed line plots denote the prediction by (2.8) using the on-axis pulse amplitude. Smooth focusing and compression occur down to an equilibrium spot size. In the later stages, this pulse begins to be modulated by density fluctiations in a similar manner to the RCP pulse (Figure 2.6).

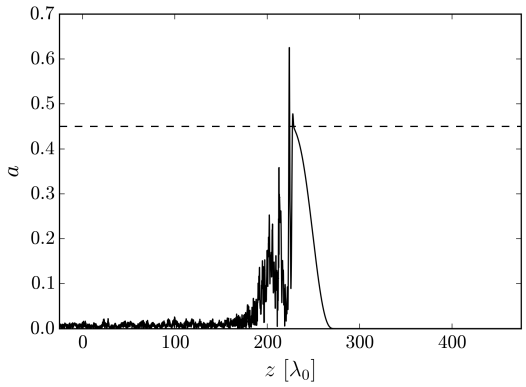

Figure 2.8: A pulse of initial amplitude $a_0 = 0.5$ and length $100\tau_0$ after propagating around $200\lambda_0$ into a plasma with $B = 2$. The dashed line marks the critical amplitude a_c as given by (2.5a). The rear of the pulse is seen to be experiencing absorption by the plasma, while the leading edge is propagating without any absorption.

laser is initialised in vacuum and modelled as a Gaussian beam with a waist size at the focal plane of $R_0 = 10\lambda_0$. The plasma is initially homogeneous after a short ramp of $1\lambda_0$ to minimise boundary reflection and the focal plane is located at the start of the plasma density plateau. Each cell contains 4 electrons, with no initial momenta. Ions are assumed to be immobile, accounting for the fact that the laser pulse duration is short. In 1D, the resolution is increased to 400 cells per wavelength, and 25 particles per cell. Where possible, all other parameters match the 3D simulations.

In terms of normalised peak amplitude, the power of circularly polarised light with a Gaussian transverse profile in the lowest mode is given by $P = 4.29{\times}10^{10}(a_0 R_0/\lambda_0)^2$ [W]. The conditions for self-focusing are met when $P/P_c > 1$ where P_c is given by (2.10).

To test the effect of a magnetic field on the evolution of a RCP laser, we consider a plasma with plateau density $(\omega_p/\omega)^2 = 0.02$, with an external magnetic field of $B = 0.5$ (approximately $5{\times}10^3$ Tesla for $\lambda_0 = 1\mu$m). The predicted self-focusing adjustment is $\eta_0^{-4} = 1/16$ that of the unmagnetised case, corresponding to a peak intensity of approximately $3{\times}10^{16}$ Wcm^{-2} (for $\lambda_0 = 1\mu$m). We use a laser with initial peak amplitude of $a_0 = 0.15$, such that $P/P_c \approx 2$. The results of this simulation are shown in figure 2.6. The pulse propagates at reduced β_g according to Eq. (2.3). Both SF and SPM-driven longitudinal compression are visible, which are coupled to each other. These effects cause a large increase in peak intensity, close to 6 times the initial amplitude. This increase in amplitude causes the excitation of longitudinal electron plasma waves at the wavelength of $2\pi v_g/\omega_p$, which has been reduced as compared to unmagnetised plasma according to figure 2.3(a). The plasma waves further distort the longitudinal profile of

the laser pulse, resulting in the formation of a pulse train similar to that studied by [14, 50]. As the beam waist collapses down further, ponderomotive expulsion becomes significant, with the minimum electron density reaching close to, but not quite zero at the pulse. As expected, the self-generated magnetic field remains comparatively small, reaching only 2% of the imposed longitudinal magnetic field strength.

Figures 2.6(b-d) show that the pulse evolution initially appears to conform to the analytical model derived here. However, after a certain distance the pulse shape is radically altered, complex structures form, and plasma heating begins. From these simulations it is evident that RCP pulse evolution in near resonant plasma is not well described by the model employed here. At an even later time, longitudinal compression of the laser pulse occurs, which allows for the excitation of electron plasma waves [107], an effect which is explicitly ignored in deriving (2.2). The strong spatiotemporal compression also raises the pulse amplitude well beyond the weakly-relativistic regime. Obviously this continuous evolution of RCP pulses in the parameter regime $B \sim 1$ and $P > P_c$ is much beyond our analytical model. The model remains, however, a reasonable method to predict the initial tendencies of the pulse evolution.

An equivalent simulation was performed for LCP light. Laser pulse, plasma and magnetic field parameters remain the same with the exception that the beam intensity is increased to $5{\times}10^{18}$ Wcm^{-2}, to maintain $P/P_c \approx 2$. The results of this simulation are shown in Figure 2.7. Focusing and compressional effects are smooth and the plasma electron response remains adiabatic throughout. The pulse group velocity is seen to be increased, in agreement with Eq. (2.3) and Figure 2.3(a). This can be qualatatively confirmed by inspection of Figures 2.6(d) and 2.7(d). Comparing the propagation distances of both pulses after the same amount of time highlights the difference in group velocity for LCP and RCP light.

It is well documented that plasma electrons gain significant amounts of energy near cyclotron resonance, which finds application in resonance heating systems for magnetically confined fusion reactors [108]. Here we are relatively far from resonance and still observe large amounts of energy absorption to the plasma, with the peak electron Lorentz factor observed to be around 3 times that predicted by the theory. This behaviour is more problematic in the near-resonant whistler regime, as intense light may easily cause a feedback of electrons continually gaining energy, resulting in the plasma returning to a resonant state. The asymmetry in electron response around $B = 1$ is not predicted by the simple model in (2.8) but may be readily observed in simulation.

To demonstrate the critical amplitude as described by (2.5a) we performed a 1D simulation of a whistler pulse, shown in Figure 2.8. For $B = 2$, $a_c = 0.45$ and hence the initial peak

amplitude was set at $a_0 = 0.5$. The pulse was also lengthened to $100\tau_0$ in full-width so as to better demonstrate the process.

As the pulse moves through the plasma, the leading edge produces an adiabatic electron response in agreement with the theory, up until the pulse amplitude $a = a_c$. At this point, the plasma becomes highly absorbing and the rear of the pulse is rapidly absorbed. This leaves an attenuated pulse traveling with a wake of heated plasma behind it. While this is very well represented in 1D, extension to higher dimension introduce transverse effects which alter the propagation characteristics. However, the critical amplitude remains a good estimate of the onset of energy absorption to the plasma.

2.4 Conclusions

The simulation results demonstrate the influence an externally applied magnetic field has on weakly relativistic plasma electron dynamics and laser propagation. In general, LCP light experiences reduced electron motion, and hence a reduction in instability growth in the presence of a strong external magnetic field. Under these conditions, pulse evolution becomes less sensitive to pulse amplitude, and the weakly relativistic approximation remains applicable even at high pulse amplitudes.

In contrast to this, RCP light experiences enhanced electron motion which becomes unpredictable when the electron cyclotron frequency approaches the incident laser frequency $B/\gamma \simeq 1$, due to the effects of cyclotron resonance. As B enters the whistler regime electron motion is once more reduced, and exceptionally strong fields of $B > 2$ experience reduced electron motion compared to the unmagnetised case for both polarisation directions.

Near to cyclotron resonance, electron motion and hence pulse evolution is very sensitive to laser amplitude for RCP light. This puts considerable strain on remaining under the weakly-relativistic approximation. Even a pulse which is initially weakly relativistic can quickly evolve to a point at which it can no longer be considered as such. This introduces complicated nonlinear phenomena, in particular, strong coupling between transverse and longitudinal evolution in the short pulse regime. Transverse focus increases the peak amplitude of the pulse, which in turn enhances longitudinal pulse compression, ponderomotive expulsion of electrons, excitation of electron plasma waves and subsequent electron acceleration. These are beyond the scope of the presented analytical model.

Despite this, the combination of transverse and longitudinal effects on RCP laser pulses may offer new opportunities for the manipulation of high power laser propagation in underdense

plasmas, which may be relevant to applications such as plasma heating, and with extensions to a fully relativistic model provide insights for laser-plasma based particle acceleration and radiation.

Chapter 3

Laser Pulse Compression Towards Collapse and Beyond

The dynamics of three-dimensional (3D) compression of ultrashort intense laser pulses in plasma is investigated theoretically and numerically. Starting from the slowly-varying envelope model, we derive equations describing the spatiotemporal evolution of a short laser pulse towards the singularity, or collapse, based on the variational method. In particular, the laser and plasma conditions leading to spherical compression are obtained. 3D particle-in-cell simulations are carried out to verify these conditions, which also enable one to examine the physical processes both towards and beyond the pulse collapse. Simulations suggest that the laser pulse can be spherically compressed down to a minimum size of the order of the laser wavelength, the so called lambda-cubic regime. The compression process develops more than twice as fast in simulation than what is predicted by the envelope model, due to the simplified nature of the latter. The final result of this process is pulse collapse, which is accompanied with strong plasma density modulation and spectrum broadening. The collapse can occur multiple times during the laser pulse propagation, until a significant part of the pulse energy is dissipated to electron acceleration by the laser ponderomitve force. It is also shown that a strong external DC magnetic field applied along the laser propagation direction can enhance the rate of compression for circularly-polarised laser pulses, when compared to an unmagnetised plasma, allowing access to strong compression and focusing in the low-density and low-amplitude regime.

3.1 Introduction

The ultrashort laser pulse has become a routine tool of high energy-density physics research, but the nature of bandwidth-limited amplification, and the finite damage threshold of solid-state optics, place lower limits on the pulse duration, focal spot size, and thus an upper limit on the peak intensity which can be produced. Plasmas are a natural choice to move beyond these limits, having extremely tunable optical properties and almost no restrictions on the beam intensities which may be sustained within them.

The study of nonlinear optical materials, as a medium to focus and compress already ultrashort laser pulses, has been a subject of considerable research interest in the past decades [5,40,41,54,109–116]. Generally, this can be described by the nonlinear Schrödinger equation for the envelope of the laser pulse under the paraxial approximation [109–111, 117]. This equation predicts that simultaneous self-focusing and compression can lead to collapse of laser pulses, where the laser focal spot size and duration both approach zero, accompanied by explosive growth in the laser intensity. Physically, however, such a limit cannot be achieved since the envelope equation is no longer valid when the laser pulse is approaching collapse. A modified nonlinear Schrödinger equation demonstrates the phenomenon of pulse steepening and spectrum broadening in various optical media [118, 119].

Compared to other nonlinear optical media, plasma can be used to manipulate short laser pulses at high peak power well above tens of terawatts. Under such peak powers, the nonlinear effects are mainly due to the relativistic effect and ponderomotive force. In this case, the envelope evolution of the laser pulses can still be described by a modified nonlinear Schrödinger equation. Typically this equation can be studied analytically [41, 112, 120, 121] or numerically [54, 90]. Through these combined efforts, relativistic self-focusing and self-compression are well understood. However, the two processes have mostly been considered separately, as we do in chapter 2. For ultrashort pulses, these processes often occur simultaneously and therefore, in order to accurately reproduce the problem a coupled treatment is required. An interesting avenue of research is the possibility to focus and compress laser pulses to the so called lambda-cubic regime [122], which may provide the opportunity to produce isolated attosecond pulses and achieve extreme high intensity [123–125]. When approaching this regime, the paraxial envelope equation is no longer valid. More interestingly, laser pulse collapse may develop during its focusing and compression, which is expected to be accompanied by spectrum broadening, plasma heating or particle acceleration and plasma density modulation. These are notoriously difficult to account for in the envelope model. Self-consistent numerical simulation using the PIC method is an effective way to investigate this problem in 3D geometry. PIC simulation

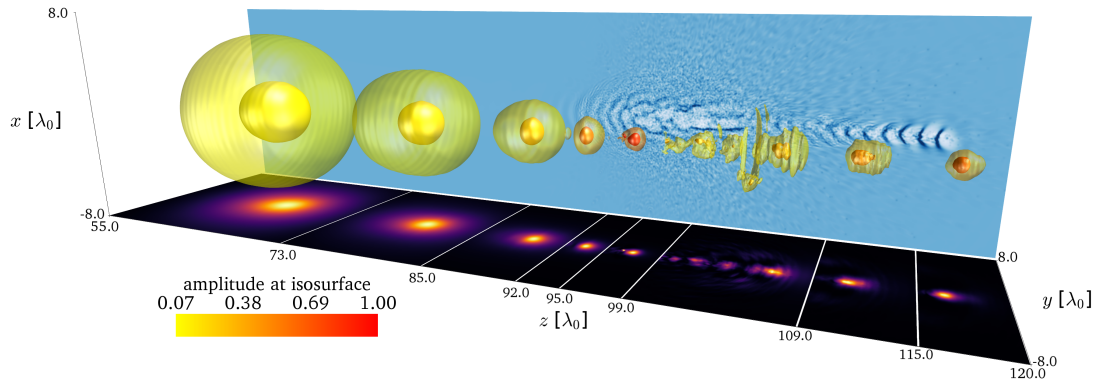

Figure 3.1: Three-dimensional spherical compression of an ultrashort pulse towards collapse and beyond, shown at progressive times, for the parameter setup discussed in section 3.4.1. The isosurfaces correspond to 1/e (transparent) and 2/e (solid) times the peak amplitude of the snapshot, coloured according to the lower-left colourbar. The bottom projection shows intensity slices in the y-z plane at $x = 0$, with different snapshots separated by white lines. The rear plane shows the electron density distribution in the x-z plane at $y = 0$, for the $t = 192\tau_0$ snapshot. We see dramatic compression of the initial pulse towards the lambda-cubic regime at $z \sim 100\lambda_0$, accompanied by a very large increase in intensity, over 150 times the initial value. Further attempts to compress the pulse lead to pulse collapse, distortion and strong ponderomotively-driven electron caviation. Despite this, the pulse remnant re-emerges from the collapse site, continues propagating, and undergoes further collapses (here shown up to the second, at z $120\lambda_0$) until the pulse energy is significantly depleted. The rendered snapshots are captured at $t = 120$, 140, 153, 159, 164, 177, 184 and $192\tau_0$ respectively, shown in order from left to right.

allows one to resolve subwavelength structures of the laser pulse during the collapse, which is critical to understanding this process. A typical picture of this, leading up to and beyond collapse, is shown in figure 3.1.

In this chapter we investigate the process of laser pulse compression in 3D towards the pulse collapse both analytically and numerically. We start with the paraxial model of envelope evolution in 3+1 (three spatial plus one temporal) dimensions. By applying the variational approach to the slowly-varying envelope equation, the conditions are derived both in unmagnetised and magnetised plasmas, under which the rates of transverse and longitudinal evolution is matched and the pulse evolves spherically towards the lambda-cubic regime and finally towards collapse. This model provides guidance for self-consistent 3D PIC simulations, which can reveal various features during the laser pulse evolution towards collapse and beyond.

3.2 Theory Model for Laser Pulse Compression in 3D

We consider a right-circularly polarised (R-mode) laser pulse, and are interested in the evolution of the pulse envelope ψ in time and space, so we again adopt the routinely used slowly-varying envelope approximation [41, 54] with the following nonlinear Schrödinger equation

$$2\mathrm{i}\frac{\partial\psi}{\partial z} + \nabla_\perp^2\psi + \epsilon_1\frac{\partial^2\psi}{\partial\tau^2} + \epsilon_2|\psi|^2\psi = 0, \tag{3.1}$$

where $\nabla_\perp^2$ is the tranverse Laplacian and ϵ_1 and ϵ_2 are constants. We have transformed to comoving time $\tau = t - z/v_g$ and are working with the dimensionless variables $\tilde{r} = rk_p$, $\tilde{z} = zk_p^2/k$ and $\tilde{\tau} = \tau\omega_p$, where k and $k_p = \omega_p/c$ are the laser and plasma wavenumbers respectively, v_g is the laser group velocity and the tildes are henceforth dropped for convenience. Note that the constants $\epsilon_1 = \beta_g^{-2} - 1$ and $\epsilon_2 = (1-\omega_c/\omega)^{-4}/2$, where $\beta_g = v_g/c$ is the normalised laser group velocity, $\omega_c = eB/m_e$ is the plasma electron cyclotron frequency in the case when an external DC magnetic field with strength B is applied along the laser propagation direction and ω is the central laser frequency. The group velocity for R-mode laser light may be derived from the dispersion relation (1.37) and is found to be

$$\beta_g = \left[1 - \frac{\omega_p^2}{\omega^2 - \omega\omega_c}\right]^{1/2}\left[1 + \frac{\omega_c\omega_p^2}{2\omega(\omega-\omega_c)^2}\right]^{-1},$$

which reduces to the usual plasma group velocity when $\omega_c = 0$.

We next apply the variational method [120] to study the evolution of ψ. We choose a Gaussian ansatz for ψ of the form

$$\psi(r,z,\tau) = a\exp\left[-\frac{r^2}{R^2} - \frac{\tau^2}{D^2} + \mathrm{i}\rho r^2 + \mathrm{i}\phi\tau^2\right], \tag{3.2}$$

where R, D, ρ and ϕ describe the beam spot size, duration, radial curvature and longitudinal chirp respectively and are all real functions of z. Here a is the normalized peak amplitude and is a complex function of z, which is related to the laser intensity I (W/cm^2) and wavelength λ_0 (μm) via $I\lambda_0^2 = |a|^2(2.76\times10^{18}$ W/cm^2 μm$^2)$. Assuming evolution from initial conditions a_0, R_0 and D_0, where R_0 is normalised to k_p and D_0 is normalised to ω_p. It is convenient to further normalise all parameter functions to their initial values, e.g. $\tilde{R} = R/R_0$, $\tilde{D} = D/D_0$, $\tilde{a} = a/a_0$, with the tildes dropped henceforth for convenience. The full derivation and results of the variational method are given in appendix B. Of most relevance here are the two coupled

equations describing the transverse and longitudinal evolution of ψ, given by

$$\frac{\mathrm{d}^2 R}{\mathrm{d}z^2} = \frac{4}{R_0^4 R^3}\left[1 - \frac{\mathcal{E}_0 \epsilon_2}{8\sqrt{2} D_0 D}\right], \tag{3.3}$$

$$\frac{\mathrm{d}^2 D}{\mathrm{d}z^2} = \frac{4\epsilon_1^2}{D_0^4 D^3}\left[1 - \frac{\mathcal{E}_0 \epsilon_2 D_0 D}{8\sqrt{2}\epsilon_1 R_0^2 R^2}\right], \tag{3.4}$$

and the constant of motion, i.e., energy conservation equation given by $\mathcal{E}_0 = |a_0|^2 R_0^2 D_0$. In practice, energy is not conserved as we will see, however this equation is approximately correct up until the final stage of compression preceeding collapse. Equations (3.3) and (3.4) describe the evolution of the pulse spot size and duration respectively, and are coupled to each other inextricably. In limiting cases we may simplify this problem. For instance, if we consider the simple case of no external magnetic field, then ϵ_1 depends only on the plasma density and $\epsilon_2 = 0.5$. Under these circumstances we can see immediately that self-compression of the laser is difficult when the plasma is underdense, as $\epsilon_1^2 \ll 1$. This is compounded upon when $D_0 \gg 1$, we see that $\mathrm{d}^2 D/\mathrm{d}z^2 \approx 0$, and may consider changes to R only, resulting in the familiar 2D self-focusing regime. Conversely, if $R_0 \gg D_0 \gg 1$ and the plasma is of sufficient density that $\epsilon_1^2 \sim 1$ then self-compression dominates, and we may consider R to be fixed instead [126, 127].

The picture is more complicated when there is an external magnetic field. Both ϵ_1 and ϵ_2 scale with the magnetic field strength, shown in Figure 3.2. We can therefore see that while ϵ_1^2 remains small for unmagnetised low-density plasma, this is not the case when a strong magnetic field is introduced. In the same vein, ϵ_2 scales very strongly with magnetic field strength. As such, we now have a system in which is more sensetive to relativistic nonlinearlty through ϵ_2, and more suceptable to self-compression specifically through ϵ_1. This combination results in the onset of relativistic effects at lower laser intensity (when compared to the unmagnetised case), and allows for self-compression in low-density regimes in which it is typically prohibited.

In such a sensitive regime, the coupling between (3.3) and (3.4) becomes important. For instance, while a pulse may begin at an amplitude at which self-compression is negligible, the effect of self-focusing may push the amplitude up to the point at which appreciable compression begins to occur, and this in turn will further influence the self-focusing.

A special case of this problem is found when considering spherically symmetric evolution, i.e. when $R(z) \equiv D(z)$. This has been studied previously for spherically symmetric geometry, considering only a single radial dimension [128]. We point out that the result obtained in spherical coordinates is reproducible in cartesian coordinates by applying the initial condition

$$D_0^2 = \epsilon_1 R_0^2. \tag{3.5}$$

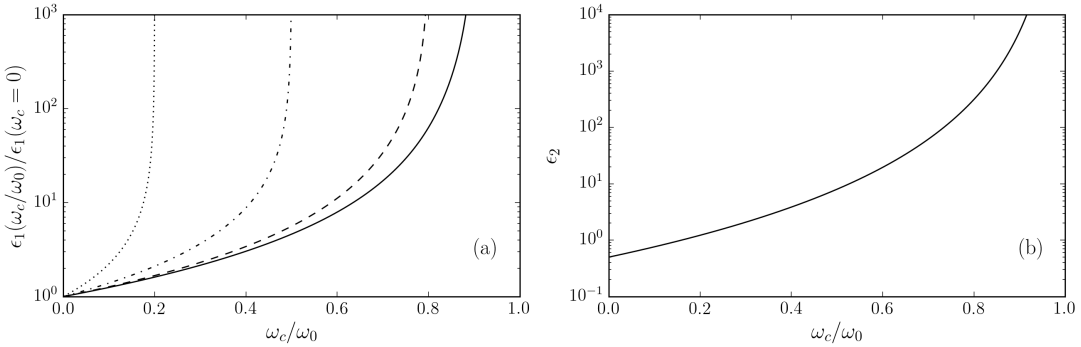

Figure 3.2: Scaling of the two NLSE coefficients with external magnetic field strength. (a) The scaling of ϵ_1 with magnetic field strength as compared to the case of no magnetic field. The scaling is stronger at higher plasma density. The solid, dashed, dot-dashed and dotted lines correspond to $n_e/n_c = 0.1$, 0.2, 0.5 and 0.8 respectively. (b) The scaling of ϵ_2 with magnetic field strength, tending to infinity as $\omega_c/\omega \to 1$.

A subtlety of this condition is that it fixes the relative shape of the pulse for the entire evolution, with the curves $R(z)$ and $D(z)$ only intersecting at the point of singularity. For any pulse aspect ratio other than unity, this implies $R(z)$ and $D(z)$ evolve asymmetrically. While it is convenient to call this the condition for spherical compression, it is not neccesarily spherical in real units. This allows for a situation where, for example, D may reduce to a single wavelength, but R may still be several times larger if the aspect ratio is low.

If reaching the lambda-cubic regime is our goal, it is tempting to suggest we should tune the pulse so that $R(z)$ and $D(z)$ intersect at λ_0. This tuning may be done with ease by inspection of the solutions to (3.3) and (3.4). The result is a small change to either R_0 or D_0 to nudge the point of intersection above zero. In fact, the difference between a pulse satisfying this condition and one satisfying the 'spherical' condition is incredibly small, and the envelope model is simply not powerful enough for such a fine detail to carry over into simulations (let alone experiments) and not be consumed by more dominant competing processes and noise. As such, taking (3.5) as the condition for spherical compression is justified.

To apply this model to more realistic situations, one must remember that the values for D_0 are assumed to be in-plasma, therefore the change in duration due to group velocity reduction should be taken into account as a real pulse enters a plasma. As this happens, a pulse with vacuum duration D_0^{vac} will be shortened to $D_0 = \beta_g D_0^{\text{vac}}$. Now, the adjusted rate-matching conditions are given by

$$D_0^{\text{vac}} = R_0(\beta_g^{-4} - \beta_g^{-2})^{1/2}. \tag{3.6}$$

Allowing both ω_p and ω_c to vary in (3.6) via the group velocity β_g, we can show how the

rate-matching condition changes with both density and magnetic field strength, as illustrated in figure 3.3. In general, lower plasma densities and lower magnetic fields require shorter pulses or broader laser spots in order to compress spherically. Specifically, in an unmagetised underdense plasma with $\omega_p^2 \ll \omega^2$, this requires $D_0^{\text{vac}}/R_0 \ll 1$, i.e., the initial pulse length must be much shorter than the laser transverse spot size. Only when the plasma is of near-critical density, one can realise spherical compression with initial $D_0^{\text{vac}}/R_0 \geq 1$. On the other hand, when a sufficiently high external DC magnetic field is applied, one may still achieve spherical compression with initial $D_0^{\text{vac}}/R_0 \sim 1$, even if the plasma is quite underdense. This implication is applicable to R-mode laser light exclusively. Left-circularly polarised, or linearly polarised light behaves entirely differently when an external magnetic field is imposed. L-mode laser light sees the opposite effect as R-mode, where the required aspect ratio becomes even smaller, and linearly polarised light experiences much more complicated effects, behaving as a superposition of R and L mode light [52]. Equation (3.5) describes the conditions for spherical compression for L-mode and linearly polarised light only when $\omega_c = 0$.

Initial beam tendency may be predicted from (3.3) and (3.4) as critical powers, taking $R(0) = 1$ and $D(0) = 1$,

$$P_R = 2.463 \times 10^{10} \left(1 - \frac{\omega_c}{\omega}\right)^4 \frac{\omega^2}{\omega_p^2} \text{ W} \tag{3.7}$$

$$P_D = 2.463 \times 10^{10} \left(1 - \frac{\omega_c}{\omega}\right)^4 \frac{\omega^2}{\omega_p^2} \frac{\epsilon_1 R_0^2}{c^2 D_0^2} \text{ W}, \tag{3.8}$$

with R_0 and D_0 now in real units. The values of P_R and P_D are derived using the approximate beam power for a CP Gaussian laser $P = 4.298 \times 10^{10} |a_0|^2 R_0^2/\lambda_0^2$ W, where both λ_0 and R_0 are again in real units. Physically, Equations (3.7) and (3.8) give the power thresholds above which the laser pulse will immediately begin to transversely focus or longitudinally compress respectively. These two thresholds are often different, and the initial tendency will not neccesarily be maintained. A laser pulse with power satisfying $P_R < P < P_D$ will initially focus transversely and spread longitudinally, but recall the coupled nature of (3.3) and (3.4); over the course of focusing the peak amplitude may rise enough that it begins to compress, reversing this initial tendency. If (3.5) is satisfied, the two thresholds become identical, and if this threshold is exceeded the pulse will collapse towards the lambda-cubic regime.

3.3 Envelope Model Comparisons

We note that in (3.7) and (3.8), the constant value is a factor of $\sqrt{2}$ higher than the usually cited threshold power for self-focusing of $17.4(\omega^2/\omega_p^2)$ GW [40]. This is due to the variational

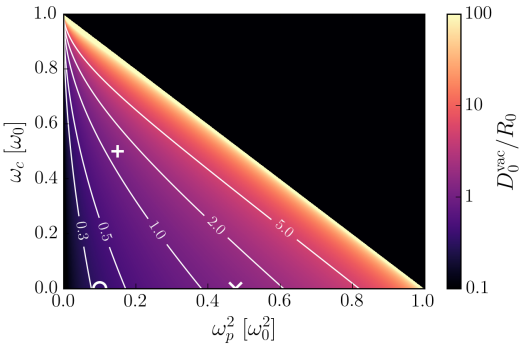

Figure 3.3: Initial pulse aspect ratio required for spherical compression as a function of density and cyclotron frequency. The isobars show the curves for some specific ratios. The upper right black area of the plot is beyond the effective critical density, and hence returns non-real values. The cross, plus, and circle signs denote the conditions we choose to simulate.

method itself. The dimensionality of the problem, and the choice of ansatz used, introduce a constant factor to the second term of the RHS of (3.3) and (3.4). For a Gaussian ansatz and 3 spatial dimensions, such as the case we examine here, this factor is equal to $(3\sqrt{2})^{-1}$. A different ansatz, or a different number of spatial dimensions will change this value. This inconsistency is well documented in reference [128], comparing both Gaussian and sech profiles in up to three spatial dimensions, and is a result of the assumption that the laser profile remains abberationless. This artefact of approximation acts to inflate the calculated power thresholds and stretch the numerical solutions of (3.3) and (3.4) for higher-dimensional systems.

3.4 Results from PIC simulation

Even though (3.6) gives the conditions for 3D compression in plasma, it does not provide details on how it develops. In order to test these equations and show the physical processes involved, simulations are performed using both the 3D PIC code Osiris [77] and supplemented by the cylindrically symmetric, quasi-3D PIC code FBPIC [79], which can produce very similar results to that of cartesian 3D PIC codes for the problems considered here, while at the same time being computationally cost-effective. A more detailed comparison between the two codes is given in appendix C, where we find good agreement between the two for the purposes of this work.

In general, length scales are normalised to the laser wavelength in vacuum λ_0, and time scales to the laser period $\tau_0 = \lambda_0/c$. We note that in the following simulation results, 'time' now refers to elapsed simulation time, rather than the comoving time used in section 3.2. In Osiris, a spatial resolution of $16 \times 16 \times 16$ cells/λ_0^3 is used to ensure the subwavelength structures can be

clearly resolved. The simulation includes electrons and ions, with $m_i/m_e = 1836$ representing a hydrogen plasma. Each cell contains 1 electron and 1 ion, with quartic particle shapes. The laser is right-circularly polarised, initialised from the wall in vacuum a distance of $5\lambda_0$ from the start of the plasma, then traverses a short linear density ramp of length $1\lambda_0$ before entering a cold homogeneous plasma with the plasm plateau beginning at $z = 0$. The simulation box is $200\lambda_0$ in total along z, $50\lambda_0 \times 50\lambda_0$ in transverse extent. In FBPIC, we maintain the resolution of 16×16 cells/λ_0^2 in the z-r plane and simulate two azimuthal modes. We again simulate both electrons and ions use a total of 40 particles per species per cell, distributed as $2 \times 2 \times 10$ per-cell along z, r and θ using cubic particle shapes. Laser amplitude, static magnetic field strength, and plasma density is varied between simulations.

3.4.1 The case for unmagnetised plasma

First, we simulate a non-magnetised plasma with a plateau density of $n_0 = \omega_p^2/\omega^2 = 0.475$ and an initial amplitude of $a_0 = 0.12$, corresponding to $P/P_c \approx 1.2$. The laser focal plane is set to the start of the plasma density plateau, with the beam waist $R_0 = 10\lambda_0$, and vacuum duration $D_0^{\text{vac}} = 13\tau_0$. These conditions are tailored to satisfy the matching condition $D_0^{\text{vac}}/R_0 = 1.3$ as denoted by the cross sign on figure 3.3. Figure 3.4 shows the overview of the pulse duration, amplitude evolution, final electron density and frequency spectrum over the course of the simulation. Firstly, the theory predicts collapse down to a singularity, and this is borne out in the simulation. Shown in figure 3.4(a), the functions R and D evolve at close-to the same rate, which is in good agreement with the theory. However, the overall rate at which the pulse collapses is much faster than predicted by the envelope model given in (3.3) and (3.4), implying both (3.7) and (3.8) are overestimated. We attribute this to artificial threshold inflation due to the 3D nature of the problem, discussed at the end of section 3.2. Accompanying the 3D compression in the simulation, the peak intensity is enhanced by two orders of magnitude. Despite this being a significant increase, it falls short of what a simple analysis might suggest.

If we say that the pulses are compressed to the lambda-cubic (i.e. $R = D = 1$), and there is no energy loss, then the maximum amplification factor we might see is a function only of the initial pulse dimensions, $a/a_0 = \sqrt{R_0^2 D_0}$. This results in a predicted amplification factor of 30 times the amplitude, or 900 times the intensity for the pulse we simulate here. These theoretical predictions are of course, not realistic, as they assume no loss to the plasma, and a perfectly abberationless collapse. Figure 3.6 shows the energy balance over time of an FBPIC simulation with equivalent parameters. We see that after the pulse has entered the plasma, the energy is partitioned between the laser and particles as expected, with little change up the the

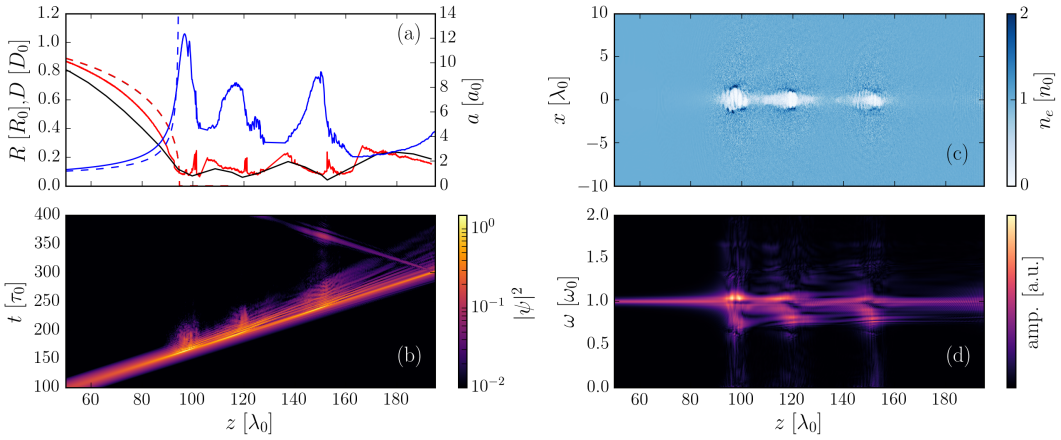

Figure 3.4: Unmagnetised simulation results. (a) Envelope parameter function evolution over the course of the simulation. The relative changes to R (black), D (red) and a (blue) are shown, the dashed lines show the theory-predicted evolution for the same parameters, in which the z axis has been scaled down by a factor of 3.5 in order to overlay with the simulation results. Immediately following a collapse the pulse becomes highly distorted and so meaningful evaluations of its width and duration are difficult to make in these regions. (b) The laser envelope profile along the central z axis at progressive times. Note that a logarithmic scale has been adopted to depict the broad range of intensity variation through the course of laser pulse collapse, and the reversed light tracks in the top-right are caused by boundary reflections as the pulse leaves the simulation box at around $t = 300\tau_0$. (c) Electron density plots at the end of the simulation ($t = 400\tau_0$). (d) Frequency spectra of the on-axis B_x fields performed at fixed longitudinal positions, over the whole simulation time domain ($400\tau_0$).

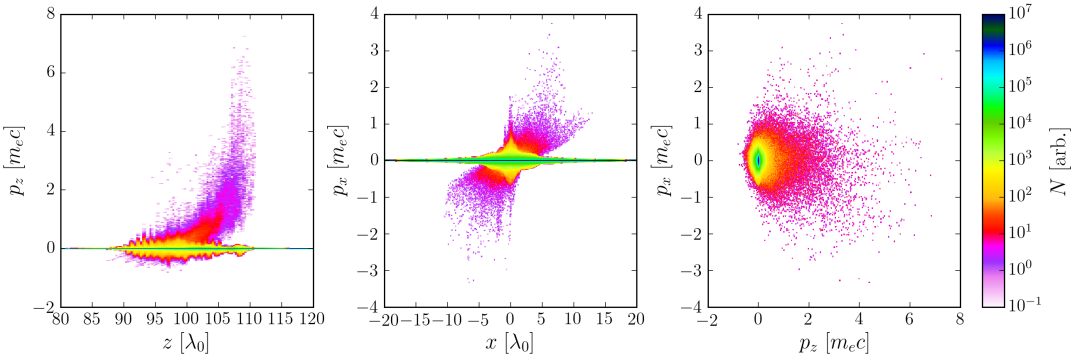

Figure 3.5: Unmagnetised simulation electron phase-space distributions at $t = 180\tau_0$, following the first collapse. (a) The longitudinal momentum p_z versus the longitudinal axis z. (b) The transverse momentum p_x versus the x axis. (c) p_z-p_x distribution.

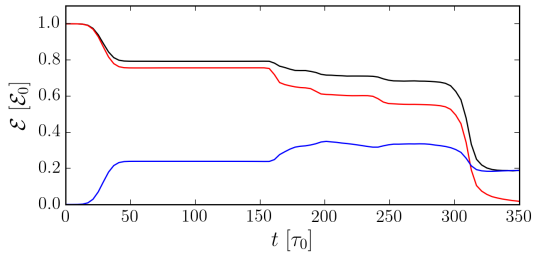

Figure 3.6: Energy balance over the course of the simulation with $n_0 = 0.475$, $B = 0$. The black line shows the total EM energy contained in the simulation ($E^2 + B^2$), the red line shows the total radiative energy calculated from the Poynting vector ($|\boldsymbol{E} \times \boldsymbol{B}|$) via (1.8)-(1.11), and the blue line shows the total kinetic energy of the electrons (ion kinetic energy is negligible). The sharp drop in EM energy at $t \approx 310\tau_0$ corresponds to the laser pulse leaving the simulation box.

point of first collapse at around $t = 160\tau_0$. Despite this, the amplification falls well short of the (naïvely) predicted result. This is due to both the partitioning of energy between the laser and plasma, and the pulse profile deviating from its initial radial profile. While most of the energy initially contained by the pulse remains radiative, as seen by the comparison of red (radiative) and black (total) EM energy curves on figure 3.6, the pulse conforms to a characteristic shape in which significantly more energy is distributed in the wings of the pulse than a Gaussian shape known as the Townes mode [54, 129], thus reducing the potential amplification.

Secondly, successive collapses are found after the first collapse, as the pulse undergoes alternating strong focusing (and compression) and strong diffraction (and decompression), losing energy each time, as seen in figure 3.6 at $t > 160\tau_0$. It is reasonable to extrapolate that this process will continue until there is no longer sufficient energy left in the core of the pulse remnant, at which point it will diffract away rapidly.

Thirdly, the pulse is not reaching a singularity, but a minimum spatial extent of approximately $1\lambda_0^3$ volume (a single cycle pulse, with a spot size of approximately one wavelength). This is due to electron cavitation which acts to prevent further compression. The pulse undergoes collapse three times over the course of the simulation, each time accompanied by a burst of keV to MeV electrons expelled from the cavity in the forward direction, seen in figure 3.5(a). There is a high divergence associated with the burst as illustrated by figure 3.5(b - c) and the particles spread out in a cone from the point of collapse. Ion motion on the other hand is sedentary, with no suprathermal ions produced over the course of the simulation. At the end of the simulation, the ion density distribution is very close to that of the electrons.

The rapid nature of the cavitation causes a density pileup to form in front of the pulse in the few periods leading up to collapse. This scatters the wave, resulting in a sudden, strong

frequency downshift [130, 131], as seen in figure 3.4(d). In addition to frequency downshift, frequency upshift is also found, which is most obvious near the first collapse. This much broadened spectrum also suggests the occurrence of laser pulse compression down to the lambda-cubic regime.

The ponderomotive force becomes quite strong in the lead-up to collapse, causing the formation of an electron density cavity. The downshifted wave becomes trapped in this newly-formed cavity as a soliton, which decays in turn to a post-soliton. Post-soliton formation in plasmas have been examined in both 2D [132,133], and 3D geometry [134] under a variety of conditions. We observe behaviour consistent with previous studies of 3D post-solitons. Formation of the ion density cavity transfers energy from the trapped EM wave to the particles, resulting in rapid decay of the post-soliton over a few tens of laser periods. Ion motion is also critical to the cavity stability. Acting in reaction to the space charge separation, ions are gradually expelled outwards and, as such, the cavities continue to slowly expand long after the postsoliton has completely decayed. Figure 3.4(c) shows the density snapshot at the end of the simulation where the three cavities structures remain well intact.

3.4.2 The case for magnetised plasma

Next, we consider a magnetised case, with normalised magnetic field strength $\omega_c/\omega = 0.5$, plasma density $n_0 = 0.15$ and initial amplitude $a_0 = 0.06$, giving $P/P_c \approx 1.5$. We note that without a magnetic field, this plasma and laser amplitude would have power ratios of $P/P_R \approx 0.09$ and $P/P_D \approx 0.48$. Even accounting for the inflated thresholds, we would expect this pulse to monotonically diffract and spread in an unmagnetised plasma. This case is denoted by the plus sign on figure 3.3 and again calls for an aspect ratio of 1.3 in order to have spherical compression. Results in line with those given for the previous simulation are shown in figures 3.7 and 3.8.

Similar to the case of unmagnetised plasma, the transverse and longitudinal sizes of the laser pulse reduce at the same rate leading to symmetrical collapse as shown in figure 3.7(a), which agrees with our theory. Meanwhile, the pulse compression again develops much faster than that predicted by the theory model given in (3.3) and (3.4). Even with such a low laser energy and in low-density plasma conditions that would typically by unfavourable for compression, pulse evolution towards collapse is found. Again, the pulse undergoes collapse several times, as seen in figure 3.7(b), each time losing small amounts of energy to energetic particle production as seen in figure 3.9. This case also exhibits post-soliton formation, localised at the points of collapse. These are distinguished from those produced in the unmagnetised case by the much

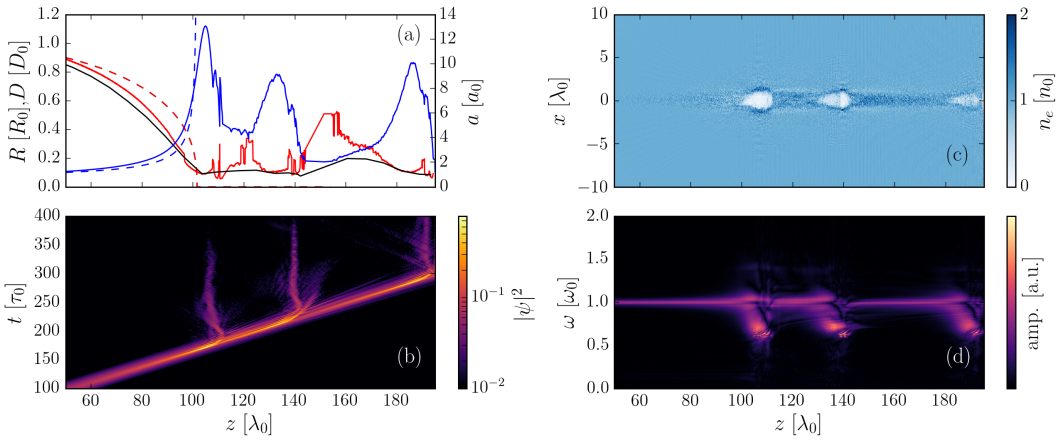

Figure 3.7: Magnetised simulation results. (a) Envelope parameter function evolution over the course of the simulation. The relative changes to R (black), D (red) and a (blue) are shown, the dashed lines show the theory-predicted evolution for the same parameters, in which the z axis has been scaled down by a factor of 2.6 in order to overlay with the simulation results. Immediately following a collapse the pulse becomes highly distorted and so meaningful evaluations of its width and duration are difficult to make in these regions. (b) The laser envelope profile along the central z axis at progressive times. Note that a logarithmic scale has been adopted to depict the broad range of intensity variation through the course of laser pulse collapse. (c) Electron density plots at the end of the simulation ($t = 400\tau_0$). (d) Frequency spectra of the on-axis B_x fields performed at fixed longitudinal positions, over the whole simulation time domain ($400\tau_0$).

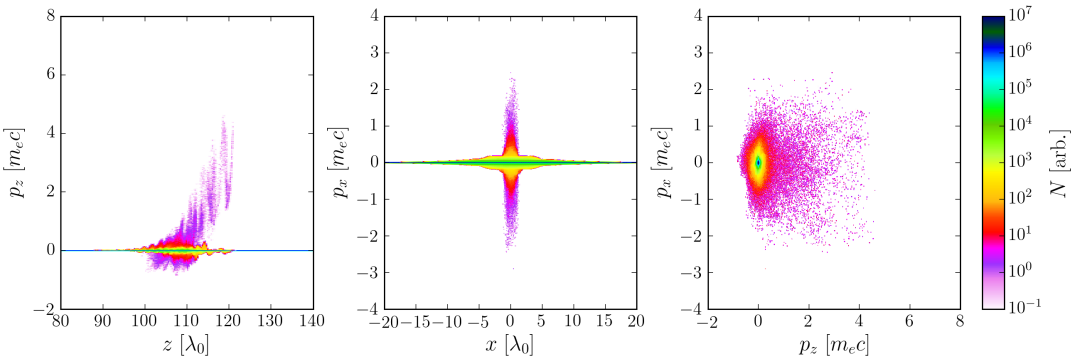

Figure 3.8: Magnetised simulation electron phasespace distributions at $t = 190\tau_0$, following the first collapse. (a) The longitudinal momentum p_z versus the longitudinal axis z. (b) The transverse momentum p_x versus the x axis. (c) p_z-p_x distribution.

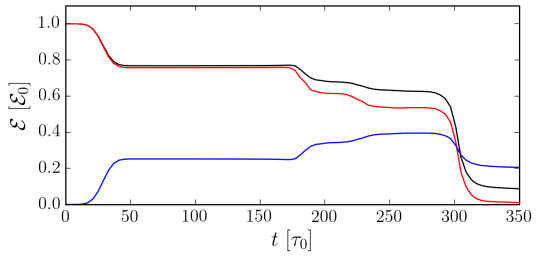

Figure 3.9: Energy balance over the course of the simulation with $n_0 = 0.15$, $B = 0.5$. The black line shows the total EM energy contained in the simulation ($E^2 + B^2$), the red line shows the total radiative energy calculated from the Poynting vector ($|\boldsymbol{E} \times \boldsymbol{B}|$) via (1.8)-(1.11), and the blue line shows the total kinetic energy of the electrons (ion kinetic energy is negligible). The sharp drop in EM energy at $t \approx 300\tau_0$ corresponds to the laser pulse leaving the simulation box.

greater lifespan of the contained solitons. They can be seen as vertical tracks, stationary in space, in figure 3.7(b) and persist many times longer. Research on post-soliton formation in magnetised plasma is less robust than for unmagnetised plasma, [135–137], with studies of 3D magnetised post-solitons doubly so. The mechanism of their comparative longevity and other specific details of magnetised post-solitons are beyond the scope of this work, however the topic certainly warrants futher study.

The frequency spectrum is also quite comparable with figure 3.7(d), showing strong frequency downshift and spectral broadening due to scattering close to collapse and trapping of laser fields inside the cavities.

The production of energetic electrons in this case is similar to the unmagnetised case, which is found only when pulse collapses occur. However from figure 3.8(b) we observe that the electrons are constrained on the central axis by the magnetic field, effectively collimating the particles in the forward direction. The electron density at the end of the simulation is again comparable, with some electron accumulation on the axis, due to the magnetic field constraining electrons. Again we see no energetic ion production, and the final ion density distribution is near-identical to that of the electrons.

The dependence on the magnetic field is very strong, as evidenced by the fact that the rate of compression is comparable to the unmagnetised case at half the laser amplitude, and less than half the plasma density. We point out once more that a laser pulse and plasma of equivalent parameters without such a strong magnetic field would not exhibit any self-focusing or self-compression. The real magnetic field strength required to elicit these effects varies with laser wavelength. For example, the value of $\omega_c/\omega = 0.5$ for $\lambda_0 \approx 1$ μm corresponds to around 5,000 T, which remains a challenge to produce experimentally [86]. However, if we consider

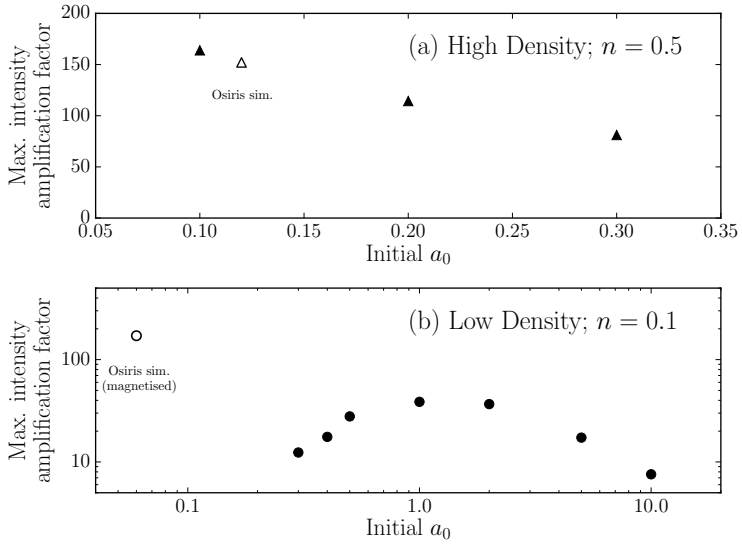

Figure 3.10: Peak intensity amplification for different initial amplitudes and plasma conditions. (a) Shows the high-density results, where $n = 0.5$, and (b) shows the low-density results for $n = 0.1$. The Osiris results discussed in sections 3.4.1 and 3.4.2 are given for comparison, denoted by white markers, and labeled on each subfigure. In all cases, when the maximum intensity for the simulation is reached, the pulse is close to lambda-cubic proportions.

infrared sources, such as CO_2 lasers with $\lambda_0 \approx 10$ μm, this is reduced to 500 T, which is more readily available [8, 138]. Thus this magnetised plasma approach suggests a novel method of compression for long-wavelength or low-amplitude lasers, which are typically more difficult to manipulate [139, 140].

3.4.3 The case for high amplitudes

It is also worthwhile to look at the physics as laser amplitude is raised beyond the weakly-relativistic limit. We choose to examine densities of $n_0 = 0.1$ and $n_0 = 0.5$, represented by the circle and cross on figure 3.3, respectively. By maintaining $R_0 = 10\lambda_0$, from (3.6) this requires $D_0^{\text{vac}} = 3.51$ and 14.14, respectively. We use FBPIC to simulate several different amplitude cases and present the results in figure 3.10. As we are interested only in the envelope dynamics up to the first collapse, we leave ions immobile, as the simulations do not extend to the ion motion timescale. Correspondingly we increase the electron particle count to 100 particles per cell distributed as $2\times2\times25$ in (r, z, θ) and utilise 5 azimuthal modes.

In overview, we may examine the outcome of a compression by the maximum intensity amplification. This is performed for each simulation at the point of collapse and the results are summarised in figure 3.10. In the case of high density shown in figure 3.10(a), we see a general

downward trend as amplitude is increased, with low amplitude pulses in near-critical density plasma capable of significant amplification, over 150 times the initial intensity. This is exhibited by both of the Osiris simulations and the FBPIC simulation with $n_0 = 0.5$, $a_0 = 0.1$. As the amplitude is raised to $a_0 \sim 1$, the high density case sees rapid filamentation and disintegration of the pulse, entirely dominating any other envelope processes and making such conditions unsuitable for compression. As such no results are shown in this regime.

The low density case on the other hand, shown in figure 3.10(b), exhibits a local amplification maximum around $a_0 \sim 1$. The pulses with moderate amplitudes $a_0 = 1$ and $a_0 = 2$ show amplfication of around 40 times the initial intensity. We offer as explanation that in this regime the compression is fast enough that the wake does not have time to modulate the main pulse, and distortions from ponderomotive effects are also at a minimum, resulting in relatively clean compression. As amplitude is further raised, the amplification drops once more, falling monotonically as ponderomotive losses and other destructive processes dominate the propagation. At $a_0 = 10$, the maximum amplification has fallen to less than one order of magnitude. Spherical compression appears to still be possible in this regime, however, due to ponderomotive focusing and leading-edge etching, it is least described by our model.

In all cases, the compressed profile approaches the lambda-cubic regime, with the 'best' results reaching slightly sub-wavelength dimensions, albeit briefly. In general the higher the amplification, the more closely the compressed pulse approaches the lambda-cubic regime.

For a more detailed examination, we may compare two specific cases. A laser with amplitude $a_0 = 0.3$ was simulated for both low, and high density plasma. Both pulses have the same peak amplitude, but due to their differing dimensions, contain different amounts of energy. The pulse in high density plasma contains approximately 4.5 times the energy of the pulse in low density. As such, we expect that the amplifcation factor in high density plasma will be greater than that of the low density plasma, if we are taking the pulses to be spherically symmetric in their respective plasmas. For the long and short pulses we consider the maximum amplification factor calculated from $a/a_0 = \sqrt{R_0^2 D_0}$ comes out to 37 and 19 times the initial amplitude respectively. In fact, the simulation results show amplification factors of 8.6 for the long pulse and 3.4 for the short pulse. This disparity is in line with that discussed in section 3.4.1.

Some snapshots of the simulation results are shown in figures 3.11 and 3.12, showing the laser E_x field, electron density and wavenumber spectra at various times for the $n_0 = 0.1$ and $n_0 = 0.5$ simulations respectively. The low-density case in figure 3.11 shows the initially Gaussian pulse in figure 3.11(a). In figure 3.11(b), after propagating some distance into the plasma, the pulse envelope has contracted both longitudinally and transversely as expected,

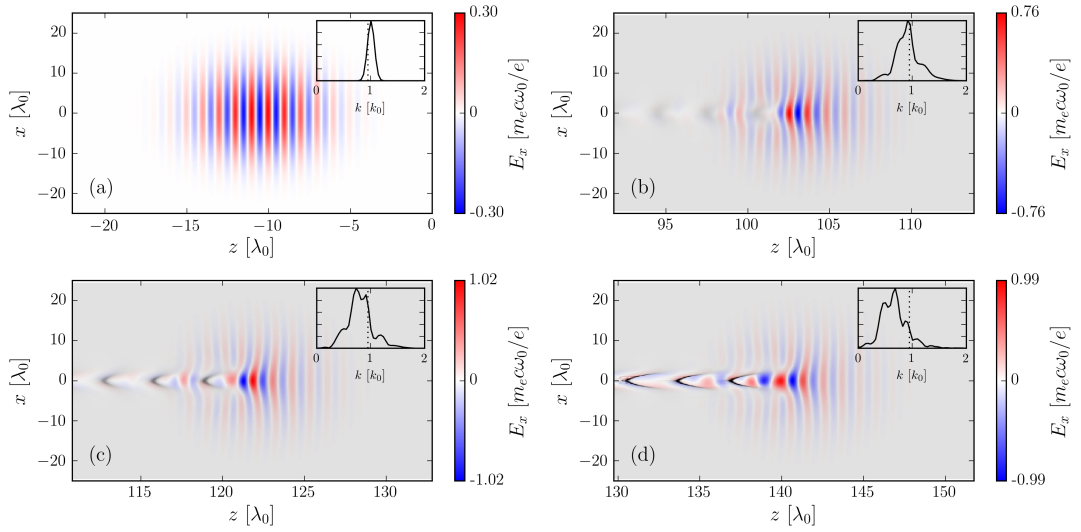

Figure 3.11: Laser electric field (red/blue) and illustrative plasma density (greyscale) at progressive times, for the case of $n_0 = 0.1$, $a_0 = 0.3$. The inset plots show the k-space spectrum of the E_x field along the central axis of each snapshot. The dotted line represents the linear expected value of k based on the plasma refractive index. (a) $t = 0$, the initial pulse profile. (b) $t = 120\tau_0$, the pulse after entering the plasma. (c) $t = 140\tau_0$, the pulse at its minimum extent. (d) $t = 160\tau_0$, the pulse post-collapse.

but it is also modulated by the forming plasma wake. The next snapshot figure 3.11(c) shows the pulse at close-to its minimum spatial extent. We see that although compression is quite symmetric, it is not as strong as it could be, limting to around $2\lambda_0$ in spot-size, and similar longitudinal extent. As propagation continues from figure 3.11(c) to 3.11(d), we see that the frequency downshift continues, and the pulse begins to distort due to the continual downshifting, elongating and trailing in the wake, with frequency components becoming separated [141]. This results in only modest amplification of 10-20 times the initial intensity. In this density regime, spherical compression requires both shorter pulses and higher initial amplitudes than the high-density or magnetised cases. This means lower total energy overall, and renders the compression process open to competition from ponderomotive effects. Compounding this, at close-to-threshold laser powers such as these, the propagation distance before collapse is quite long, giving more time for even low growth-rate instabilities to become significant such as pulse modulation due to scattering processes and pulse spectral changes.

Correspondingly, the high density case is shown in figure 3.12. Again, (a) shows the initial pulse profile, and (b) the pulse after entering the plasma, some reflection is seen as the pulse enters the plasma. Due to the higher plasma density, the time and distance scales for collapse are much shorter than in figure 3.11. After only $30\lambda_0$ the pulse has reached the lamda-cubic

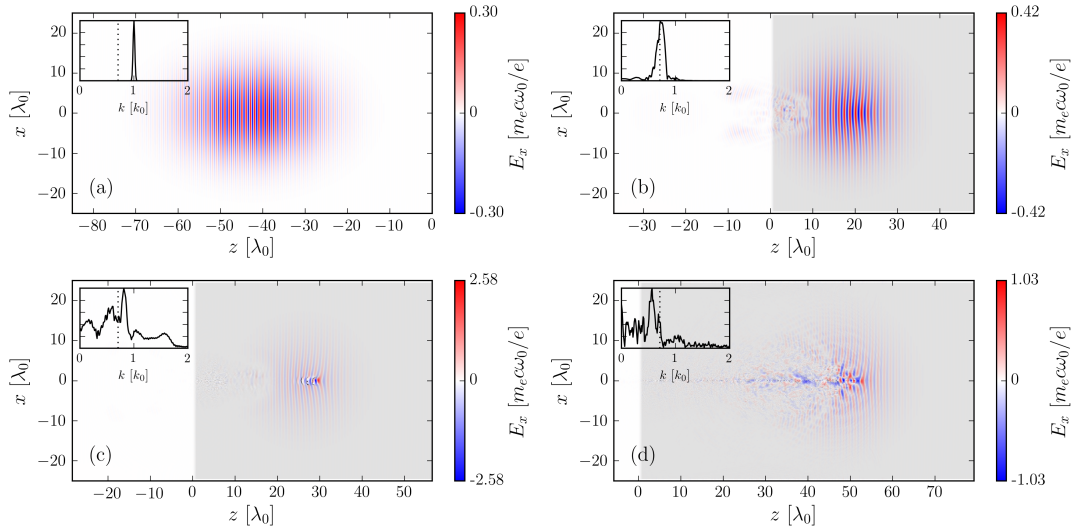

Figure 3.12: Laser electric field (red/blue) and illustrative plasma density (greyscale) at progressive times, for the case of $n_0 = 0.5$, $a_0 = 0.3$. The inset plots show the k-space spectrum of the E_x field along the central axis of each snapshot. The dotted line represents the linear expected value of k based on the plasma refractive index. (a) $t = 0$, the initial pulse profile. (b) $t = 68\tau_0$, the pulse after entering the plasma (c) $t = 80\tau_0$, the pulse at its minimum extent (d) $t = 112\tau_0$, the pulse post-collapse.

regime, with a fitted spot-size of only $0.7\lambda_0$, and an equivalent duration. This naturally induces strong spectral broadening as seen in the inset of (c), however due to the short propagation distance and high plasma density, no appreciable wake has formed to distort the pulse. We attribute the very compact compressed profile to this relatively undisturbed plasma, preserving the $n_e = n_0$ assumption made in the theory. Post-collapse, the pulse disintegrates rapidly, with the remnants continuing to propagate as seen in other simulations.

3.5 Conclusions

In conclusion, we have demonstrated the viability of spherical compression and subsequent pulse collapse for short-pulse lasers over a wide parameter range. 3D numerical simulation suggests the laser pulses can be compressed to the lambda-cubic regime before they reach collapse. Spherical collapse is accompanied by the significant spectrum broadening, the formation of density cavities and the production of energetic electrons in the forward direction. Multiple pulse collapses can be found during the laser pulse propagation until the pulse energy is sufficiently dissipated to plasma. Such phenomena can occur even for short laser pulses with input energy as small as a few millijoules and thus can be demonstrated experimentally on various

laser systems. The inclusion of a magnetic field is shown to enhance the compression rates at lower densities and amplitudes, and could potentially be used to manipulate long-wavelength lasers which are typically difficult to compress below the picosecond scale. While compression can achieve impressive factors of amplification, energy balance analysis shows that only a small fraction of the total EM energy is contained in the core of the pulse. As such the use of a plasma channel may be beneficial to corral the laser energy towards the axis and improve overall efficiency. As laser intensity is increased the compression efficiency falls due to absorption to the plasma, and nonlinear effects causing the pulse evolution to stray further from the expected profile. Eventually, the pulse shape is dominated by ponderomotive focusing and pulse erosion, and cannot truly by called a compression in this sense. The magnetic field affects both the compression rate, and the coupling between transverse and longitudinal focusing, and careful choice of plasma and field parameters may allow pulses of almost any dimension and amplitude to be smoothly compressed using the right matched conditions. While we exclusively consider one specific case, the coupled nature of the evolution equations derived here afford them the potential to govern the shaping of light into nearly any profile, offering an exciting outlook for future research.

Chapter 4

Magnetic Field Amplification by High Power Lasers

The process by which an existing magnetic field of relatively low strength 10^2-10^3 T may be amplified to a quasistatic magnetic field aligned along the laser axis of 10^3-10^4 T is investigated. The mechanism underlying the effect is found to be ponderomotive in nature, governed by grad-B drift currents. Scaling relations for the strength of the induced field are derived from Ampère's law, suggesting roughly linear scaling with light intensity and plasma density. We employ 3D and quasi-3D particle-in-cell simulations to numerically investigate the process, and find agreement with the scaling relations, and support for the ponderomotive mechanism explanation of the effect in general. The lifetime of the process is considered, and we find the major factor limiting its growth and lifetime is ion motion, which disrupts the electron currents neccessary to sustain the induced field. The induced field is found to be of sufficient strength, and is long-lived enough to be relevant for study in relation to applications in radiation production and laboratory astrophysics.

4.1 Introducton

Magnetic fields in plasmas have been a source of constant interest for a considerable amount of time, as they are found universally in all plasma regimes from astrophysicsal to fusion and a need to understand them underpins many of the ongoing problems in plasma physics. They are often ephemeral, and they manifest in many different topologies, making them challenging to study with any degree of generality. This has given rise to many different models and tools with which to study them.

It has been observed previously [142] that an intense LG laser incident on a plasma with a preexisting background magnetic field B_0 may induce an apparent amplification effect, resulting in a highly localised, ultraintense magnetic field along the path of the laser. This effect has been explained as due to the transfer of angular momentum from an LG_{01} mode laser to the plasma, facilitated by the external magnetic field. Instead, we propose that this effect is not unique to OAM or indeed AM-carrying light in general, rather it is a ponderomotively driven effect. The field forms in the wake of the pulse, as particles are ponderomotively expelled from the beam, and their trajectories are then curved by the background field. This kick-starts an amplification of the longitudinal magnetic fields which occurs when a laser is tightly focused. The transverse motion of electrons is converted into an azimuthal current, which in turn induces a self-reinforcing magnetic field, long after the laser has passed.

We propose the use of a linearly polarised pulse in the fundamental mode, providing no angular momentum of its own. However, in the presence of a background magnetic field, we find that the plasma nevertheless gains a significant amount of angular momentum, and a strong, static magnetic field forms in the wake of the pulse. The mechanism underlying this field is not immediately obvious, and so we perform simulations and use the results to discuss potential explanations for the phenomenon.

4.2 Simulation Setup

Simulations were carried out using both Osiris and FBPIC to determine both the basic principle and perform parameter variations in order to better understand the process by which the magnetic field forms and is sustained. The Osiris simulations used a plasma $40\lambda_0 \times 40\lambda_0 \times 30\lambda_0$ with a resolution of $32 \times 32 \times 32$ cells/λ_0^3 and 60 iterations per laser period. A linearly polarised laser with duration $D_0 = 10\tau_0$ and spot size $R_0 = 7\lambda_0$ with a peak amplitude of $a_0 = 5$ incident on a plasma with $n_0 = 0.5$ and a normalised background magnetic field of $B_0 = 0.2$ (such that $\omega_c = 0.2\omega$). A 3D render of the induced field is shown in figure 4.3. The very well defined cylindrical shape is due to the background magnetic field, which restricts particle motion around the axis, but allows for particles to stream along z freely, allowing the field to spread to the edges of the plasma at $z = 5$ and $z = 35$. In order to explore the effects of parameter variations, FBPIC is employed. The FBPIC simulations use a similarly sized plasma to that of the Osiris simulations, but with a lower resolution of 16×16 cells/λ_0^2. Five azimuthal modes are used with $2 \times 2 \times 25$ particles along r, z, θ. We find that there is sufficiently good agreement between Osiris and FBPIC to justify the use of the latter in tandem. The cylindrically symmetric nature

of FBPIC does result in significantly more noise close to the axis, however this is compensated for in the analysis with a slight smoothing filter.

4.3 Mechanism and Scaling

4.3.1 Angular Momentum

As observed by [142], during the formation and maintainence of the induced magnetic field the plasma obtains a vast amount of angular momentum, and this is the mechanism to which they attribute the magnetic field formation. However, the amount of angular momentum imparted to the plasma cannot be accounted for by the laser alone. The total angular momentum of light may be calculated via

$$\boldsymbol{L} = \epsilon_0 \int_V \boldsymbol{r} \times (\boldsymbol{E} \times \boldsymbol{B})\, \mathrm{d}V, \tag{4.1}$$

where $\boldsymbol{r}$ is the position vector and V is the plasma volume. This expression represents the total angular momentum, making no distinction between spin or orbital contributions. Equation (4.1) requires the longitudinal fields be included in order to produce a nonzero result for the AM along the axis, this makes it somewhat more difficult to use in analytically calculating the AM of light. However it is useful for numerically evaluating simulation results. An alternate method of approximating the the total angular momentum of a laser pulse may be to calculated from the number of photons, and then multiply by $\hbar(\delta + l)$ accounting for the SAM, where δ describes the polarisation state, and OAM where l describes the azimuthal index of a laguerre polynomial.

For a pure gaussian laser using the tesbed parameters described in section 4.2, the total energy comes to $\mathcal{E} \approx 1.1$ J. If we simulate a LG_{01} beam with the amplitude scaled such that the pulse contains the same energy, we may use the photon energy $\mathcal{E}_\gamma = hc/\lambda_0$ and take $\lambda_0 = 1\mu$m for simplicity, to find there are $\mathcal{E}/\mathcal{E}_\gamma \approx 5.5 \times 10^{18}$ photons in total. The beam should therefore carry an OAM of 5.8×10^{-16} kg m^2 s^{-1}. This value is confirmed by measuring the total energy, and angular momentum of a simulated LG beam, where we find both in good agreement with theory. This value, assuming angular momentum is conserved, should be the sum of the AM partitioned between the EM fields and the plasma over the course of the simulation. In fact, this is not the case. Figure 4.1 shows the angular momentum and energy partitioning for several laser configurations. Each pulse contains 1.1 J and the CP and LG pulses begin with the calculated value of AM, be it spin or orbital. Small differences can be seen in the coupling to the plasma, mostly due to the small differences in refractive index and focusing dynamics

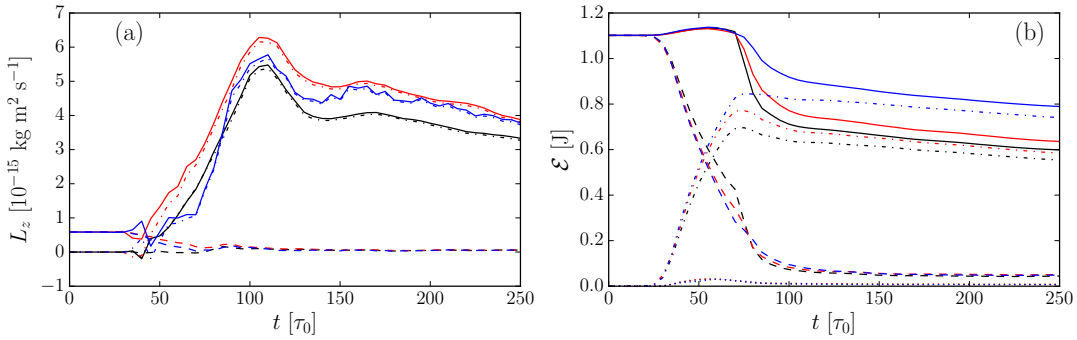

Figure 4.1: Equal-energy laser pulses with different field configurations. Linear polarisation (black), circular polarisation (red) and linearly polarised LG_{01} (blue). (a) The partitioning of angular momentum along z, where the solid, dot-dashed and dashed lines track the total AM, AM carried by the plasma and by AM carried by the light in the simulation box respectively. (b) The energy balance over the course of the simulations. The solid, dot-dashed, dashed and dotted lines represent the total energy, EM energy, particle energy and the energy contained only in the B_z field respectively.

between the different pulses. However, we see in Figure 4.1(a) that in all cases the total angular momentum in the system grows to around ten times the amount carried by the CP and LG pulses. While angular momentum should be conserved, it appears that in this case it is not. The external magnetic field may be the cause of this, as it is not generated self-consistently. There is therefore strong motivation to study this phenomena experimentally. A more detailed discussion of how angular momentum is transfered (or not transfered) to the plasma by OAM-carrying beams may be found in appendix D. The pulse energy is shown in figure 4.1(b), and we see that as expected, much of the pulse energy is coupled to the plasma as heating, and some of it is lost as the pulses exit the simulation box around $t = 100\tau_0$. The EM energy that remains is very small comparatively, with the energy contained in the B_z field on the order of mJ. Despite this, it remains roughly constant and due to the compact nature of the fields, the actual field strength remains very high long after the laser has passed. Furthermore we note that upon reversing the polarity of the seed field, the induced field follows suit. Figure (4.2) shows the results of FBPIC simulations demonstrating this for linearly polarised light, where we see two near-identical plots of the B_z field, with only the sign differing between the two. It is interesting to note that this behaviour is also true for LG light, as noted by [142]. This introduces further difficulties in accepting this process as a transfer of angular momentum, as the final AM of the plasma is unrelated to the initial AM of the incident laser.

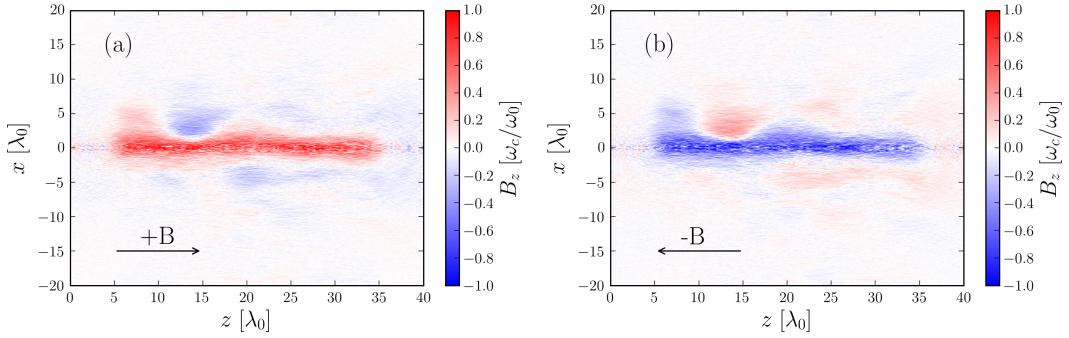

Figure 4.2: Induced magnetic field given a positive (a) and negative (b) seed field along z, indicated on the plots. In both cases the laser is linearly polarised, and incident from the left. Both snapshots taken at $t = 200\tau_0$.

4.3.2 Dynamo Action

Given this, we look for an alternate explanation for the formation and upkeep of the field. The long-lasting nature of the field, and the apparent self-reinforcement it exhibits would suggest some sort of dynamo action as the mehanism for the field, and indeed there has been recent interest in laboratory dynamos [143–145], with solutions found to the MHD equations. We note at this point that MHD is not strictly applicable to laser-plasma interactions, as the spatial and temporal scales are very small, and the plasma is generally collisionless and far from a Maxwellian temperature distribution. For the purposes of the following demonstration however, this may be overlooked.

At a glance, we may look at the magnetic reynolds number R_m, which gives the ratio of magnetic induction to magnetic diffusivity, in order to gauge how readily a plasma might exhibit dynamo action. The minimum R_m for spontaneous amplification of magnetic fields is generally quoted to fall between 100 and 3000 depending on the geometry under consideration [146]. The magnetic reynolds number is given by

$$R_m = \mu_0 \sigma_0 v L \tag{4.2}$$

where L is the length-scale of the plasma flow. In order to estimate R_m we must assume several quantities. While the length scale will neccesarily be very small, on the order of 10^{-6} m, the flow velocity and conductivity can be extremely high for a hot plasma, placing at least some parts of the plasma into the regime in which dynamo action is possible.

Given this, we may look at the MHD magnetic induction equation [147]

$$\frac{\partial \boldsymbol{B}}{\partial t} = \nabla \times (\boldsymbol{v} \times \boldsymbol{B}) + \frac{1}{\sigma_0 \mu_0} \nabla^2 \boldsymbol{B}. \tag{4.3}$$

Where $\boldsymbol{v}$ is the plasma flow velocity, $\sigma_0 = n_e e^2/(m_e \nu_{ei})$ is the DC conductivity of the plasma and ν_{ei} is the electron-ion collision frequency. In reality, the plasma is magnetised, and so the conductivity would be better expressed as a tensor, but again, for the purposes of this example it is not important. The coupling of $\boldsymbol{v} \times \boldsymbol{B}$ allows kinetic energy to be transformed into magnetic energy, and it is evident that without a flow, the equation becomes a magnetic diffusion equation only. This would appear to fit very well with the magnetic fields observed in simulation. However, an answer is not forthcoming. Taking an azimuthal flow $\boldsymbol{v} = \hat{\boldsymbol{e}}_{\boldsymbol{\theta}} v_\theta(r)$ and longitudinal field $\boldsymbol{B} = \hat{\boldsymbol{e}}_{\boldsymbol{z}} B_z(r)$ with radial dependence,

$$\nabla \times (\boldsymbol{v} \times \boldsymbol{B}) = \hat{\boldsymbol{e}}_{\boldsymbol{\theta}} \frac{\partial}{\partial z} v_\theta B_z - \hat{\boldsymbol{e}}_{\boldsymbol{z}} \frac{\partial}{\partial \theta} v_\theta B_z = 0 \tag{4.4}$$

reducing (4.3) to a diffusive process only, at odds with observations. It is important to note that we assume a quasiinfinite plasma length such that $\partial/\partial z \to 0$, and a perfect azimuthal symmetry such that $\partial/\partial\theta \to 0$. In reality the plasma is of finite length, and azimuthal symmetry is certainly not assured, so both terms will be nonzero. However, predicting and describing these asymmetries is not feasable. Clearly this very simplified flow and magnetic field geometry is not sufficient to decribe the origin of the magnetic field, but such a process may still be relevant, relying on asymmetries in the plasma and magnetic field geometry.

4.3.3 Drift Current

Such a strong, well defined magnetic field would imply an equally well defined current sustaining it. However, the instantaneous current density does not show any particularly strong azimuthal component, as seen in figure 4.4(a). However, when the current density is summed along z for the whole simulation box, the azimuthal current becomes quite evident. This lack of a net azimuthal current in the slice diagnostics implies that instead of a direct current, the magnetic field is sustained by a time-averaged current. Therefore, we look at the magnetic field topology itself and consider a drift current arising from guiding-centre motion of the electrons.

The individual and collective motion of charged particles in electric and magnetic fields is fundamental to this work, however generally we have assumed either universally constant or enveloped oscilliatory fields such as the laser fields, and static constant background magnetic fields. Inhomogeneous E and B fields bring with them an entire class of particle motions called

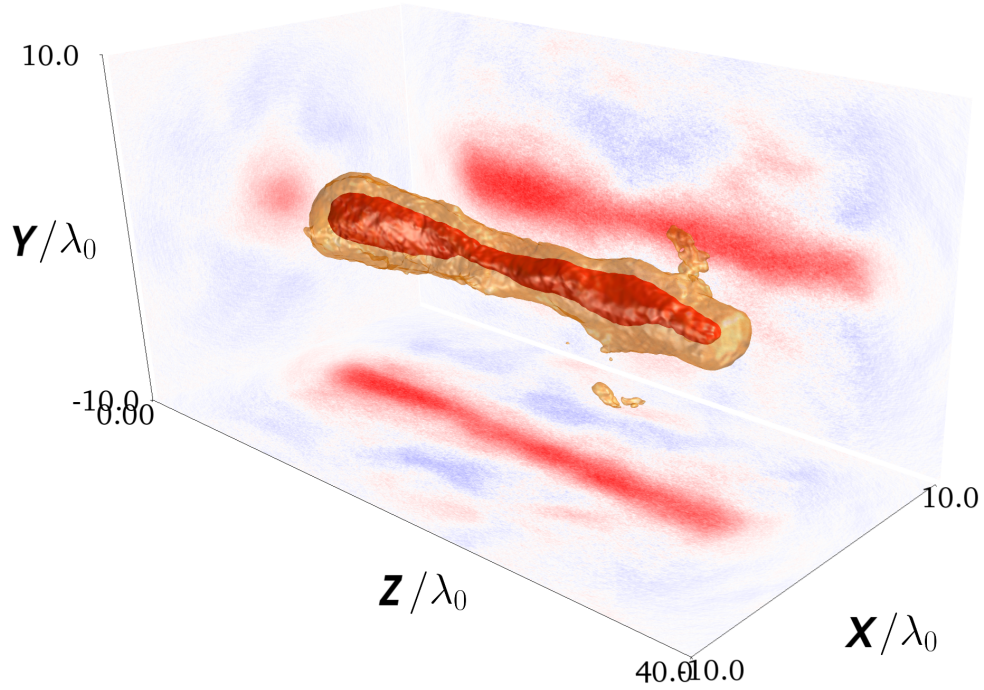

Figure 4.3: The B_z field at $t = 150\tau_0$. Axis labels are given in laser wavelengths. The yellow isosurface corresponds to $B_z = 0.2$, the red isosurface to $B_z = 0.5$. The peak field amplitude in the snapshot is $B_z = 1.02$, corresponding to over 10^4T for $\lambda_0 = 1\mu$m.

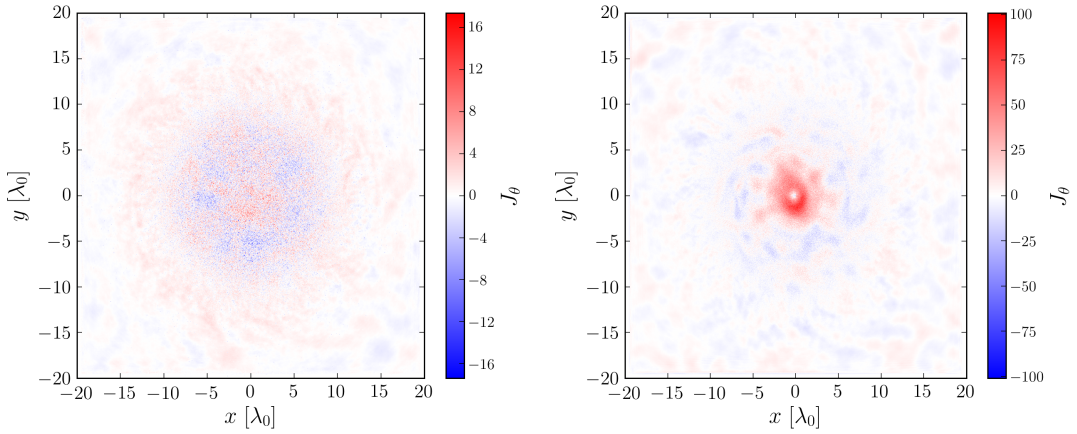

Figure 4.4: Azimuthal current density, at (a) a single slice through the middle of the simulation box (b) integrated along z. In the unintegrated slices, away from the axis there are more clearly identifiable azimuthal currents, as seen in (a). This is due to the lower electron temperature and less turbulent nature of the plasma far from the axis, the currents are transient in nature and when integrated along z there is little net current anywhere except the axis, as seen in (b).

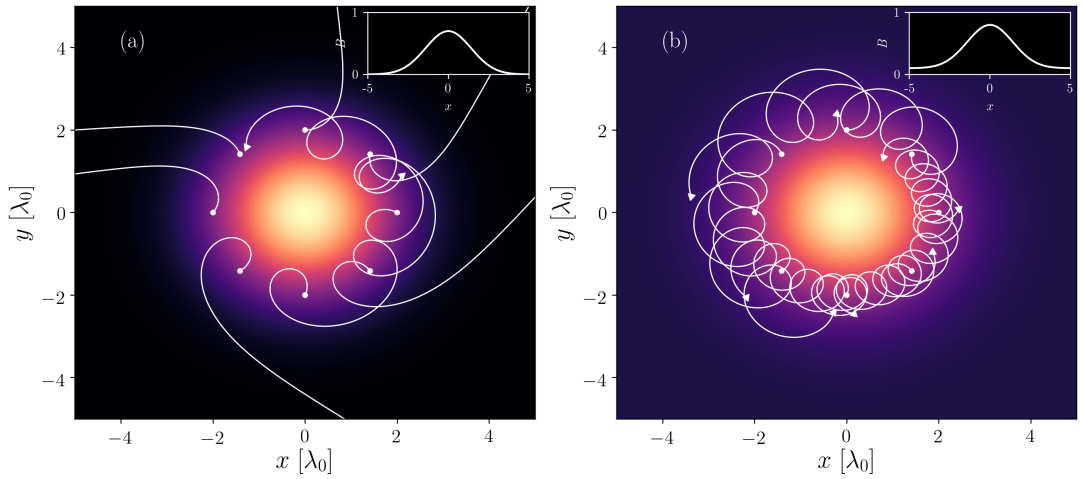

Figure 4.5: The motion resulting from electrons with randomised initial momentum under an inhomogeneous magnetic field. The field is shown by the colourmaps and a slice (inset). Electron orbits are shown without (a) and with (b) a background magnetic field. Note that the difference in magnetic field is very slight between (a) and (b), Inset (b) shows the presence of a background field $B_0 = 0.1$ not present in (a).

drifts. In a plasma with a background magnetic field, the particles will perform cyclotron motion as discussed in chapter 1. Taking there to be no change in the kinetic energy of the particle (i.e. $\boldsymbol{E} = 0$), and taking there to be some spatial gradient to $\boldsymbol{B}$ the guiding centre of the particle motion will drift perpendicular to the gradient of the magnetic field $\boldsymbol{v}_{\text{drift}} \perp \nabla B$. This is the so-called grad-B drift, and in the nonrelativistic limit it is is given by [148]

$$\boldsymbol{v}_{\nabla B} = \frac{\mathcal{E}_\perp}{qB} \frac{\boldsymbol{B} \times \nabla B}{B^2}, \tag{4.5}$$

where $\mathcal{E}_\perp$ is the transverse (relative to $\boldsymbol{B}$) component of the electron kinetic energy. A corresponding drift current density may be estimated by considering the plasma density. If we consider a magnetic field $\boldsymbol{B} = \hat{\boldsymbol{e}}_{\boldsymbol{z}} B(r)$ aligned along z with some spatial inhomogeneity along r, the resulting drift motion $\boldsymbol{v}_{\nabla B} = \hat{\boldsymbol{e}}_{\boldsymbol{\theta}} v_{\nabla B}$. This drift motion is demonstrated in figure 4.5. In figure 4.5(a), some test particles with random initial momenta were simulated and the equation of motion solved numerically. These particles gyrate due to the imposed magnetic field, and drift azimuthally due to the inhomogeneity. When only self-generated fields are considered, even if a centralised, gaussian-like longitudinal field structure forms, while some particles with congruous trajectories will become trapped, most particles will eventually escape, and a self-sustaining field structure cannot form. This is demonstrated in the fact that of the eight particles simulated, six were eventually lost. However, if a background field is imposed as in

figure 4.5(b), all eight particles remain trapped, and continue to contribute to the azimuthal drift current. The exact difference in the magnetic field topology in each case is shown in the inset plots in figure 4.5, the difference is quite minor, but even the presence of a small seed field dramatically alters the particle trajectories. Once a magnetic field is established, the resulting motion of the electrons can be separated into fast and slow components. The slow motion makes up the time-averaged drift current, and the fast motion is the cyclotron motion of the electrons, which act as microscopic current loops, to which we may assign a magnetic moment

$$\boldsymbol{\mu}_e = -\mu_e \hat{\boldsymbol{e}}_{\boldsymbol{z}}, \tag{4.6a}$$

$$\mu_e = \frac{\mathcal{E}_\perp}{B}. \tag{4.6b}$$

This motion is transformed back into a longitudinal magnetic field via Ampère's law, with the drift motion acting to reinforce the seed field, and the cyclotron motion acting to reduce it, although the two competing generated fields are obviously not in balance, given the growth of the magnetic field in one direction. This behavious is borne out in PIC simulation, a random sample of 250 electron trajectories is plotted in figure 4.6, in which the guiding centre motion can be clearly seen in almost all particles near to the laser axis. Quantifying this effect is quite difficult.

Assuming quasineutrality and neglecting ion motion, we may use Ampère's law (1.39b) to study the magnetic field including both drift motion and cyclotron motion

$$\nabla \times \boldsymbol{B} = \mu_0 \nabla \times \boldsymbol{M}_{\omega_c} + \mu_0 \boldsymbol{J}_{\nabla B} \tag{4.7}$$

where $\boldsymbol{M}_{\omega_c}$ is the plasma magnetisation due to the cyclotron motion of the electrons and $\boldsymbol{J}_{\nabla B}$ is the drift current. The magnetisation and drift current are given by

$$\boldsymbol{M}_{\omega_c} = \int_{\boldsymbol{v}} \boldsymbol{\mu}_e f_e(\boldsymbol{v}) \, \mathrm{d}^3\boldsymbol{v}, \tag{4.8a}$$

$$\boldsymbol{J}_{\nabla B} = -e \int_{\boldsymbol{v}} \boldsymbol{v}_{\nabla B} f_e(\boldsymbol{v}) \, \mathrm{d}^3\boldsymbol{v}, \tag{4.8b}$$

where $f_e(\boldsymbol{v})$ is the distribution function of the electrons. If we assume that the distribution $f_e(\boldsymbol{v})$ is Maxwellian, the integral

$$\int_{\boldsymbol{v}} \mathcal{E}_\perp f_e \, \mathrm{d}^3\boldsymbol{v} = n_e k_B T_e = p, \tag{4.9}$$

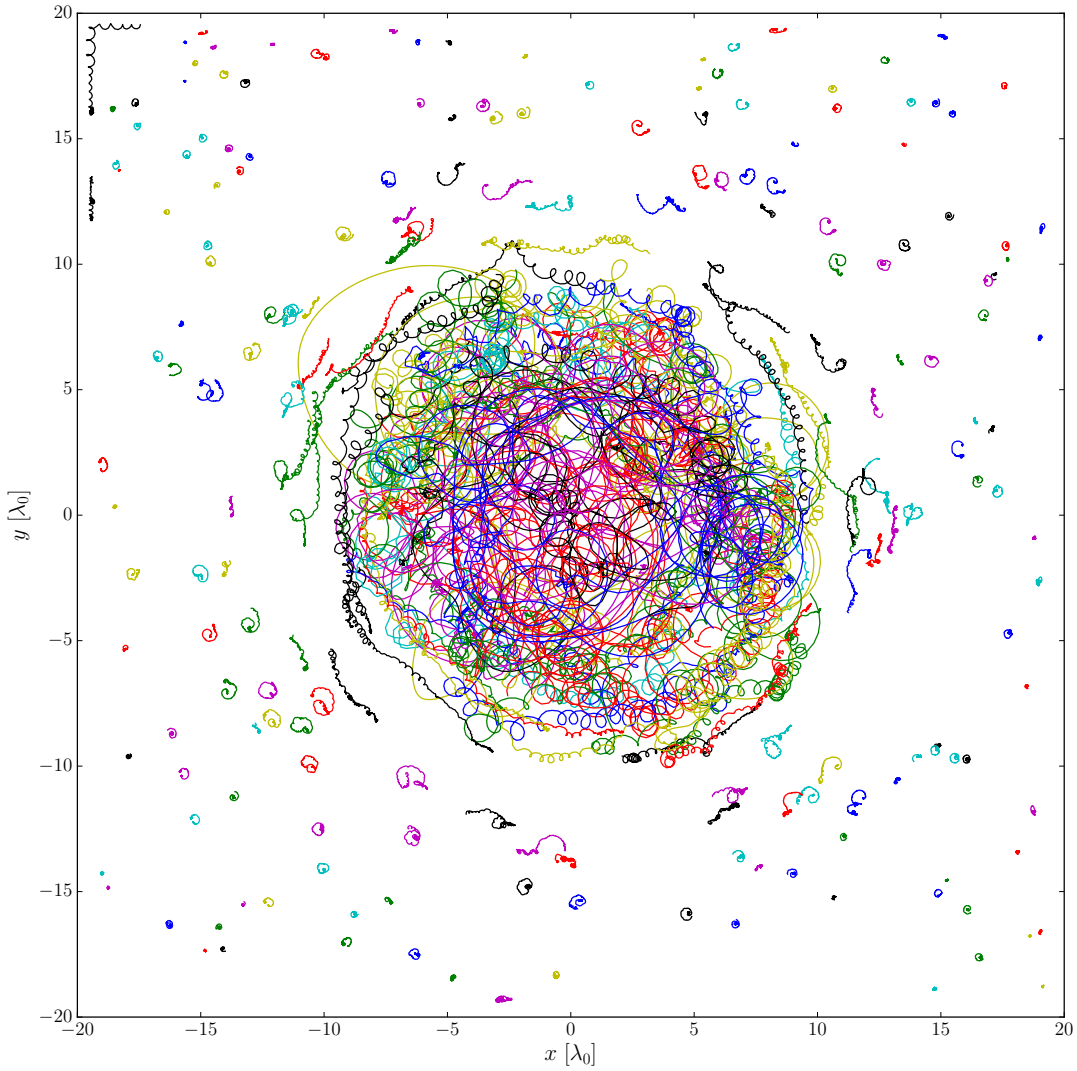

Figure 4.6: A flat random sample of 250 electron orbits. Particle tracks are coloured arbitrarily to improve visibility.

where p is the kinetic pressure, is of use. While it is unlikely that the distribution is Maxwellian when the laser is present, we would expect the plasma to relax towards it once the laser has passed. Using this, we may evaluate (4.7) as

$$\nabla \times \boldsymbol{B} = -\mu_0 \nabla \times \left(\frac{p}{B} \hat{\boldsymbol{e}}_{\boldsymbol{z}} \right) + \mu_0 \frac{p}{B^3} \boldsymbol{B} \times \nabla B \tag{4.10}$$

Here the first term on the RHS denotes the contribution by the electron cyclotron motion, and the second term denotes the contribution by the drift motion. Further algebra on (4.10) leads to the familiar relation

$$\frac{B^2}{2\mu_0} + p = \text{constant}. \tag{4.11}$$

describing the relationship between kinetic ($n_e k_B T_e$) and magnetic ($B^2/2\mu_0$) pressure. Alternatively, we may also arrive at

$$B = \sqrt{2\mu_0 n_e k_B T_e + \text{constant}.}, \tag{4.12}$$

indicating a potential scaling relationship for the magnetic field strength involving the plasma density and temperature.

4.4 Simulation Results and Discussion

Figure 4.7 shows a summary of parameter scans varying several key parameters and examining the effect on the resulting magnetic fields. The results are presented as lineouts averaged in space, taken from the final step of the simulations at $t = 250\tau_0$. The spatial averaging is performed in both z and θ and is achieved by taking advantage of FBPIC's harmonic decomposition algorithm. All field outputs in FBPIC are decomposed according to azimuthal mode, such that a simulation with n_m modes will produce field diagnostics with $2n_m - 1$ components, which may be combined to retrieve the complete field F as follows

$$F = f_{\Re}^0 + \sum_{n=1}^{n_m - 1} \left[f_{\Re}^n \cos(n\theta) + f_{\Im}^n \sin(n\theta) \right], \tag{4.13}$$

where the f coefficients describe the various modes of the field, and θ gives the plane angle at which we are resolving the field. Therefore, to average a field around θ we can see by inspection of (4.13) that the result will be

$$\langle F \rangle_\theta = \frac{1}{2\pi} \int_0^{2\pi} F \, \mathrm{d}\theta = f_{\Re}^0, \tag{4.14}$$

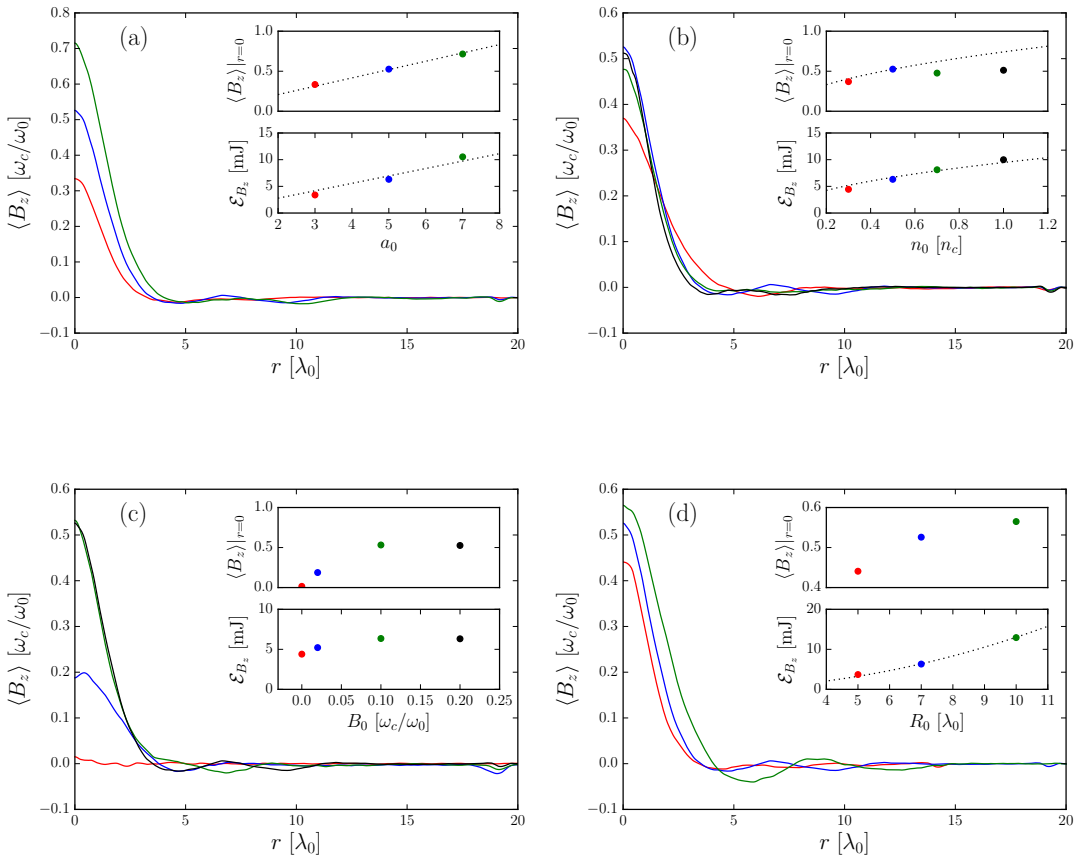

Figure 4.7: Radial magnetic field profiles demonstrating the effect of varying (a) laser amplitude, (b) plasma density (c) seed magnetic field strength and (d) laser spot size on B_z. All simulations use a common testbed with $B_0 = 0.2$, $a_0 = 5$, $R_0 = 7\lambda_0$, $n_0 = 0.5n_c$, snapshots are taken at $t = 250\tau_0$ and spatially averaged around θ and along z. The averaged lineouts are smoothed with a Savitzky-Golay filter with a window length of 15 and polynomial of order 2. The upper insets show the peak magnetic field against the parameter being varied. The lower insets show the total energy contained in the B_z field. Both insets in (a) are fitted to a linear regression, both insets in (b) are fitted to a regression of power half. The lower inset in (d) is fitted to a quadratic regression.

as integrating sinusoids over an integer number of their periods comes to zero. The spatial averaging along z is performed numerically, from the beginning of the plasma to the end of the plasma, such that vacuum fields are excluded.

We may also sum the total energy in the field using the same properties. The field energy density U is given by

$$U = \frac{\alpha F^2}{2}, \tag{4.15}$$

where $\alpha = \mu_0^{-1}$ if F is a magnetic field, and $\alpha = \epsilon_0$ if F is an electric field. We may combine (4.13) and (4.15), and evaluate the volume integral $\int_V U \, \mathrm{d}V$, where $\mathrm{d}V = r\mathrm{d}r\mathrm{d}\theta\mathrm{d}z$, to retrieve the total energy in the field. Desepite the potentially very large number of terms obtained when expanding F^2, most sum to zero when integrated around θ, and so we may analytically evaluate the azimuthal part of the integral, leaving us with

$$\mathcal{E}_F = \frac{\alpha\pi}{2} \int_0^\infty r \int_{-\infty}^\infty 2(f_\Re^0)^2 + \sum_{n=1}^{n_m-1} \left[(f_\Re^n)^2 + (f_\Im^n)^2\right] \mathrm{d}z\mathrm{d}r. \tag{4.16}$$

Which may then be discretised according to the simulation mesh spacing and the remainder of the integral evaluated numerically.

Plasma temperature is related to the laser intensity, therefore we may expect a linear relationship with laser amplitude, as $T_e = \bar{\mathcal{E}}$ and $\mathcal{E}_\perp \propto I \propto a^2$, assuming tranverse motion dominates. This relationship is supported by 4.7(a), where the dotted line in the upper inset shows a good fit to a linear regression. The lower inset shows the total energy of the B_z field, and this also scales linearly with amplitude.

Initial density is more directly controlable, but also affects the energy coupling to the plasma, and the resulting electron temperature. This scaling is tested with the results shown in figure 4.7(b). The averaged field amplitude does not scale this way, instead appearing to saturate after $n_0 = 0.5$, as illustrated in figure 4.7(b) lower inset. This is likely a diminishing return on the energy coupling per particle for a constant laser intensity. Despite this, the total energy contained in the magnetic fields does increase with density, as illustrated in figure 4.7(b) lower inset. This may indicate that a high density plasma with $n_0 \geq 1$ is capable of supporting very high magnetic fields, but with the requirement that the input pulse is of sufficiently high amplitude to heat the plasma sufficiently to drive the requisite currents.

The background field strength is more difficult to quantitatively examine, but nevertheless affects the induced field. The transverse heat flow is dependent on the magnetic field. A higher field restricts electron motion, leading to a sharper, tighter profile. Figure 4.7(c) shows the effect of varying B_0. Naturally when there is no initial magnetic field, no field is induced.

However it is interesting to note from the lower inset that the energy contained in the B_z field is not much less than the cases where an induced field is present. This suggests that the process does not greatly alter the magnetic energy partitioning, rather is simply reorders it to be more collimated. Further, the initial field has a saturation point around $B_0 = 0.1$ beyond which it no longer affects the induced field as seen in the upper inset. This may be explained as the point at which the majority of electrons become trapped close to the axis and contribute to the current. Beyond this, there is no further advantage to increasing the background field. This saturation point will increase linearly with laser amplitude as $p_\perp \propto a$, however the exact value is difficult to determine exactly, relying on an accurate method to predict the resudial momentum of the electrons after the laser has passed. This requires a knowlege of the specific focusing dynamics.

Increasing the laser spot size increases the width of the magnetic field as one might expect, demonstrated in figure 4.7(d). This is in line with the increased energy imparted to the plasma, as $\mathcal{E} \propto R_0^2$, so do we also see a quadratic scaling of the magnetic field energy in the lower inset. The peak field strength however is not affected much, instead seeming to saturate, with the additional magnetic energy contained in the wider field profile. Very large spot-size beams are more prone to fillamentation, so the beam does not focus onto the axis as cleanly as the smaller spot-size beams, As the simulated plasma is quite shallow and the beam itself already ultrashort, self correction and channel formation does not have time to occur the laser energy is deposited over a large radius. This may also help explain why despite the increased energy imparted, the peak magnetic field does not increase as the beam cannnot focus strongly enough to increase the amplitude on-axis much beyond the smaller spot-size simulations.

The induced field forms quickly in the wake of the laser pulse, and appears to have an extremely long lifetime under all circumstances. In all cases the field presists until the simulation ends with very little change in topology, and only a minor decay in field strength. As the local plasma temperature can reach several hundred keV the collision frequency is expected to be negligible, as such, collisions were not simulated. The electron-ion collision rate can be approximated by [149]

$$\nu_{ei} \approx 2.91 \times 10^{-6} Z n_e T_e^{-3/2} \ln(\Lambda), \tag{4.17}$$

where n_e is given in cm^{-3}, Z is the number of free electrons per atom, T_e is the electron temperature in eV, $\ln(\Lambda) = \ln(9N_D/Z)$ is the coulomb logarithm, $N_D = 4\pi\lambda_D^3/3$ is the debye number and $\lambda_D = (\epsilon_0 T_e/n_e e)^{1/2}$ is the debye length. A cursory estimate of the electron-ion collision frequency using the simulation plasma parameters, and taking an electron temperature of 100 keV gives $\nu_{ei} \sim 10^9\ \mathrm{s}^{-1}$, corresponding to an expected timescale for the induced field on the order of nanoseconds, before collisions become significant. It would be beneficial to study

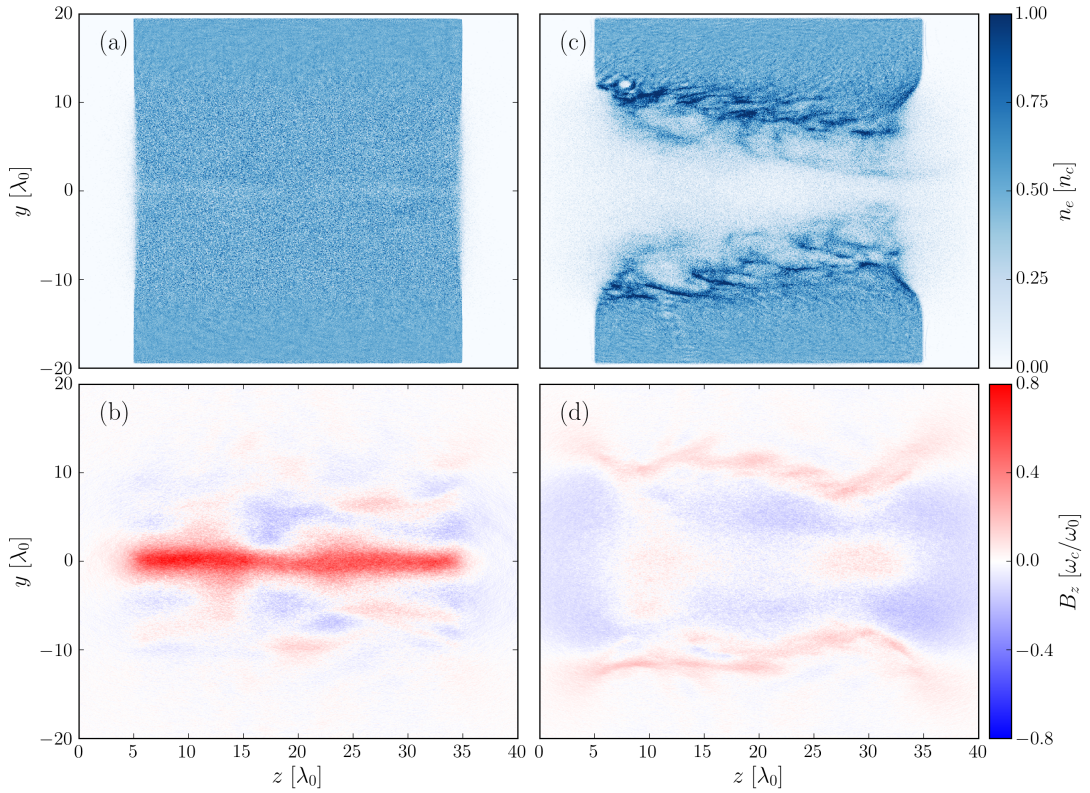

Figure 4.8: Comparison of electron densities (upper row) and B_z field amplitudes (lower row) at $t = 200\tau_0$ in simulations without (a)-(b) and with (c)-(d) ion motion enabled.

the effect collisions have on the energy transport, and determine quantitatively if there are significant losses to this mechanism.

Despite the very high estimation of the field lifetime based on the collision frequency, ion motion substantially alters the magnetic field topology. Figure 4.8 shows the effect of ion motion on otherwise identical simulations. With mobile ions, much of the areas close to the axis are evacuated shortly after the laser passes. As electrons move to neutralise the charge separation induced by the radial motion of the ions, this in turn disrupts the azimuthal current and leads to a rapid disappation of the magnetic field. The induced field in this case is less collimated, with the on-axis strength much lower. However, there is still a relatively ordered field formed due to the fairly well-defined wall of the evacuated channel. As the channel expands, the radial motion of the plasma as a whole induces a complex expanding multiringed magnetic field structure, which may well be worthy of study in its own right. For experiment, the use of an ion species with a low charge-to-mass ratio, would delay the onset of this motion. This may be achieved with a high-Z ion species. Figure 4.9 shows the rate of channel formation for 3 ion species. The

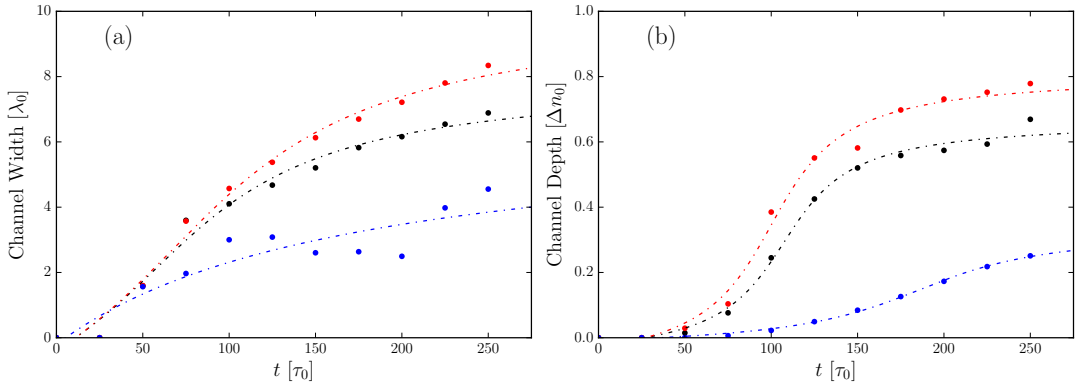

Figure 4.9: Ion channel formation rate for three ion species; H^{+1} (red), Ar^{+18} (black) and Ar^{+1} (blue) characterised by (a) channel width, defined as the radial point at which density is equal to the plasma plateau density, and (b) channel depth, defined as the density at $r = 0$. The channel is not uniform, so a slice at $z = 30\lambda_0$ is chosen to illustrate the typical rates. The results are fitted to arctangent regressions, assuming the channel width and depth ultimately plateaus as ion momentum is disappated.

channel for the H^{+1} ($q/m \sim 10^8$) plasma forms the fastest, with Ar^{+18} ($q/m \sim 10^7$) and Ar^{+1} ($q/m \sim 10^6$) following in order of decreasing charge/mass. The use of Ar^{+1} is illustrative, as the high plasma temperature would fully ionise argon, but despite the much lower charge/mass ratio, a channel forms nonetheless. The effect of mixed-ion plasmas and partially ionised species are worthy of further study, but beyond the scope of this work.

4.5 Conclusions

We have investigated the phenomena of magnetic field amplification by high power lasers, and demonstrated its viability for quasistatic magnetic fields lasting tens to hundreds of laser periods. The field appears ponderomotively driven, allowing lasers of arbitrary polarisation and field configuration to be employed, given a suitable seed field. The field itself is sustained by an azimuthal current induced in the wake of the laser pulse.

The induced field scales with both laser amplitude and plasma density, with no theoretical limit. Dense plasmas with ultraintense lasers may be capable of supporting fields into the tens of kiloteslas. It is interesting that while extremely strong magnetic fields may be produced, the overall energy contained within the relevant field component remains small when compared to the other components. This is likely due to the extremely compact nature of the field structure, but may suggest a way to improve the efficiency of the process and realise stronger fields given further research.

The extremely hot nature of the plasma generated suggests and extremely long timescale for collisional losses. However, this potential is tempered by the fact that ion motion inevitably disrupts the currents as an evacuated channel forms in the path of the laser, and this occurs on a much faster timescale than collisions. Despite this, the strong fields still persist for hundreds of femtoseconds at least, making them of useful duration nontheless. This limitation may be further mitigated by the use of an ion species with a low charge-to-mass ratio to slow the ion motion further.

Chapter 5

Summary and Outlook

This thesis presents the theoretical framework and numerical investigation of envelope dynamics of short pulse lasers in plasma, under the influence of strong magnetic fields.

The first section of this thesis covers weakly relativistic laser dynamics in quite sparse plasma $n_e < 0.1n_c$, with a focus on the effects stemming from the external magnetic field. A strong external magnetic field dramatically alters the elctron response under circularly polarised light. In the non whistler regime ($\omega_c < \omega_0$), the weakly-relativistic regime is described by the condition $a_0^2\eta_0^2 \ll 1$. For LCP light this means a damped electron response, extending the weakly-relativistic regime into traditionally fully-relativistic light intensities. For RCP light this curtains the weakly-relativistic regime even further, resulting in increased instability growth, absorption and wavebreaking effects at much lower light intensities. These polarisation effects may be employed to either allow access to fully-relativistic processes in low-power laser systems, or examine weakly-relativistic effects in high-power systems. At resonance ($\omega_c = \omega_0$), the plasma is entirely absorbing to RCP light. By contrast LCP light experiences no such resonant point. The analagous resonance for LCP light is governed by the ion cyclotron frequency, and is both of too low a frequency, and too minor magnitide to be relevant. An electron-positron plasma would have a strong resonance for both RCP and LCP light, and may be an interesting avenue of study. In the whistler regime ($\omega_c > \omega_0$), a laser pulse may propagate through arbitrarily dense plasma, and relativistic effects can serve to bring the plasma back to an absorbing resonant state as $\omega_c/\gamma \to \omega_0$. As this is independent of density, it may offer a method to measure the field in a plasma given a known probe laser intensity.

The second section of this thesis considers a more quantitative method of describing pulse propagation, by employing the varitional method to generate parameter functions describing both the transverse and longitudinal dynamics in a more self-consistent way. The specific case

of symmetric evolution is studied in detail, and its viability as a method of causing complete pulse collapse is demonstrated. The parameter range for such collapses emcompass a large range of potential plasma and pulse parameters. In the strictly weakly-relativistic regime a pulse may be smoothly compressed to the lambda-cubic, and a corresponding large increase in intensity achieved. The use of a magnetic field is accounted for by the evolution equations, and may be used to compress pulses of arbitrary shape, due to the fact that the longitudinal and transverse compression rates do not scale equally when a magnetic field is applied. This allows for the possibility that carefully chosen plasma and magnetic field parameters may allow access to compression for a very wide range of pulse shapes and intensities. High intensity pulses may also be compressed towards the lambda-cubic regime, but the overall efficiency is much reduced, as there are significant losses to absorption, and the exact mechanism of compression moves from a purely envelope model, to a ponderomotively driven process.

The final section considers how intense lasers may be used to further enhance an imposed magnetic field by ponderomotively-driven circulating currents, sustained by the background B-field. Given a suitable seed field, an intense laser or arbitrary polarisation and mode may induce an extremely strong quasistatic magnetic field along the laser propagation axis. This field scales with the laser intensity and plasma density, as both contribute to driving the strong azimuthal currents needed to sustain the magnetic field. The induced field may reach an order of magnitude higher than the seed field, which seems to have an optimal level around $\omega_c/\omega_0 \sim 0.1$, corresponding to 10^2-10^3 T depending on the laser wavelength. The field is relatively long-lived, limited by ion motion, which disrupts the azimuthal currents. The use of high-Z or otherwise plasma with a low average q/m may mitigate this and prolong the life of the magnetic field.

Moving forward, the work done over the course of this project may find application in high-power laser experiments. The pure envelope dynamics may be of interest to plasma-based accelerator physics and inertial confinement fusion. Optical schemes for generation of extremely strong and compact magnetic fields may be of relevance to magnetically-assisted fast ignition, as a means of collimating electrons into the compressed fuel more efficiently, and for radiation production, from deflecting relativistic particle beams.

Chapter 3 highlights the need to look further into the discrepancies arising from simplfied evolution models. Theory and simulation results differ in predicted collapse distance, and while this discrepancy is less important at high intensities, where envelope dynamics are no longer dominated by the purely relativistic effects underlying the evolution equations we derive, the source of this discrepancy should be studied in order to improve understanding of the limitations of such models. We also note a lack of work on post-soliton formation in magnetised

plasmas, where we see relatively long-lived solitons in 3D geometry, a phenomenon usually associated with 2D simulations, and the unrealistic electron motion this reproduces. This work suggests such phenomena are indicative of a partial or complete pulse collapse, and may be useful to experimentalists to identify with reasonable accuracy the location of collapse events. Additionally, the envelope evolution equations derived here, may be applied to higher-order beam modes, such as LG modes, by considering the symmetry of the amplitude profiles and constructing approximate profiles by superposition of simpler profiles. The radial profile as a 2D envelope with cylindrical symmetry suggests higher-order LG or HG beams would collapse down to ring structured or rectilinear arrays of pulses. Given the strong ponderomotive forces observed when fundamental Gaussian pulses are tightly focused and compressed, higher modes would potentially cause ordered patterns or ring-shaped post-soliton cavities, which may offer a novel method to structure the plasma density and diffract subsequent beams.

Chapter 4 also suggests further study of both the underlying mechanisms, and the detailed scaling of magnetic field amplification. Additionally, the questions arising from the huge angular momentum gain by the plasma, and apparent violation of the related conservation laws would be best examined experimentally, given that the practicalities of studying such strong ambient magnetic fields preclude a self-consisten method of generation.

In all cases, there is clear motivation to study in more detail the effects of moving beyond the weakly-relativistic regime. We consistently see deviations from the models due to laser intensity growth pushing into the fully relativistic regime. This in turn causes electron acceleration and introduces ponderomotive effects not accounted for by the models. As a clear next step this would both improve the applicability of the envelope models, and give a more accurate description overall of the dynamics in all cases.

Appendix A

Calculating Electron Motion

This appendix contains the details of calculating particle orbits under light of arbitrary polarisation and arbitrary external magnetic field strength. Consider the plasma to be initially cold. Individual electron motion is given by the Lorentz equation

$$m\frac{\partial \boldsymbol{v}}{\partial t} = q\left(\boldsymbol{E} + \boldsymbol{v} \times \boldsymbol{B}\right). \tag{A.1}$$

We may linearise by assuming plane-wave solutions for $\boldsymbol{E}$, and further simplify by assuming the interaction is nonrelativistic, ie. $v \ll c$ allowing us to discount the laser magnetic field.

$$\boldsymbol{E} = \hat{\boldsymbol{e}}_{\boldsymbol{x}} E_x + \hat{\boldsymbol{e}}_{\boldsymbol{y}} E_y. \tag{A.2}$$

The static magnetic field

$$\boldsymbol{B} = \hat{\boldsymbol{e}}_{\boldsymbol{z}} \delta B_z, \tag{A.3}$$

is aligned along $\boldsymbol{k}$, with the direction of the field is determined by δ, which takes values of 1 or -1 corresponding to R and L modes.

Derivatives are linearied accordingly

$$\frac{\partial}{\partial t} f(t) = -i\omega f(t), \tag{A.4}$$

$$\int f(t)\,\mathrm{d}t = \frac{i}{\omega} f(t) + C. \tag{A.5}$$

Initial substitution gives us

$$-i\omega m \begin{pmatrix} v_x \\ v_y \\ 0 \end{pmatrix} = q \left[\begin{pmatrix} E_x \\ E_y \\ 0 \end{pmatrix} + \begin{vmatrix} \hat{\boldsymbol{e}}_{\boldsymbol{x}} & \hat{\boldsymbol{e}}_{\boldsymbol{y}} & \hat{\boldsymbol{e}}_{\boldsymbol{z}} \\ v_x & v_y & 0 \\ 0 & 0 & \delta B_z \end{vmatrix} \right], \tag{A.6}$$

which seperates to

$$-im_e\omega v_x = q(E_x + v_y \delta B_z), \tag{A.7}$$

$$-im_e\omega v_y = q(E_y - v_x \delta B_z). \tag{A.8}$$

We now introduce the signed cyclotron frequency $\Omega_c = \delta\omega_c = e\delta B_z/m_e$ and solve (A.7) and (A.8) simultaneously for $v_{\{x,y\}}$ in terms of $E_{\{x,y\}}$

$$v_x = \frac{q}{m}\left[\frac{i\omega E_x - \Omega_c E_y}{\omega^2 - \Omega_c^2}\right], \tag{A.9}$$

$$v_y = \frac{q}{m}\left[\frac{i\omega E_y + \Omega_c E_x}{\omega^2 - \Omega_c^2}\right]. \tag{A.10}$$

Now we may integrate to retrieve expressions for position

$$x = -\frac{q}{\omega m}\left[\frac{\omega E_x + i\Omega_c E_y}{\omega^2 - \Omega_c^2}\right] + C, \tag{A.11}$$

$$y = \frac{q}{\omega m}\left[\frac{i\Omega_c E_x - \omega E_y}{\omega^2 - \Omega_c^2}\right] + C. \tag{A.12}$$

Substituting appropriate values for Ω_c, m and q, and an expression for E allow the orbits for arbitrary particles in arbitrary fields to be determined

Appendix B

Variational method workings

This appendix details the variational method as applied in chapter 3 leading to (3.3) and (3.4).

B.1 Obtaining the Reduced Lagrangian

The governing NLSE is given by

$$2i\frac{\partial\psi}{\partial z} + \nabla_\perp^2\psi + \epsilon_1\frac{\partial^2\psi}{\partial\tau^2} + \epsilon_2|\psi|^2\psi = 0, \tag{B.1}$$

and we take a test envelope function

$$\psi = A(z)\exp\left[-\frac{x^2+y^2}{R^2(z)} - \frac{\tau^2}{D^2(z)} + iB(z)(x^2+y^2) + iC(z)\tau^2\right], \tag{B.2}$$

where $A(z)$ is the complex amplitude, $R(z)$ is the spot radius, $D(z)$ is the pulse duration, $B(z)$ is the transverse phase term and $C(z)$ is the longitudinal chirp term. The variational principle requires that the lagrangian energy density $\mathcal{L}$ satisfies

$$\sum_{j\in\mathcal{X}}\left[\frac{\partial}{\partial j}\left(\frac{\partial\mathcal{L}}{\partial[\partial_j(\psi^*)]}\right)\right] - \frac{\partial\mathcal{L}}{\partial\psi^*} = 0 \tag{B.3}$$

$$\mathcal{X} = \{x, y, z, \tau\}$$

Such a lagrangian is given by

$$\mathcal{L} = i\left(\psi\frac{\partial\psi^*}{\partial z} - \psi^*\frac{\partial\psi}{\partial z}\right) + \left|\frac{\partial\psi}{\partial y}\right|^2 + \left|\frac{\partial\psi}{\partial x}\right|^2 + \epsilon_1\left|\frac{\partial\psi}{\partial\tau}\right|^2 - \frac{\epsilon_2}{2}|\psi|^4. \tag{B.4}$$

Appendix B. Variational method workings

First we evaluate (B.4), requiring the derivatives of ψ

$$\frac{\partial\psi}{\partial z} = \frac{\mathrm{d}A}{\mathrm{d}z}\frac{\psi}{A} + \psi\left(\frac{2r^2}{R^3}\frac{\mathrm{d}R}{\mathrm{d}z} + \frac{2\tau^2}{D^3}\frac{\mathrm{d}D}{\mathrm{d}z} + ir^2\frac{\mathrm{d}B}{\mathrm{d}z} + i\tau^2\frac{\mathrm{d}C}{\mathrm{d}z}\right), \tag{B.5a}$$

$$\frac{\partial\psi^*}{\partial z} = \frac{\mathrm{d}A^*}{\mathrm{d}z}\frac{\psi^*}{A^*} + \psi\left(\frac{2r^2}{R^3}\frac{\mathrm{d}R}{\mathrm{d}z} + \frac{2\tau^2}{D^3}\frac{\mathrm{d}D}{\mathrm{d}z} - ir^2\frac{\mathrm{d}B}{\mathrm{d}z} - i\tau^2\frac{\mathrm{d}C}{\mathrm{d}z}\right), \tag{B.5b}$$

$$\frac{\partial\psi}{\partial y} = \psi\left(-\frac{2y}{R^2} + 2iyB\right), \tag{B.5c}$$

$$\frac{\partial\psi}{\partial x} = \psi\left(-\frac{2x}{R^2} + 2ixB\right), \tag{B.5d}$$

$$\frac{\partial\psi}{\partial \tau} = \psi\left(-\frac{2\tau}{D^2} + 2i\tau C\right). \tag{B.5e}$$

The reduced lagrangian is given by integrating over all dependent variables we wish to eliminate;

$$\langle\mathcal{L}\rangle = \int_{-\infty}^{\infty}\int_{-\infty}^{\infty}\int_{-\infty}^{\infty}\mathcal{L}\,\mathrm{d}\tau\mathrm{d}y\mathrm{d}x. \tag{B.6}$$

We may also define for reference

$$|\psi|^2 = |A|^2\exp\left[-\frac{2x^2}{R^2} - \frac{2y^2}{R^2} - \frac{2\tau^2}{D^2}\right], \tag{B.7a}$$

$$|\psi|^4 = |A|^4\exp\left[-\frac{4x^2}{R^2} - \frac{4y^2}{R^2} - \frac{4\tau^2}{D^2}\right], \tag{B.7b}$$

$$\left|\frac{\partial\psi}{\partial x}\right|^2 = |\psi|^2\left(\frac{4x^2}{R^2} + 4x^2B^2\right), \tag{B.7c}$$

$$\left|\frac{\partial\psi}{\partial y}\right|^2 = |\psi|^2\left(\frac{4y^2}{R^2} + 4y^2B^2\right), \tag{B.7d}$$

$$\left|\frac{\partial\psi}{\partial \tau}\right|^2 = |\psi|^2\left(\frac{4\tau^2}{D^2} + 4\tau^2C^2\right), \tag{B.7e}$$

$$\psi\psi^{*\prime} = |\psi|^2\left[\frac{A^{*\prime}}{A^*} + (x^2+y^2)\left(\frac{2R^\prime}{R^3} - iB^\prime\right) + \tau^2\left(\frac{2D^\prime}{D^3} - iC^\prime\right)\right], \tag{B.7f}$$

$$\psi^*\psi^\prime = |\psi|^2\left[\frac{A^\prime}{A} + (x^2+y^2)\left(\frac{2R^\prime}{R^3} + iB^\prime\right) + \tau^2\left(\frac{2D^\prime}{D^3} + iC^\prime\right)\right], \tag{B.7g}$$

$$\psi\psi^{*\prime} - \psi^*\psi^\prime = |\psi|^2\left[\frac{A^{*\prime}}{A^*} - \frac{A^\prime}{A} - (x^2+y^2)2iB^\prime - \tau^2 2iC^\prime\right]. \tag{B.7h}$$

From here we may combine the above equations and evaluate $\langle\mathcal{L}\rangle$ using textbook gaussian integrals. After some algebra we arrive at

$$\langle\mathcal{L}\rangle = \left(\frac{\pi}{2}\right)^{3/2} DR^2[i(AA^{*\prime} - A^*A') + |A|^2\cdot \\ [B'R^2 + C'D^2/2 + 2R^2(R^{-4} + B^2) + \epsilon_1 D^2(D^{-4} + C^2)] - |A|^4\epsilon_2 2^{-5/2}]. \quad \text{(B.8)}$$

We may compact this by defining the following convenience functions

$$\varphi = AA^{*\prime} - A^*A', \quad \text{(B.9a)}$$

$$\theta = B'R^2 + C'D^2/2 + 2R^2(R^{-4} + B^2) + \epsilon_1 D^2(D^{-4} + C^2), \quad \text{(B.9b)}$$

$$\phi = \epsilon_2 2^{-5/2}, \quad \text{(B.9c)}$$

and write the reduced lagrangian in a more manageable form

$$\langle\mathcal{L}\rangle = \left(\frac{\pi}{2}\right)^{3/2} DR^2\left[i\varphi + |A|^2\theta - |A|^4\phi\right]. \quad \text{(B.10)}$$

B.2 Variations of the Parameter Functions

The general form for variations on a function $A(z)$ is given by

$$\frac{\delta\langle\mathcal{L}\rangle}{\delta A} = \frac{\partial}{\partial z}\frac{\partial\langle\mathcal{L}\rangle}{\partial\left(\frac{\partial A}{\partial z}\right)} - \frac{\partial\langle\mathcal{L}\rangle}{\partial A} = 0. \quad \text{(B.11)}$$

We require variations on all parameter functions, starting with A:

$$\frac{\partial}{\partial z}\frac{\partial\langle\mathcal{L}\rangle}{\partial\left(\frac{\partial A}{\partial z}\right)} = -i\left(\frac{\pi}{2}\right)^{3/2}\frac{\mathrm{d}}{\mathrm{d}z}[DR^2A^*], \quad \text{(B.12)}$$

$$\frac{\partial\langle\mathcal{L}\rangle}{\partial A} = \left(\frac{\pi}{2}\right)^{3/2} DR^2\left[iA^{*\prime} + A^*\theta - 2A^*|A|^2\phi\right], \quad \text{(B.13)}$$

$$-i\frac{\mathrm{d}}{\mathrm{d}z}[DR^2A^*] = DR^2\left[iA^{*\prime} + A^*\theta - 2A^*|A|^2\phi\right]. \quad \text{(B.14)}$$

Variations of A^*:

$$\frac{\partial}{\partial z}\frac{\partial\langle\mathcal{L}\rangle}{\partial\left(\frac{\partial A^*}{\partial z}\right)} = i\left(\frac{\pi}{2}\right)^{3/2}\frac{\mathrm{d}}{\mathrm{d}z}[DR^2A], \quad \text{(B.15)}$$

$$\frac{\partial\langle\mathcal{L}\rangle}{\partial A^*} = \left(\frac{\pi}{2}\right)^{3/2} DR^2\left[-iA' + A\theta - 2A|A|^2\phi,\right] \quad \text{(B.16)}$$

$$i\frac{\mathrm{d}}{\mathrm{d}z}[DR^2A] = DR^2\left[-iA' + A\theta - 2A|A|^2\phi\right]. \tag{B.17}$$

Now multiply (B.14) and (B.17) by their conjugates and subract to obtain

$$-i\left[\frac{\mathrm{d}}{\mathrm{d}z}(DR^2A^*)A + \frac{\mathrm{d}}{\mathrm{d}z}(DR^2A)A^*\right] = DR^2[i(A^{*\prime}A + A'A^*)]. \tag{B.18}$$

From here, expand the derivatives to obtain the constant of motion for the system, i.e. the EM energy conservation equation

$$\frac{\mathrm{d}}{\mathrm{d}z}(|A|^2R^2D) = 0, \tag{B.19}$$

which states the while the individual parameter functions may vary with z, the total energy does not change from its initial value $\mathcal{E}_0$. We may hence write this in terms of the parameter function initial values; $A(0) = A_0$, $R(0) = R_0$ and $D(0) = D_0$:

$$|A|^2R^2D = |A_0|^2R_0^2D_0 = \mathcal{E}_0. \tag{B.20}$$

Next, multiply (B.14) and (B.17) by their conjugates and add, to obtain the useful relation

$$-i\varphi = |A|^2\theta - 2|A|^4\phi. \tag{B.21}$$

Now perform variations on the remaining parameter functions, starting with B:

$$\frac{\partial\langle\mathcal{L}\rangle}{\partial B} = \left(\frac{\pi}{2}\right)^{3/2} DR^2|A|^2[4R^2B], \tag{B.22}$$

$$\frac{\mathrm{d}}{\mathrm{d}z}\frac{\partial\langle\mathcal{L}\rangle}{\partial B'} = \left(\frac{\pi}{2}\right)^{3/2} \frac{\mathrm{d}}{\mathrm{d}z}[DR^4|A|^2]. \tag{B.23}$$

Recall (B.19) and hence obtain

$$\frac{\mathrm{d}R}{\mathrm{d}z} = 2RB. \tag{B.24}$$

After R is known, B may be found as

$$B = \frac{1}{2}\frac{\mathrm{d}\ln(R)}{\mathrm{d}z}. \tag{B.25}$$

Variations for C:

$$\frac{\partial\langle\mathcal{L}\rangle}{\partial C} = \left(\frac{\pi}{2}\right)^{3/2} DR^2|A|^2[2\epsilon_1CD^2], \tag{B.26}$$

$$\frac{\mathrm{d}}{\mathrm{d}z}\frac{\partial\langle\mathcal{L}\rangle}{\partial C'} = \left(\frac{\pi}{2}\right)^{3/2} \frac{1}{2}\frac{\mathrm{d}}{\mathrm{d}z}[D^3R^2|A|^2]. \tag{B.27}$$

Appendix B. Variational method workings

As before, recall (B.19) and obtain

$$\frac{\mathrm{d}D}{\mathrm{d}z} = 2\epsilon_1 CD. \tag{B.28}$$

After D is known, C may be found as

$$C = \frac{1}{2\epsilon_1}\frac{\mathrm{d}\ln(D)}{\mathrm{d}z}. \tag{B.29}$$

Variations for D:

$$\frac{\partial\langle\mathcal{L}\rangle}{\partial D} = \left(\frac{\pi}{2}\right)^{3/2} R^2\left[i\varphi + |A|^2\left[B'R^2 + \frac{3}{2}C'D^2 + 2R^2(B^2+R^{-4}) - \epsilon_1 D^{-2} + 3\epsilon_1 D^2C^2\right] - |A|^4\phi\right], \tag{B.30}$$

$$\frac{\mathrm{d}}{\mathrm{d}z}\frac{\partial\langle\mathcal{L}\rangle}{\partial D'} = 0. \tag{B.31}$$

Set (B.30) equal to (B.31) and then equate to (B.21) to obtain

$$C'D^2 - 2\epsilon_1 D^{-2} + 2\epsilon_1 D^2C^2 = -|A|^2\phi. \tag{B.32}$$

Variations for R:

$$\frac{\partial\langle\mathcal{L}\rangle}{\partial R} = \left(\frac{\pi}{2}\right)^{3/2} 2DR\left[i\varphi + |A|^2[2B'R^2 + C'D^2/2 + 4B^2R^2 + \epsilon_1 D^2(C^2+D^{-4})] - |A|^4\phi\right], \tag{B.33}$$

$$\frac{\mathrm{d}}{\mathrm{d}z}\frac{\partial\langle\mathcal{L}\rangle}{\partial R'} = 0. \tag{B.34}$$

Set (B.33) equal to (B.34) and then equate to (B.21) to obtain

$$R^2B' + 2B^2R^2 - 2R^{-2} = -|A|^2\phi. \tag{B.35}$$

Equations (B.24) and (B.35) are coupled and can be combined to get

$$R'' = \frac{4}{R^3}\left(1 - \frac{E_0\phi}{2D}\right). \tag{B.36}$$

Similarly (B.28) and (B.32) are coupled and can be combined to get

$$D'' = \frac{4\epsilon_1^2}{D^3}\left(1 - \frac{E_0\phi D}{2\epsilon_1^2R^2}\right). \tag{B.37}$$

We may normalise $\tilde{R} = R/R_0$ and $\tilde{D} = D/D_0$ resulting in

$$R'' = \frac{4}{R^3R_0^4}\left(1 - \frac{A_0^2R_0^2\phi}{2D}\right), \tag{B.38}$$

$$D'' = \frac{4\epsilon_1^2}{D^3 D_0^4}\left(1 - \frac{A_0^2 D D_0^2 \phi}{2\epsilon_1 R^2}\right). \tag{B.39}$$

Recalling that $\phi = \epsilon_2 2^{-5/2}$, we may retrieve the exact forms used in chapter 3.

Appendix C

Code Comparison - Osiris and FBPIC

Here we provide some comparisons of the OSIRIS and FBPIC codes used. We compare two simulations in-full, and focus on the essential physics of the envelope dynamics, in particular the dynamics up to the first collapse. We conclude OSIRIS and FBPIC agree well enough, up to the point of first collapse.

The first case of comparison between OSIRIS and FBPIC is the simulation discussed in section 3.1 of the main work. This is an unmagnetised plasma with $n_0 = 0.475$ and a laser with initial parameters $R_0 = 10\lambda_0$, $D_0 = 13\tau_0$ and $a_0 = 0.12$. We compare the on-axis intensity in figure C.1, fitted parameter evolution in figure C.2. We see from figure C.1 that qualatatively there is very good agreement between the two codes, FBPIC exhibits more noise after the laser has passed, but this is a perennial feature of cylindrical codes, due to algorthmic difficulties in dealing with the axis. The effect of this noise is negligible in our work. More quantative comparison is given by figure C.2, which compares the fitted parameters for beam spot size, duration and peak amplitude. Up to the first collapse, over the course of the simulation, all major features are reproduced by both codes, with small differences arising in terms of the focusing dynamics. The initial point of collapse differs by only a few wavelengths.

The second case of comparison between OSIRIS and FBPIC is the simulation discussed in section 3.2 of the main work. This is a magnetised plasma with $n_0 = 0.15$ and $B = 0.5$ and a laser with initial parameters $R_0 = 10\lambda_0$, $D_0 = 13\tau_0$ and $a_0 = 0.06$. We again compare the on-axis intensity in figure C.3, fitted parameter evolution in figure C.4. We see from figure C.3 that qualatatively there is mostly good agreement between the two codes. The compression is again spherical in both codes, however the time-to-collapse is more noticeably greater in FBPIC

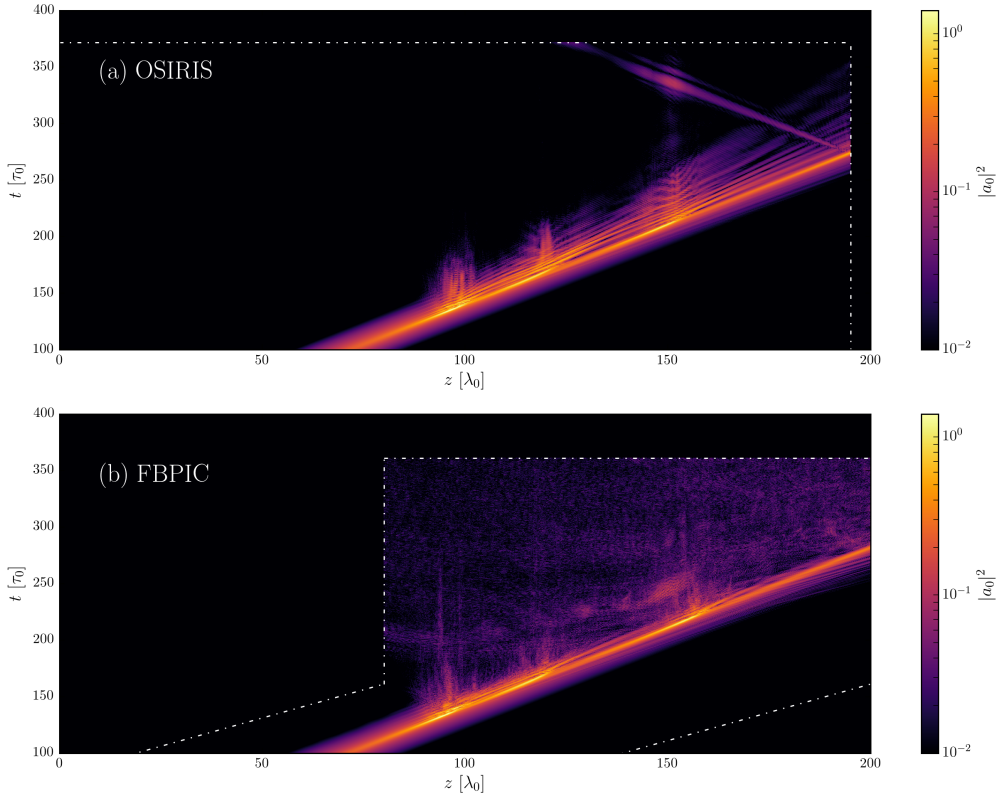

Figure C.1: Comparison of (a) on-axis envelope of an OSIRIS simulation to (b) the same information from an FBPIC simulation of equivalent parameters. The dot-dashed lines show the simulation spatial and time domain extents. An initially moving window was used for the FBPIC case, which was then halted to allow for comparison of post-soliton dynamics.

than in the unmagnetised plasma case. This is most evident in figure C.4, and is possibly due to the sensitive nature of the regime. Small differences in laser initialisation or energy partitioning may give rise to this discrepancy. Most evident is the lack of a third collapse in the FBPIC simulation. We observe the pulse remnant amplitude rising as it leaves the simulation box, so it is reasonable to conclude that if the box was larger, the third collapse even would eventually occur. However, it would do so significantly after that of the OSIRIS simulation.

In all cases, the key result of the work, i.e. spherical compression in the run up to the first collapse, is well-reproduced by both codes, with the only appreciable differences being the variations in the distance-to-collapse. For this reason we feel that the use of both OSIRIS and FBPIC in tandem is well justified, up to the point of first collapse. Beyond this, agreement is still largely good, but less consistent, and in magnetised plasma, the results diverge more strongly. As such in section 3.3 we choose to only examine unmagnetised plasma using FBPIC alone.

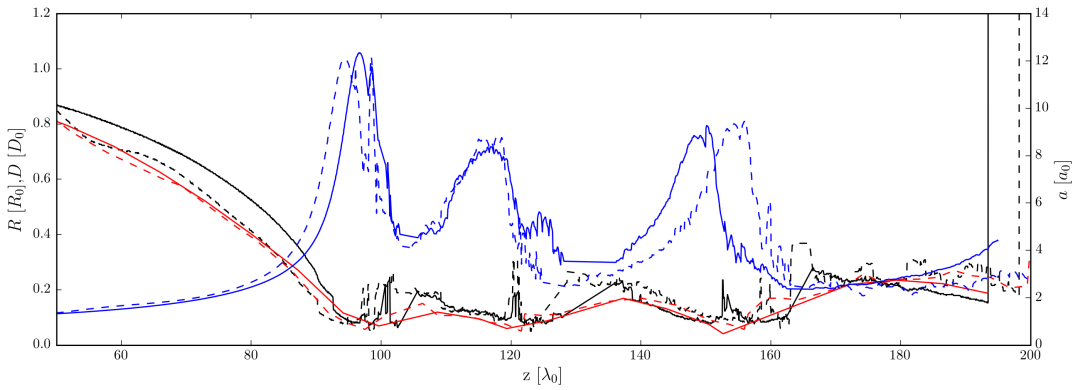

Figure C.2: A comparison of the fitted parameters, R (red), D (black) and a (blue). The OSIRIS results are represented by solid lines, and FBPIC simulation by dashed lines.

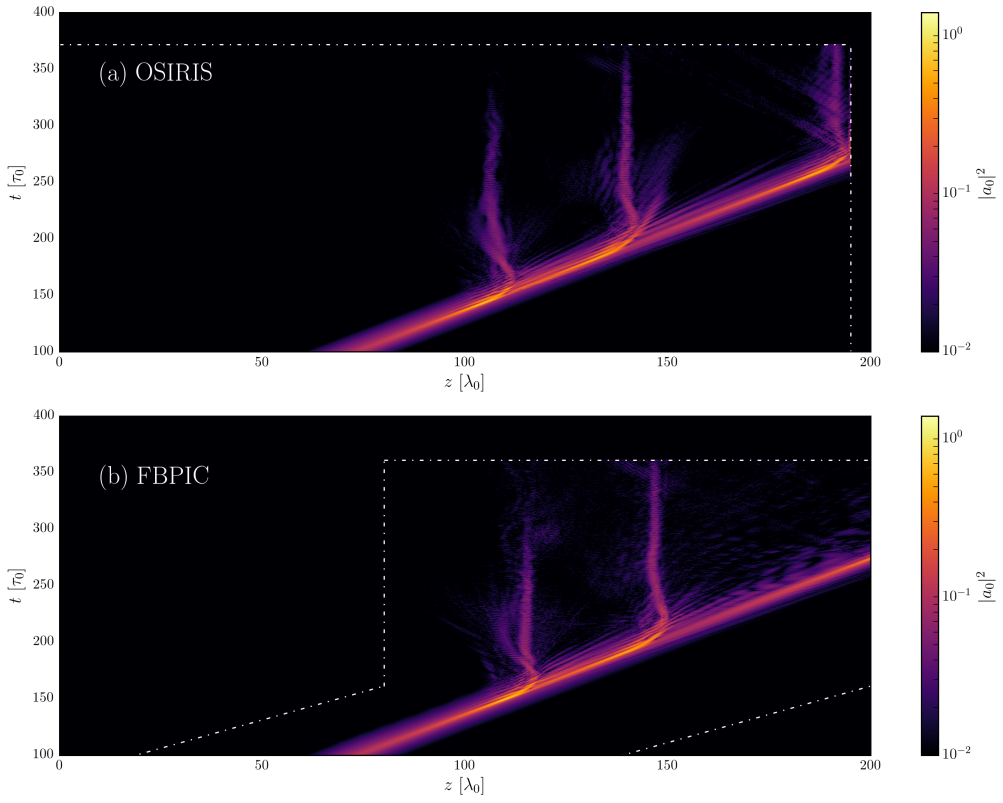

Figure C.3: Comparison of (a) on-axis envelope of an OSIRIS simulation to (b) the same information from an FBPIC simulation of equivalent parameters. The dot-dashed lines show the simulation spatial and time domain extents. An initially moving window was used for the FBPIC case, which was then halted to allow for comparison of post-soliton dynamics.

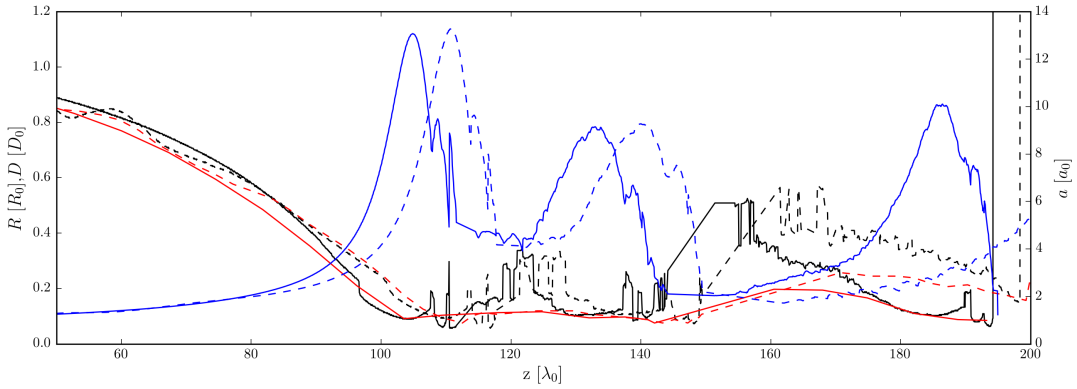

Figure C.4: A comparison of the fitted parameters, R (red), D (black) and a (blue). The OSIRIS results are represented by solid lines, and FBPIC simulation by dashed lines.

Appendix D

Plasma Angular Momentum

This appendix contains a discussion of how one may calculate the instantaneous angular momentum of a plasma under the influence of light carrying some arbitrary angular momentum. The angular momentum along z of a single particle in a plasma is given by

$$L_z = xp_y - yp_x. \tag{D.1}$$

where x, y are the particle positions p_x, p_y the particle momentum components and all are functions of time. Assuming each particle experiences an electric field of the form

$$\Re\{\boldsymbol{E}\} = E_x\hat{\boldsymbol{e}}_{\boldsymbol{x}}\cos(l\theta - \omega t) - E_x\hat{\boldsymbol{e}}_{\boldsymbol{y}}\sin(l\theta - \omega t) \tag{D.2}$$

i.e. a laser of arbitrary polarisation and azimuthal mode, with components, where l is the azimuthal mode index relevant to LG beams and E_x and E_y may have some envelope. Electron motion may be described via solutions to the linearised Lorentz force equation. These are (see appendix A)

$$p_x(t) = \frac{q}{\omega}\left[\frac{BE_y - E_x}{1 - B^2}\right]\sin(l\theta - \omega t) = C_{p_x}\sin(l\theta - \omega t), \tag{D.3}$$

$$p_y(t) = \frac{q}{\omega}\left[\frac{BE_x - E_y}{1 - B^2}\right]\cos(l\theta - \omega t) = C_{p_y}\cos(l\theta - \omega t), \tag{D.4}$$

$$x(t) = \frac{q}{\omega^2 m}\left[\frac{BE_y - E_x}{1 - B^2}\right]\cos(l\theta - \omega t) = C_x\cos(l\theta - \omega t), \tag{D.5}$$

$$y(t) = \frac{q}{\omega^2 m}\left[\frac{E_y - BE_x}{1 - B^2}\right]\sin(l\theta - \omega t) = C_y\sin(l\theta - \omega t). \tag{D.6}$$

now including an optional external magnetic field along z denoted by B. We introduce the C coefficients for brevity. We may analytically determine the angular momentum of a volume of

plasma by integrating over the volume. For a homogeneous plasma of density n_e, in cylindrical coordinates we have the total angular momentum

$$L_z = n_e \int_{-\infty}^{\infty} \int_0^{2\pi} \int_0^{\infty} [(r\cos(\theta) - x)p_y - (r\sin(\theta) - y)p_x]\, r\mathrm{d}r\mathrm{d}\theta\mathrm{d}z. \tag{D.7}$$

where the particle positions are now displaced as $r\cos(\theta) - x$ and $r\sin(\theta) - y$ to represent all parts of the plasma volume. For a finite pulse envelope, the r and z parts of the integral will reduce to constants relating to the beam profile. The azimuthal part of the integral is of interest on its own;

$$L_z \propto \int_0^{2\pi} [r\cos(\theta)p_y - xp_y - r\sin(\theta)p_x + yp_x]\, \mathrm{d}\theta. \tag{D.8}$$

Evaluating this gives a two-part function with an oscilliatory term and a DC term

$$L_z \propto r(lC_{p_y} - C_{p_x})\frac{2\sin(\pi l)\cos(\pi l - \omega t)}{l^2 - 1} + 2\pi C_0, \tag{D.9}$$

where we have made use of the fact that $C_x C_{p_y} = -C_y C_{p_x} = C_0$. The oscilliatory part is nonzero only if l takes the values 1, -1, or any non-integer, and averaging this over time reduces the contribution to zero, no net transfer occurs. The static term is nonzero when the laser is either circularly polarised, or there is some background magnetic field, and once again disappears once the laser influence is removed. This affirms that while beams with intrinsic angular momentum will indeed impart it to plasma, beams without intrinsic angular momentum ($l = 0$) may also impart angular momentum through $L_{\text{const.}}$ when $|B_z| > 0$. The method employed here does not take energy loss to the plasma into account, so any estimation of the plasma angular momentum after absorption has occured is beyond the scope of this treatment.

The oscilliatory part of the result is graphed in Figure D.1 for different l, and a few different values of ω_c/ω (at $t = 0$). The result suggests that an index of $|l| = 1$ is the only integer mode capable of transfering AM to the plasma, even temporarily. It also implies that non-integer modes may impart OAM, and while these are not strictly solutions of the wave equation, they may be approximated by superpositions of modes, such as found in light-springs. Applying an external field biases the plasma towards a particular l, when $|\omega_c/\omega| = 1$ only l of matching sign will contribute AM to the plasma, the antiparallel l will not cause AM contribution. However this does not stop the static term from contributing.

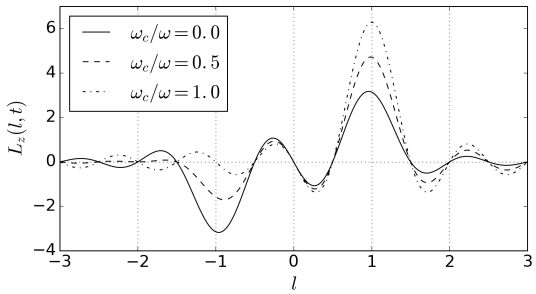

Figure D.1: Angular momentum as a function of azimuthal mode index l.

List of Publications

Publications and presentations relating to this research to date:

[1] T. C. Wilson, F. Y. Li, M. Weikum, and Z. M. Sheng, "Influence of strong magnetic fields on laser pulse propagation in underdense plasma," *Plasma Phys. Control. Fusion*, vol. 59, p. 065002, 2017.

[2] T. C. Wilson, F. Y. Li, M. Weikum, and Z. M. Sheng, "Influence of strong magnetic fields on laser pulse propagation in underdense plasma," poster presentation, European Physical Society 44th Plasma Physics Conference, Belfast, June 2017

[3] T. C. Wilson, F. Y. Li, S. M. Weng, M. Chen, P. McKenna, and Z. M. Sheng, "Laser pulse compression towards collapse and beyond in plasma," *J. Phys. B: At. Mol. Opt. Phys.*, vol. 52, p. 055403, 2019.

[4] T. C. Wilson, F. Y. Li, S. M. Weng, M. Chen, P. McKenna, and Z. M. Sheng, "Laser pulse compression towards collapse and beyond in plasma," oral presentation, International Conference on High Energy Density Physics, Oxford, May 2019.

Bibliography

[1] D. Strickland and G. Mourou. Compression of amplified chirped optical pulses. *Optics Communications*, 56:219, 1985.

[2] J. Schwinger. On gauge invariance and vacuum polarization. *Phys. Rev.*, 82:664, 1951.

[3] G. Dunne. New strong-field qed effects at extreme light infrastructure. *Eur. Phys. J. D*, 55:327, 2009.

[4] G. Mourou and T. Taijma. The extreme light infrastructure: Optics' next horizon. *Optics and Photonics News*, 22:47, 2011.

[5] H. Y. Wang, C. Lin, Z. M. Sheng, et al. Laser shaping of a relativistic intense, short gaussian pulse by a plasma lens. *Phys. Rev. Lett.*, 107:265002, 2011.

[6] S. Semushin and V. Malka. High density gas jet nozzle design for laser target production. *Review of Scientific Instruments*, 72:2961, 2001.

[7] S Fujioka et al. Kilotesla magnetic field due to a capacitor-coil target driven by high power laser. *Scientific Reports*, 3:1170, 2013.

[8] J. J. Santos et al. Laser-driven platform for generation and characterization of strong quasi-static magnetic fields. *New Journal of Physics*, 17:083051, 2015.

[9] Ph. Korneev, E. d'Humiéres, and V. Tikhonchuk. Gigagauss-scale quasistatic magnetic field generation in a snail-shaped target. *Phys. Rev. E*, 91:043107, 2015.

[10] T. Tajima and J. M. Dawson. Laser electron accelerator. *Phys. Rev. Lett.*, 43:267, 1979.

[11] C. Joshi et al. Ultrahigh gradient particle acceleration by intense laser-driven plasma density waves. *Nature*, 311:525, 1984.

[12] J. N. Rosenzwieg et al. Experimental observation of plasma wake-field acceleration. *Phys. Rev. Lett.*, 61:98, 1988.

[13] C. M. Tang and P. Sprangle. Dynamics of spacecharge waves in the laser beat wave accelerator. *Physics of Fluids*, 28:1974, 1985.

[14] E Esaray, J Krall, and P Sprangle. Envelope analysis of intense laser pulse self-modulation in plasmas. *Phys. Rev. Lett.*, 72:2887, 1994.

[15] N. Kumar and A. Pukhov. Self-modulation instability of a long proton bunch in plasmas. *Phys. Rev. Lett.*, 104:255003, 2010.

[16] A. N. Emilio et al. Terahertz-driven linear electron acceleration. *Nature Communications*, 6:8486, 2015.

[17] S. M. Hooker. Developments in laser-driven plasma accelerators. *Nature Photonics*, 7:775, 2013.

[18] A. J. Gonsalves et al. Petawatt laser guiding and electron beam acceleration to 8 gev in a laser-heated capillary discharge waveguide. *Phys. Rev. Lett.*, 122:084801, 2019.

[19] S. Benedetti et al. High gradient linac for proton therapy. *Physical Review Accelerators and Beams*, 20:040101, 2017.

[20] H. T. Kim et al. Enhancement of electron energy to the multi-gev regime by a dual-stage laser-wakefield accelerator pumped by petawatt laser pulses. *Phys. Rev. Lett.*, 111:165002, 2013.

[21] H. T. Kim et al. Stable multi-gev electron accelerator driven by waveform-controlled pw laser pulses. *Scientific Reports*, 7:10203, 2017.

[22] E. Esarey, C. B. Schroeder, and W. P. Leemans. Physics of laser-driven plasma-based electron accelerators. *Rev. Mod. Phys.*, 81:1229, 2009.

[23] S. Kiselev, A. Pukhov, and I. Kostyukov. X-ray generation in strongly nonlinear plasma waves. *Phys. Rev. Lett.*, 93:135004, 2004.

[24] S. Kneip et al. Observation of synchrotron radiation from electrons accelerated in a petawatt-laser-generated plasma cavity. *Phys. Rev. Lett.*, 100:105006, 2008.

[25] M. Chen et al. Tunable synchrotron-like radiation from centimeter scale plasma channels. *Light Sci. Appl.*, 5:16015, 2016.

[26] B. Liu et al. Quasimonoenergetic electron beam and brilliant gamma-ray radiation generated from near critical density plasma due to relativistic resonant phase locking. *Phys. Plasmas*, 22:080704, 2015.

[27] J. M. Di Nicola et al. The national ignition facility: laser performance status and performance quad results at elevated energy. *Nuclear Fusion*, 59:032004, 2019.

[28] J. Lindl et al. Review of the national ignition campaign 2009-2012. *Phys. Plasmas*, 21:020501, 2014.

[29] M. L. Spaeth et al. Description of the nif laser. *Fusion Science and Technology*, 69:25, 2016.

[30] P. K. Kaw. Nonlinear laser-plasma interactions. *Rev. Mod. Plasma Phys.*, 1:2, 2017.

[31] R. kodama et al. Fast heating of ultrahigh-density plasma as a step towards laser fusion ignition. *Nature*, 412:798, 2016.

[32] M. Bailly-Grandvaux et al. Guiding of relativistic electron beams in dense matter by laser-driven magnetostatic fields. *Nat. Commun.*, 9:102, 2018.

[33] W.-M. Wang, P. Giibbon, Z.-M. Sheng, and Y.-T. Li. Integrated simulation approach for laser-driven fast ignition. *Phys. Rev. E*, 91:013101, 2015.

[34] W. M. Wang, P. Gibbon, Z. M. Sheng, and Y. T. Li. Magnetically assisted fast ignition. *Phys. Rev. Lett.*, 114:015001, 2015.

[35] G. Shvets et al. Superradiant amplification of an ultrashort laser pulse in a plasmaby a counterpropagating pump. *Phys. Rev. Lett.*, 81:4879, 1998.

[36] V. M. Malkin, G. Shvets, and N. J. Fisch. Fast compression of laser beams to highly overcritical powers. *Phys. Rev. Lett.*, 82:4448, 1999.

[37] W. Cheng et al. Reaching the nonlinear regime of raman amplification of ultrashort laser pulses. *Phys. Rev. Lett.*, 94:045003, 2005.

[38] S. Weber et al. Amplification of ultrashort laser pulses by brillouin backscattering in plasmas. *Phys. Rev. Lett.*, 111:055004, 2013.

[39] W. B. Mori et al. Evolution of self-focusing of intense electromagnetic waves in plasma. *Phys. Rev. Lett.*, 60:1298, 1988.

[40] A. Pukhov and J. Meyer-ter Vehn. Relativistic magnetic self-channeling of light in near-critical plasma: Three-dimensional particle-in-cell simulation. *Phys. Rev. Lett.*, 76:3975, 1996.

[41] C. Ren et al. Compressing and focusing a short laser pulse by a thin plasma lens. *Phys. Rev. E*, 63:026411, 2001.

[42] C. Thaury et al. Plasma mirrors for ultrahigh-intensity optics. *Nat. Phys.*, 3:424, 2007.

[43] C. Thaury et al. Coherent dynamics of plasma mirrors. *Nat. Phys.*, 4:631, 2008.

[44] A. Leblanc et al. Plasma holograms for ultrahigh-intensity optics. *Nature Physics*, 13:440, 2017.

[45] C. G. Durfee, III and H. M. Milchberg. Light pipe for high intensity laser pulses. *Phys. Rev. Lett.*, 71:2409, 1993.

[46] H. M. Milchberg et al. Development and applications of a plasma waveguide for intense laser pulses. *Physics of Plasmas*, 3:2149, 1996.

[47] A. Ting et al. Plasma wakefield generation and electron acceleration in a self-modulated laser wakefield accelerator experiment. *Physics of Plasmas*, 4:1889, 1997.

[48] Z. M. Sheng, J. Zheng, and D. Umstadter. Plasma density gratings induced by intersecting laser pulses in underdense plasmas. *Appl. Phys. B*, 77:673, 2003.

[49] H. C. Wu et al. Chirped pulse compression in nonuniform plasma bragg gratings. *Appl. Phys. Lett.*, 87:201502, 2005.

[50] Z.-M. Sheng, K. Mima, Y. Sentoku, Nishihara K., and J. Zhang. Generation of high amplitude plasma waves for particle acceleration by cross-modulated laser wake fields. *Physics of Plasmas*, 9:3147, 2002.

[51] L. L. Yu et al. Plasma optical modulators for intense lasers. *Nat. Comm.*, 7:11893, 2016.

[52] S. Weng et al. Extreme case of faraday effect: magnetic splitting of ultrashort laser pulses in plasmas. *Optica*, 4:1086, 2017.

[53] W.-M. Wang, P. Gibbon, Z.-M. Sheng, and Y.-T. Li. Tunable circularly polarized terahertz radiation from magnetized gas plasma. *Phys. Rev. Lett.*, 114:253901, 2015.

[54] A. B. Borisov, A. V. Borovskiy, O. B. Shiyaev, V. V. Korobkin, A. M Prokhorov, J. C. Solem, T. S. Luk, K. Boyer, and C. K. Rhodes. Relativistic and charge-displacement self-channeling of intense ultrashort laser pulses in plasmas. *Physical Review A*, 45:5830, 1992.

[55] J. N. Bardsley and B. M. Penetrante. Relativistic dynamics of electrons in intense laser fields. *Phys. Rev. A*, 40:3823, 1989.

[56] A. I. Akhiezer and R. V. Polovin. Theory of wave motion in an electron plasma. *Soviet Physics, JEPT*, 3:696, 1956.

[57] D. Bauer et al. Relativistic ponderomotive force, uphill acceleration, and transition to chaos. *Phys. Rev. Lett.*, 75:4622, 1995.

[58] E. A. Startsev and C. J. McKinstrie. Multiple scale derivation of the relativistic ponderomotive force. *Phys. Rev. E*, 55:7527, 1997.

[59] W. M. Elsasser. Hydromagnetic dynamo theory. *Reviews of Modern Physics*, 28:135, 1956.

[60] I. Lerche. Kinematic-dynamo theory. *The Astrophysical Journal*, 166:627, 1971.

[61] C. Federrath. Magnetic field amplification in turbulent astrophysical plasmas. *J. Plasma Phys.*, 82:535820601, 2016.

[62] J. A. Stamper et al. Spontaneous magnetic fields in laser-produced plasmas. *Phys. Rev. Lett.*, 26:1012, 1971.

[63] A. R. Bell et al. Observation of plasma confinement in picosecond laser-plasma interactions. *Phys. Rev. E*, 48:2087, 1993.

[64] L. Biermann. Uber den usprung der magnetfelder auf sternen und im interstellaren raum. *Z. Naturforsch*, 5a:65, 1950.

[65] R. Sudan. Mechanism for the generation of 10^9 g magnetic fields in the interaction of ultraintense short laser pulse with an overdense plasma target. *Phys. Rev. Lett.*, 70:3075, 1993.

[66] S. C. Wilks et al. Absorption of ultra-intense laser pulses. *Phys. Rev. Lett.*, 69:1383, 1992.

[67] V. K. Tripathi and C. S. Liu. Self-generated magnetic fields in an amplitude modulated laser filament in a plasma. *Phys. Plasmas*, 1:990, 1994.

[68] R. J. Mason and M. Tabak. Magnetic field generation in high-intensity laser-matter interactions. *Phys. Rev. Lett.*, 80:524, 1998.

[69] Z.-M. Sheng and J. Meyer-ter Vehn. Inverse faraday effect and propagation of circularly polarized intense laser beams in plasmas. *Physical Review E*, 54:1833, 1996.

[70] S. Ali, J. R. Davies, and J. T. Mendonca. Inverse faraday effect with linearly polarised laser pulses. *Phys. Rev. Lett.*, 105:035001, 2010.

[71] G. Pariente and F. Quéré. Spatio-temporal light springs: extended encoding of orbital angular momentum in ultrashort pulses. *Optics Letters*, 40:2037, 2015.

[72] Y. Shi et al. Magnetic field generation in plasma waves driven by copropagating intense twisted lasers. *Phys. Rev. Lett.*, 121:145002, 2018.

[73] J. Vieira, J. T. Mendonça, and F. Quéré. Optical control of the topology of laser-plasma accelerators. *Phys. Rev. Lett.*, 121:054801, 2018.

[74] X. H. Yang et al. Propagation of intense laser pulses in strongly magnetized plasmas. *Applied Physics Letters*, 106:224103, 2015.

[75] J. P. Boris. Relativistic plasma simulation-optimization of a hybrid code. *Proceedings of the 4th Conference on Numerical Simulation of Plasmas (Naval Research Laboratory, Washington D. C.)*, 1:3, 1970.

[76] E. S. Sarachik and G. T. Schappert. Classical theory of the scattering of intense laser radiation by free electrons. *Phys. Rev. D*, 1:2738, 1970.

[77] R. A. Fonseca, Silva L. O., F. S. Tsung, V. K. Decyk, W. Lu, C. Ren, W. B. Mori, S. Deng, S. Lee, T. Katsouleas, and J. C. Adam. Osiris, a threedimensional fully relativistic particle in cell code for modeling plasma based accelerators. *Lect. Notes Comput. Sci.*, 2331:342, 2002.

[78] Osiris — extreme plasma physics. `http://epp.tecnico.ulisboa.pt/osiris/`. [Online; accessed 3-January-2020].

[79] Rémi Lehe, Manuel Kirchen, Igor A. Andriyash, Brendan B. Godfrey, and Jean-Luc Vay. A spectral, quasi-cylindrical and dispersion-free particle-in-cell algorithm. *Computer Physics Communications*, 203:66 – 82, 2016.

[80] Fbpic documentation. `https://fbpic.github.io/index.html`. [Online; accessed 3-January-2020].

[81] B. B. Godfrey. Numerical cherenkov instabilities in electromagnetic particle codes. *Journal of Computational Physics*, 15:504, 1974.

[82] K. Mima et al. Magnetized fast ignition (mfi) and laser plasma interaction in strong magnetic field. *Journal of Physics: Conference Series*, 688:012066, 2013.

[83] F. Debray and P. Frings. State of the art and developments of high field magnets at the 'laboratoire national des champs magntiques intenses. *Comptes Rendus Physique*, 14:2, 2013.

[84] J R Sims, D G Rickel, C A Swenson, J B Schillig, and C N Ammerman. Assembly, commissioning and operation of the nhmfl 100 tesla multi-pulse magnet system. *IEEE Transactions on Applied Superconductivity*, 18:587, 2008.

[85] P. F. Schmit et al. Understanding fuel magnetization and mix using secondary nuclear reactions in magneto-inertial fusion. *Physical Review Letters*, 113:155004, 2014.

[86] U. Wanger et al. Laboratory measurements of 0.7 gg magnetic fields generated during high-intensity laser interactions with dense plasmas. *Physical Review E*, 70:026401, 2004.

[87] A S Sandhu et al. Direct observation of turbulent magnetic fields in hot, dense laser produced plasmas. *Phys. Rev. Lett.*, 89:225002, 2002.

[88] S Mondal et al. Direct observation of turbulent magnetic fields in hot, dense laser produced plasmas. *Proc. Natl Acad. Sci.*, 109:8011, 2012.

[89] A D Shaikh et al. Megagauss magnetic fields in ultra-intense laser generated dense plasmas. *Plasma Phys. Control. Fusion*, 59:014007, 2017.

[90] G. Z. Sun, E. Ott, Y. C. Lee, and P. Guzdar. Self-focusing of short intense pulses in plasmas. *Physics of Fluids*, 30:526, 1987.

[91] P. Sprangle, E. Esarey, A. Ting, and G. Joyce. Laser wakefield acceleration and relativistic optical guiding. *Applied Physics Letters*, 53:2146, 1988.

[92] O. Shorokhov and A. Pukhov. Self-compression of laser pulses in plasma. *Physical Review Letters*, 91:265002, 2003.

[93] I. Watts, M. Zepf, E. L. Clark, M. Tatarakis, K. Krushelnick, and A. E. Dangor. Measurements of relativistic self-phase modulation in plasma. *Physical Review E*, 66:036409, 2002.

[94] M. Malekshahi, D. Dorranian, and H. R. Askari. Self-focusing of the high intensity ultra short laser pulse propagating through relativistic magnetized plasma. *Optics Communications*, 332:227, 2014.

[95] A. Sharma and V. K. Tripathi. Relativistic and ponderomotive self-focusing of a laser pulse in magnetized plasma. *Laser and Particle Beams*, 30:659, 2012.

[96] Y. Liang, H.-B. Sang, F. Wan, C. Lv, and B.-S. Xie. Relativistic laser pulse compression in magnetized plasmas. *Physics of Plasmas*, 22:073105, 2015.

[97] B. Bokaei, A. R. Niknam, and E. Imani. Spatiotemporal evolution of high power laser pulses in relativistic magnetized inhomogeneous plasmas. *Physics of Plasmas*, 22:092310, 2015.

[98] T. S. Gill, R. Kaur, and R. Mahajan. Self-focusing of super-gaussian laser beam in magnetized plasma under relativistic and ponderomotive regime. *Optik*, 126:1683, 2015.

[99] L Gorbunov, P Mora, and T M Antonsen. Magnetic field of a plasma wave driven by a laser pulse. *Physical Review Letters*, 76:2495, 1996.

[100] Z M Sheng and J Meyer-ter Vehn. Analytic and numerical study of magnetic fields in the plasma wake of an intense laser pulse. *Physics of Plasmas*, 5:3764, 1998.

[101] V I Berezhiani, S M Mahajan, and N L Shatashvili. Theory of magnetic field generation by relativistically strong laser radiation. *Physical Review E*, 55:995, 1997.

[102] I Kostyukov, G Shvets, N J Fisch, and J M Rax. Inverse faraday effect in a relativistic laser channel. *Laser and Particle Beams*, 19:133, 2001.

[103] J A Stamper and B H Ripin. Faraday-rotation measurements of megagauss magnetic fields in laser-produced plasmas. *Physical Review Letters*, 34:138, 1975.

[104] S. X. Luan, W. Yu, F. Y. Li, D. Wu, Z. M. Sheng, M. Y. Yu, and J. Zhang. Laser propagation in dense magnetized plasma. *Phys. Rev. E*, 94:053207, 2016.

[105] P. Sprangle, A. Ting, and C. M. Tang. Analysis of radiation focusing and steering in the free-electron laser by use of a source-dependent expansion technique. *Physical Review A*, 36:2773, 1987.

[106] D. Anderson and M. Bonnedal. Variational approach to nonlinear self-focusing of gaussian laser beams. *Physics of Fluids*, 22:105, 1979.

[107] P Mora and T M Antonsen. Electron cavitation and acceleration in the wake of an ultraintense, self-focused laser pusle. *Pyhsical Review E*, 53:R2068, 1996.

[108] V. Erckmann and U. Gasparino. Electron cyclotron resonance heating and current drive in toroidal fusion plasmas. *Plasma Physics and Controlled Fusion*, 36:1869, 1994.

[109] Y. Silberberg. Collapse of optical pulses. *Opt. Lett.*, 15:1282, 1990.

[110] G. Cerullo, A. Dienes, and V. Magni. Spacectime coupling and collapse threshold for femtosecond pulses in dispersive nonlinear media. *Opt. Lett.*, 21:65, 1996.

[111] A. L. Gaeta. Catastrophic collapse of ultrashort pulses. *Phys. Rev. Lett.*, 84:3582, 2000.

[112] O. Shorokhov et al. Self-compression of laser pulses in plasma. *Phys. Rev. Lett.*, 91:265002, 2003.

[113] F. Sylla, A. Flacco, S. Kahaly, M. Veltcheva, A. Lifshitz, Makla V., E. D'Humières, I. Andriyash, and V. Tikhonchuk. Short intense laser pulse collapse in near-critical plasma. *Phys. Rev. Lett.*, 110:085001, 2013.

[114] H. Leblond, D. Kremer, and D. Mihalace. Collapse of ultrashort spatiotemporal pulses described by the cubic generalized kadomtsev-petviashvili equation. *Physical Review A*, 81:033824, 2010.

[115] V. Shumakova, P. Malevich, S. Ališauskas, A. Voronin, A. M. Zheltikov, D. Faccio, D. Kartashov, A. Baltuška, and A. Pugžlys. Multi-millijoule few-cycle mid-infrared pulses through nonlinear self-compression in bulk. *Nature Communications*, 7:12877, 2016.

[116] A. A. Balakin, A. G. Litvak, V. A. Mironov, and S. A. Skobelev. Self-compression of soliton-like laser pulses in the process of self-focusing. *Journal of Optics*, 19:095503, 2017.

[117] G. Fibich. *The Nonlinear Schrodinger Equation –Singular Solutions and Optical Collapse.* Springer, 2015.

[118] D. Anderson and M. Lisak. Nonlinear asymmetric self-phase modulation and self-steepening of pulses in long optical waveguides. *Phys. Rev. A*, 27:1393, 1983.

[119] Z.-M. Sheng, Ma J.-X., Z.-Z. Xu, and W. Yu. Effect of an electron plasma wave on the propagation of an ultrashort laser pulse. *J. Opt. Soc. Am. B*, 10:122, 1993.

[120] D. Anderson. Variational approach to nonlinear pulse propagation in optical fibers. *Physical Review A*, 27:3135, 1983.

[121] E. Esarey, P. Sprangle, J. Krall, and A. Ting. Self-focusing and guiding of short laser pulses in ionizing gases and plasmas. *IEEE Journal of Quantum Electronics*, 33:1879, 1997.

[122] G. Mourou and V. Yanovsky. Relativistic optics: A gateway to attosecond physics. *Opt. and Photonic News*, 15:40, 2004.

[123] N. M. Naumova, J. A. Nees, I. V. Sokolov, B. Hou, and Mourou G. A. Relativistic generation of isolated attosecond pulses in a λ^3 focal volume. *Phys. Rev. Lett.*, 92:063902, 2004.

[124] G. D. Tsakiris et al. Route to intense single attosecond pulses. *New J. Phys.*, 8:19, 2006.

[125] G. Mourou and Tajima T. More intense, shorter pulses. *Science*, 331:41, 2011.

[126] A. A. Balakin, A. G. Litvak, V. A. Mironov, and S. A. Skobelev. Self-compression of relativistically strong femtosecond laser pulses during the excitation of a plasma wake wave. *EPL*, 100:34002, 2012.

[127] A. Pipahl et al. High-intensity few-cycle laser-pulse generation by the plasma-wakefield self-compression effect. *Phys. Rev. E*, 87:033104, 2013.

[128] M. Desaix, D. Anderson, and M. Lisak. Variational approach to collapse of optical pulses. *J. Opt. Soc. Am. B*, 8:2082, 1991.

[129] K. D. Moll and A. L. Gaeta. Self-similar optical wave collapse: Observation of the townes profile. *Phys. Rev. Lett.*, 90:203902, 2003.

[130] B. Zhu, Y.-C. Wu, K.-G. Dong, W. Hong, J. Teng, W.-M. Zhou, L.-F. Cao, and Y.-Q. Gu. Observation of a strong correlation between electromagnetic soliton formation and relativistic self-focusing for ultra-short laser pulses propagating through an under-dense plasma. *Physics of Plasmas*, 19:102304, 2012.

[131] K. Mima, M. S. Jovanović, Y. Sentoku, Z.-M. Sheng, M. M. Škorić, and T. Sato. Stimulated photon cascade and condensate in a relativistic laser-plasma interaction. *Physics of Plasmas*, 8:2349, 2001.

[132] N. M. Naumova et al. Formation of electromagnetic postsolitons in plasmas. *Phys. Rev. Lett.*, 87:185004, 2001.

[133] S. Luan et al. Trapping of electromagnetic radiation in self-generated and preformed cavities. *Laser and Particle Beams*, 31:589, 2013.

[134] T. Esirkepov, K. Nishihara, S. V. Bulanov, and F. Pegoraro. Three-dimensional relativistic electromagnetic subcycle solitons. *Phys. Rev. Lett.*, 89:275002–1, 2002.

[135] D. Farina, M. Lontano, and S. Bulanov. Relativistic solitons in magnetized plasmas. *Phys. Rev. E*, 62:4146, 2000.

[136] J. Borhanian, I. Kouraskis, and S. Sobhanian. Electromagnetic envelope solitons in magnetized plasma. *Phys. Lett. A*, 373:3667, 2009.

[137] W. Feng, J. Q. Li, and Y. Koshimoto. Relativistic soliton formation in laser magnetized plasma interactions. *J. Phys.: Conf. Ser.*, 717:012031, 2016.

[138] V. T. Tikhonchuk, M. Bailly-Grandvaux, J. J. Santos, and A. Poyé. Quasistationary magnetic field generation with a laser-driven capacitor-coil assembly. *Physical Review E*, 96:023202, 2017.

[139] M. N. Polyanskiy, M. Babzien, and I. V. Pogorelsky. Chirped-pulse amplification in a CO_2 laser. *Optica*, 8:675, 2015.

[140] S. Tochitsky, F. Fuiza, and C. Joshi. Prospects and directions of CO_2 laser-driven accelerators. *AIP Conference Proceedings*, 1777:020005, 2016.

[141] Z. Nie et al. Relativistic single-cycle tunable infrared pulses generated from a tailored plasma density structure. *Nature Photonics*, 12:489, 2018.

[142] D. Wu and J. W. Wang. Magetostatic amplifier with tunable maximum by twisted-light plasma interactions. *Plasma Physics and Controlled Fusion*, 59:095010, 2017.

[143] J. Meinecke et al. Developed turbulence and nonlinear amplification of magnetic fields in laboratory and astrophysical plasmas. *Proceedings of the National Academy of Sciences*, 112:8211, 2015.

[144] P. P. Tiwary et al. Turbulent amplification of magnetic field in laser plasma interaction and astrophysical plasmas. *Physics of Plasmas*, 24:062312, 2017.

[145] P. Tzeferacos et al. Laboratory evidence of dynamo amplification of magnetic fields in a turbulent plasma. *Nature Communications*, 9:591, 2018.

[146] J. Schober et al. Magnetic field amplification by small-scale dynamo action: Dependence on turbulence models and reynolds and prandtl numbers. *Phys. Rev. E*, 85:026303, 2012.

[147] Z. Wang et al. Laminar plasma dynamos. *Physics of Plasmas*, 9:1491, 2002.

[148] C. M. Cully and E. F. Donovan. A derivation of the gradient (∇B) drift based on energy conservation. *American Journal of Physics*, 67:909, 1999.

[149] P. Gibbon. *Short Pulse Laser Interactions with Matter: An Introduction.* Imperial College Press, London, 2005.